UNIVERSITY OF CALIFORNIA

SANTA CRUZ

Bioelectronics for Modulating Cell Membrane Potential

A dissertation submitted in partial satisfaction

of the requirements for the degree of

DOCTOR OF PHILOSOPHY

in

ELECTRICAL AND COMPUTER ENGINEERING

by

Harika Dechiraju

December 2023

The Dissertation of Harika Dechiraju is approved:

Professor Marco Rolandi, chair

Professor Mircea Teodorescu

Professor Ali Yanik

Peter Biehl
Vice Provost and Dean of Graduate Studies

LIST OF FIGURES

ABSTRACT

Harika Dechiraju

Bioelectronics for Modulating Cell Membrane Potential

Merging electronics with biological systems poses a significant challenge due to the fundamental difference between biological signaling, which relies on ions and molecules, and electronic signaling, which relies on electrons. Bioelectronics seeks to bridge this gap, creating innovative platforms that seamlessly harness both ionic and electronic functionalities. Among the various bioelectronic devices, ion pumps play a crucial role, utilizing electric fields to transport ions and molecules from reservoirs to specific targets, such as cells. In this work, I will discuss fabricating and characterizing a range of bioelectronic ion pumps. Additionally, I will explore their applications in modulating cell membrane potential, with potential implications for stem cell differentiation, tissue regeneration, and the study of ionic communication in bacteria.

ACKNOWLEDGEMENTS

I would like to express my deepest gratitude to all the people who have supported me in this endeavor.

First, I would like to thank my advisor Marco Rolandi for everything he has taught me over the years, for constantly motivating me to do better, and for helping me communicate my ideas and research to a wide audience.

I would also like to thank members of my committee, Mircea Teodorescu and Ali Yanik for their time and input over the years.

Over the course of my PhD, I have learned the most from several members of the Rolandi group. Thank you, Jack, for the tough love, for always believing that I could do this, and having my back. Thank you, Manping, for being a great friend and super fun to work with.

Thank you, Sergio, for being my sounding board countless times, and for being a friend I could always count on.

I would also like to thank all the other members of the Rolandi group for always helping me and being there for me: Dante, Houpu Li, Narges Asefifeyzabadi, Cristian Hernandez, Tiffany Nguyen, Elham Aslankoohi and Niloofar Asefi. Special thanks to

all the undergrads Carrie Bradley, Elana Muzzy, Jonathan Orozco, Sydnie Figuerres, Alexie Barbee, and Ansel Trevino. It was a blast working with all of you.

Thanks to the wonderful people I've had the opportunity to collaborate with over the years – Giovanny Marquez, Mohammad Jafari, Cody Rasmussen-Ivey, and Colin Comerci. None of this work would have been possible without your support and I have truly learned a lot from each of you.

Thanks to all my close friends Nevedita Sankararaman, Shriya Narayanan, Nazib Sorathiya, Shreya Rajkumar, Lakshminarasimhan, Akshay Likhitkar, and Rashmi Chennagiri for encouraging me and keeping me sane over the course of my PhD.

Finally, I would like to thank my parents D N Rao and Padma, and my brother Harish for their unwavering encouragement, love, and understanding over the years. None of this would have been possible without their support through the highs and lows of this journey.

Publications - In This Dissertation

H. Dechiraju, C. Comerci, L. Luo, N. Asefi, M. Tebyani, P. Baniya, S. Figuerres, A. Trevino, A. Barbee, M. Teodorescu, G. Suel, M. Rolandi "Effect of spatiotemporal K+ modulation on bacterial biofilms" *In Progress*

H. Dechiraju, J. Selberg, M. Rolandi et.al. "On-chip on-demand delivery of K+ for in vitro bioelectronics" *AIP Advances*, 12, 125205 (2022)

H. Dechiraju, M. Jia, L. Luo, M. Rolandi. "Ion-conducting hydrogels and their applications" *Advanced Sustainable Systems,* 6 (2), 2100173 (2022)

G. Marquez*, **H. Dechiraju***, M. Teodorescu, M. Rolandi, M. Gomez et.al "Delivering biochemicals with precision using bioelectronic devices enhanced with feedback control" *bioRxiv*, 555386 (2023) (In review – Plos One)

M. Jia, **H. Dechiraju**, P. Pansodtee, J. Mathews, C. Wu, M. Levin, M. Teodorescu, M. Rolandi. "Bioelectronic control of chloride ions and concentration with Ag/AgCl contacts" *APL Materials* 8.9 (2020): 091106 (2020)

J. Selberg, M. Jafari, J. Mathews, **H. Dechiraju**, M. Rolandi et. al. "Machine-learning driven bioelectronics for closed-loop control of cells" *Advanced Intelligent Systems* 2000140 (2020)

Publications - Not Featured in This Dissertation

M. Tebyani, G. Keller, W.S. Hee, P. Baniya, **H. Dechiraju**, M. Rolandi, M. Teodorescu, et. al "A modular fluorescent camera unit for medical imaging applications" *In Progress*

Y. Park, S. Hernandez, CO Hernandez, **H. Dechiraju**, M. Rolandi, et. al. "Modulation of neuronal activity in cortical organoids with bioelectronic delivery of ions and neurotransmitters" *bioRxiv,* 10.544416 (2023) (in review- Cell Reports Methods)

M. Jafari, **H. Dechiraju**, G. Marquez, M. Rolandi, M. Gomez "Merging machine learning and bioelectronics for closed-loop control of biological systems and homeostasis" *Cell Reports Physical Science* 4, 101535 (2023)

P. Pansodtee, J. Selberg, **H.Dechiraju**, M. Teodorescu, M. Rolandi, et.al "The multi-channel potentiostat: Development and evaluation of a scalable mini-potentiostat array for investigating electrochemical reaction mechanisms" *Plos One,* 16(9), e0257167 (2021)

M. Jafari, G. Marquez, J. Selberg, M. Jia, **H.Dechiraju**, M. Rolandi et. al. "Feedback control of bioelectronic devices using machine learning" *IEEE Control Systems Letters,* 5(4), 1133-1138 (2020)

C. Wu, J. Selberg, B. Nguyen, **H. Dechiraju**, M. Rolandi, et. al. "A microfluidic ion sensor array" *Small*, 16(6), 1906436 (2020)

1. INTRODUCTION

1.1 BIOELECTRONICS

Luigi Galvani's studies on animal electricity from the 18th century can be considered to be the origin of bioelectronics.[1, 2] Bioelectronics bridges the gap between biology and electronics in sensing and actuation.[3-6] They comprise sensors and actuators to interrogate and control physiological processes across lengths and timescales.[7-13] Examples of bioelectronic devices include the pacemaker, brain implants to manage conditions such as epilepsy and Parkinson's, cochlear implants to restore auditory functions, and devices to stimulate the Vagus nerve. Advances in functional materials enable the creation of bioelectronic devices[14-18] that interface with organs[19], organisms[20], and sub-cellular components.[21, 22] Multiple sensing and actuation modalities are available, including optoelectronic[23], plasmonic[24], magnetic[25, 26], and electrochemical.[27-30]

One of the main challenges for bioelectronic devices is translating ionic currents prevalent in biology to electronic signals and vice versa. This is because signal transmission in biological systems relies on the movement of ions and biomolecules instead of electrons and holes.[31-33] Iontronics is a class of bioelectronic devices that rely on ions as their major charge carrier. [34] This consists of many different devices and components such as ionic diodes, ionic transistors (OECTs), ion pumps, etc. [35] Ion pumps can fulfill the dual ionic-electronic capability by translating currents to the flow of a particular species of ions and biomolecules at the device level.[35-37] They

facilitate the movement of ions and molecules with an induced electric field[38] and have various applications such as reducing inflammation[3], treatment of epilepsy[4], influencing cell differentiation[39], and promoting wound healing.[40]

1.1.1 IONTRONICS

Interfacing electronics with biological systems poses a challenge largely because biological signaling is dominated by ions and molecules instead of electrons and holes. Iontronics is a branch of bioelectronics that comprises materials and devices that can fulfill this ionic-electronic capability. [35] In iontronic devices, chemical gradients are created by the controlled release of charged ions at specific locations, at specific times. Examples of iontronic circuits include ionic resistors (ion pumps), ionic diodes, and ionic transistors that behave analogous to traditional electronic circuits but use ions as the primary charge carriers instead of electrons.

Iontronic delivery devices differ from other delivery systems such as microfluidic pumps, or iontophoresis because they provide highly precise delivery without any liquid flow, while also having a constant resupply for the species to be delivered. They can also be controlled very precisely to provide a high spatiotemporal resolution for the delivery. Ion pumps enable on-demand delivery of precise amounts of charged species (e.g., neurotransmitters, and other ions) to well-defined localized environments without requiring any liquid flow. They can achieve ion or drug delivery where delivery can be sustained or turned on and off by demand. When a voltage is applied, ions are transported electrophoretically from a reservoir directly into the target region (cultured cells, tissue, organoids, etc.). The outlets can be made as small as needed, thereby

enabling single-cell stimulation. The electrical current through the device can be translated directly into dosage, which can also be visualized using mathematical models.

1.1.2 MEMBRANE POTENTIAL

Bioelectricity refers to the electrical signaling occurring at the plasma membrane of a cell via ion channels, ion pumps, and gap junctions. These channels and pumps enable in segregation of positive and negative charges across a cell membrane and use energy to transport ions along a concentration gradient. A cell's resting membrane potential, Vmem, is defined as the difference in the concentrations of various ions inside and outside the cell membrane.[41] This resting potential serves as an insight into the behaviors that underlie processes such as differentiation, proliferation, migration, etc. The value is measured in millivolts (mV). A more negative Vmem indicates a strongly polarized, mature, more differentiated cell while a less negative Vmem indicates a depolarized cell, usually embryos or stem cells. [42]

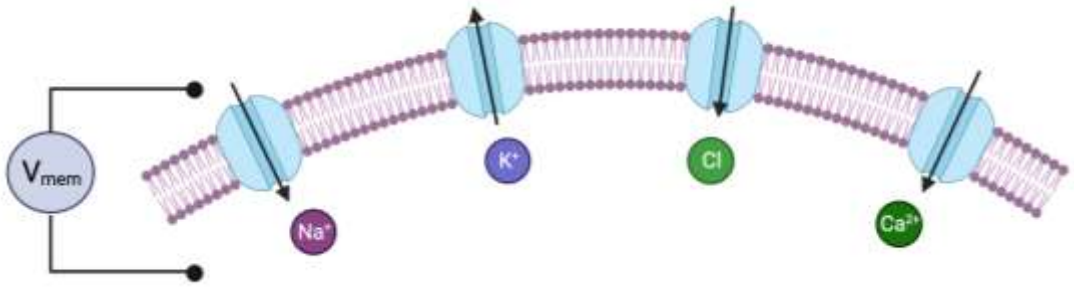

Figure 1 Resting membrane potential in cells. Created with BioRender.com

Bioelectric properties control several key aspects of cell behavior. Vmem regulation plays an important role in the differentiation of several types of stem cells macrophage cells. Vmem control also plays a role in inducing the regeneration of tissue or altering the pattern of regeneration. Modulation of Vmem has also been shown to influence macrophage polarization, an essential phenomenon in the process of wound healing. M1 macrophages show an increased Vmem while M2 macrophages show a decreased Vmem compared to M0 macrophages. [43]

Vmem changes also play an important role in the behavior of prokaryotic cells. Metabolic oscillations in bacterial species such as *Bacillus Subtilis* show a sustained correlation with Vmem oscillations in the bacteria. [44]

1.2 FLOW OF CHARGE

The principle behind iontronic devices is to deliver a specific dose of charged species (ions or biomolecules) at a certain place where the dosage can be controlled by controlling the current in the iontronic circuit. An iontronic circuit consists of various components – (i) electrodes that act as an electrical contact and provide an electronic-ionic interface (ii) electrolytes that consist of solutions of ions, and (iii) ion exchange membranes (IEM) that act as the conductors of charge. Charge transport in the iontronic circuit occurs as a combination of electrons, holes, cations, and anions.

Cations and anions take over the charge transport from electrons or holes at the electronic-ionic interface. This is followed by a mass transport of ions, unselectively

through the electrolytes and selectively through the IEM where either the cations or the anions are the primary charge carriers.

1.2.1 ELECTRODES

To run an ionic current through the IEMs, electrodes that can convert electronic current to ionic current are required. Poly(3,4-ethylenedioxythio-phene) doped with polystyrene sulfonate (PEDOT: PSS) is a common electrode material used in bioelectronic devices. In a 2-electrode setup with PEDOT: PSS acting as the source and target electrodes, upon positively biasing the source electrode, holes are injected into the PEDOT of this electrode. To maintain charge neutrality, cations leave the PEDOT: PSS source electrode as the charge of the PEDOT increases due to the injection of holes. The target electrode is negatively biased, which means that holes are extracted from the PEDOT of this electrode. To remain charge neutral, cations move into the PEDOT: PSS target electrode as the charge of the PEDOT decreases due to the extraction of holes. [45]

Some bioelectronic devices utilize metal electrodes such as palladium and silver as working electrode materials as a means of being selective towards specific ions or biomolecules for delivery. For a positive bias, an electron transfers from the surface of the metal working electrode (WE) to the circuit, resulting in oxidation of the metal surface. This leads to a series of electrochemical reactions. The combination of electron transfer and electrochemical reactions leads to a potential drop at the metal surface. The electron traveling along the electronic circuit to the counter/ reference electrode

(CE/RE) and a cation moving from the source to the target along the IEM complete the circuit. Reduction at the surface of the CE/RE balances the overall charge.[46]

Palladium (Pd) is a widely recognized metal for proton transport. [47] This is because when Pd comes in contact with a solution and is biased at a negative voltage, H^+ is adsorbed onto its surface thereby forming the alloy PdH_x with x ranging from 0.6-0.7. The overall equation for this reaction is:

$$Pd + H^+ + e^- \rightarrow PdH_x$$

When a PdH_x contact is positively biased, H will be released back to the solution from the alloy as H^+.

The best-known reference electrode Ag/AgCl can also be exploited to create working electrodes for bioelectronic delivery of positively charged species. The equation for this reaction is:

$$Ag + Cl^- \longleftrightarrow AgCl + e^-$$

Upon a positive bias, the negative Cl^- is attracted to the Ag surface of the WE. When Cl^- reaches the Ag surface, it oxidizes to Cl. Subsequently, the Cl physisorbs onto the Ag surface to form AgCl. Simultaneously at the RE, the AgCl undergoes reduction to form Ag. The resulting cation in this process is pushed into the IEM to maintain charge neutrality. [48]

1.2.2 ELECTROLYTES

Electrolytes are substances that undergo dissociation when dissolved in water. Upon dissociation, they form ions. The extent to which an electrolyte dissociates determines

its strength with strong electrolytes being those that completely dissociate in water and weak electrolytes being those that partially dissociate. During dissociation, the number of positively charged ions (cations) and negatively charged ions (anions) remain equal, thus maintaining charge neutrality in the electrolyte. These ions act as mobile charge carriers and make the electrolyte electrically conductive. This property of electrolytes is used in iontronic devices. The movement of these ions is a combination of effects such as diffusion, drift, and convection.

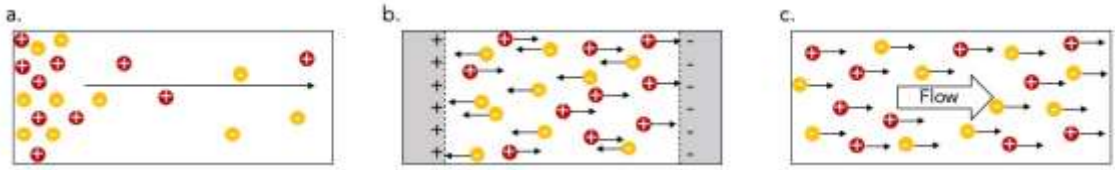

Figure 2 Types of ion transport mechanisms (a.) Diffusion from a region of higher concentration to a region of lower concentration (b.) Drift towards the applied potential. A positive potential attracts anions while a negative potential attracts cations (c.) Movement of ions via convection.

Diffusion is the net movement of particles such as atoms or ions from a region of higher concentration to a region of lower concentration (Fig 2(a)). This diffusion is driven by a chemical potential.

Fick's first law relates diffusive flux (amount of substance diffused per unit area, per time) to the concentration gradient.

$$J = -D\frac{dc}{dx}$$

Where J – Diffusion flux

D – Diffusion co-efficient

dc/dx – concentration gradient

Diffusion co-efficients are experimentally determined and are dependent on the species and environment of the particles. The Stokes-Einstein equation scales diffusion coefficients inversely with the radius of the particle and solution viscosity.

Fick's second law predicts how the concentration changes over time because of diffusion.

$$\frac{dc}{dt} = D\ \frac{d^2c}{dx^2}$$

These laws help us understand the behavior of electrolytes when ions are added or removed using bioelectronic delivery.

Drift is the movement of charged species (ions) in the presence of an electric potential gradient (Fig 2(b)). In this gradient, cations move towards the lower potential (negatively charged electrode) and anions move towards the higher potential (positively charged electrode). For an applied electric field (E), the drift velocity of the ion (v_i) is determined by the following equation:

$$v_i = \mu_i E$$

Where μ_i is the mobility of the ion.

The current density (j) produced by the migration of ions in this electric field is a total of the current densities of the cation and anion. It is related to the drift velocity and charge density as described by the following equation

$$j = zFcv_i = zFc_i\mu_i E$$

Where c is the ion concentration, z is the valence and F is Faraday's constant.

Convection is the motion of particles due to the motion of the solvent (Fig 2(c)). It is a more potent form of ion transport for long range motion and is utilized in several applications such as transport of species in blood, as well as in microfluidic transport systems. Heat, pressure, or density gradients are the driving force behind convective transport. The flux for a particle undergoing convective transport can be given by the following

$$J = c_i v$$

The (extended) Nernst – Planck equation explains transport of ionic species by combining the effects of diffusion, drift and convection.

$$J = -D\left(\nabla c_i - \frac{c_i}{RT} zF\nabla\varphi\right) + c_i v$$

1.2.3 ION CONDUCTING HYDROGELS

Hydrogels are crosslinked 3D polymeric networks capable of retaining water within the polymer chains.[49] The high water content makes hydrogels soft with a low Young's modulus, which results in a conformal interface with soft biological tissue.[50] In the 1960s, polyhydroxyethylmethacrylate (pHEMA) hydrogel was developed as a material for permanent contact with human tissue and it was first used in contact lenses.[51, 52] Thereafter, researchers started using hydrogels in drug delivery,[53] wound dressings,[52, 54], and tissue engineering. [55, 56] Recently, hydrogels have been gradually integrated in bioelectronic devices such as for neuronal recording and simulation.[57] Water-rich hydrogels are ion conductors and make for an ideal bioelectronic interface because in biological systems signals are carried on by ions and molecules.[5, 58-62] This

ionic conductivity has led to the development of iontronics - ion-conducting bioelectronic devices- with an increasing amount of research focused on using hydrogels as ionic conductors at the interface. [57, 60, 63, 64] The unique combination of ionic conductivity, soft, elastic nature, and optical transparency allows ion-conducting hydrogels to be widely used in developing bioelectronics.

i. Structure and Classification of Hydrogels

The physical, chemical and mechanical properties of hydrogels dependent on the inter and intra-molecular interactions between the polymer functional groups and solvents present inside the 3D structure. [65] Based on their crosslinking mechanism, hydrogels can be classified as physical hydrogels and chemical hydrogels. Physical hydrogels are crosslinked by ionic and electrostatic interactions between the monomers, hydrogen bonding, or by dipolar and hydrophobic interactions.[49, 66] Chemical hydrogels have cross links formed by covalent bonds, photo-polymerization (UV induced crosslinking), and enzyme- induced crosslinks. [66] A typical chemical hydrogel structure consists of cross-linked polymer chains, fixed ions and mobile ions (Fig. 3). [49, 67] Depending on the type of charges, hydrogels can be classified into neutral hydrogels and polyelectrolyte hydrogels. Polyelectrolytes have repeating electrolyte units of charged groups, such as polyanion, polycation, and zwitterionic gels.[68-71]

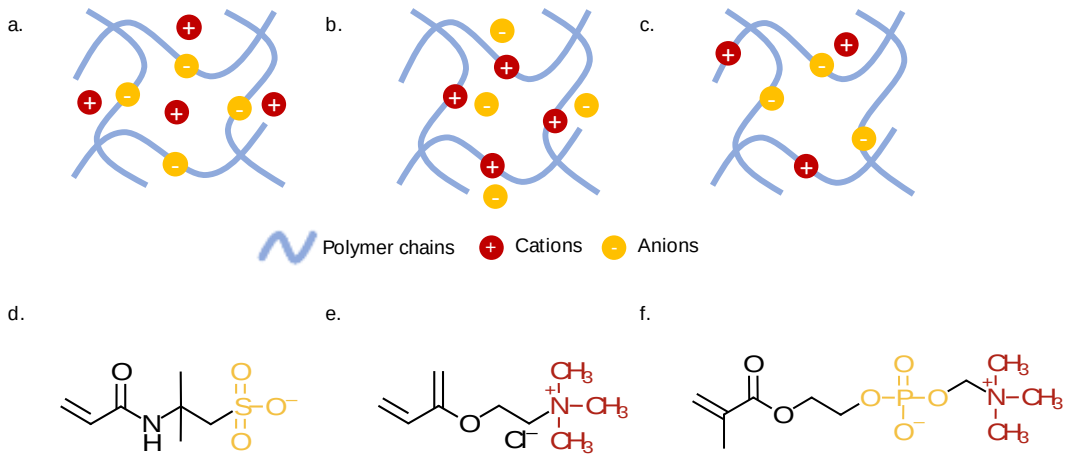

Figure 3 Schematic of the structure of (a) Polyanion hydrogel (b) Polycation hydrogel and (c) Zwitterionic hydrogel. Polyanion hydrogel has a large number of fixed anions (negatively charged ions) and can conduct cations (positively charged ions) through the gel. Polycation hydrogel has a large number of fixed cations and can conduct anions. Zwitterionic gels are composed of monomers both positively and negatively charged. (d) Polyanionic monomer - 2-acrylamido-2-methylpropane sulfonic acid (e) Polycationic monomer - 2-(acryloyloxy) ethyltrimethyl ammonium chloride (f) Zwitterionic monomer - 2-methacryloyloxyethyl phosphorylcholine

Over the past decade, hydrogels made from natural materials have come to the limelight because of their biocompatibility, hydrophilicity, and biodegradable nature.[72] Several natural hydrophilic polymers such as polysaccharides (hyaluronic acid, alginate, chitosan, and cellulose), proteins (collagen, gelatin), and DNA can form a three-dimensional network that can retain a large amount of interstitial water, hence forming a naturally derived hydrogel.[65, 73, 74] They can also mimic the chemical and physical

environments of an extracellular matrix thereby making them popular candidates for creating scaffolds for drug delivery and tissue engineering applications. [73, 74]

ii. Ionic Conduction and Optimization

The history of ionic conductors can be traced back to the 1830s with the work of Michael Faraday on solid electrolytes.[75] The discovery of silver iodide and sodium alumina in 1967 is considered the beginning of the solid-state ionic field.[76, 77] Around the same time, Dupont synthesized a polymer ionomer known as Nafion, which is one of the best proton conductors. [78] Charge carriers in ionic conductors are negatively charged (anions) or positively charged (cations).There can be multiple ionic species with different charges, so the total conductivity of an ionic conductor is given by the sum of the contributions of all of charge carriers:[79]

$$\sigma = \sum_i Z_i e n_i u_i$$

σ is the sum of the ionic conductivity contributed by each mobile ion (i), where Z_i is the absolute value of the ion charge, e is the fundamental charge, n_i is the charge carrier density, and μ_i is the mobility for each ion.

Although the majority of hydrogels are able to conduct ions because of their aqueous environment, here we mainly discuss the hydrogels that have fixed charges in the polymer network, polyelectrolyte hydrogels. From eq (1), the ionic conductivity of a

hydrogel is dependent on both the property of the ionic conductor, such as the charge carrier density, and the property of the charged species, such as their mobility. The assumption is that a hydrogel will be charge neutral so a fixed charge in the polymer backbone will result in the same amount of mobile charge that can contribute to the ionic conductivity. The mobility (μ) of different ions is dependent on the temperature of the system (T), the diffusion coefficient (D), charge of the ion (q), and the Boltzmann constant (K_B) as shown

$$\mu = \frac{\boldsymbol{Dq}}{\boldsymbol{k_B T}}$$

In a porous network, the diffusion coefficient of ions is smaller than the diffusion coefficient for the same ion in water and needs to be adjusted for the size and topography of the pores as shown in [80, 81]

$$D_{eff} = D_0 \frac{\epsilon}{\tau}$$

where D_{eff} is effective diffusion coefficient in a porous network, D_0 is the diffusion coefficient in liquid, ϵ is the porosity, and τ is the tortuosity, which describes the non-linear path from one side of the membrane to the other. [82] Tuning charge carrier density, porosity, and tortuosity during hydrogel synthesis can optimize the ionic conductivity of the hydrogel.

Impedance spectroscopy is a popular choice for determining the mobility and charge density in polyelectrolytes. To do so, impedance spectroscopy analyzes the electrical behavior of an electrolyte sandwiched between two electrodes under applying an alternating electrical signal.[83, 84] When this electrical signal is applied to the sample, periodically the negative and positive ions accumulate at the respective electrodes forming a double layer (Fig. 4a). Using impedance spectroscopy, an equivalent circuit can be generated where C_e represents the capacitance of the electrical double layers, C is the capacitance formed by the electrodes and the electrolyte and R represents the resistance of the bulk electrolyte. This circuit can then be used to calculate the ionic diffusion coefficient which in turn gives the value for charge carrier density as described by Bandara et.al [83].

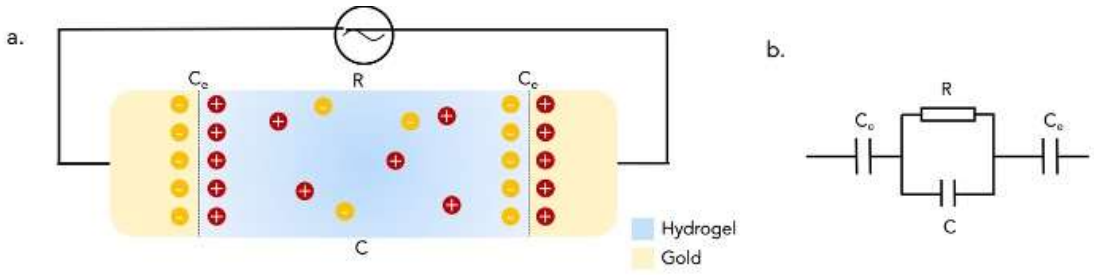

Figure 4 (a) Schematic showing setup for impedance spectroscopy on a hydrogel. The gel is sandwiched in between two electrodes and upon applying an electrical signal, electrical double layers are formed at both the electrodes. (b) Equivalent circuit for the setup described in (a) where C_e represents the capacitance of the electrical double layers, C represents the capacitance formed by the electrodes and R shows the resistance of the bulk electrolyte

Ionic hydrogels are composed of a solid phase crosslinked polymer network with fixed charges and a liquid phase consisting of a solvent that solvates the chains in the network. [85] One of the most common ways of preparing ion-conducting hydrogels is by dissolving ionic salts into the hydrogel solutions.[60] The physical and chemical properties of these hydrogels can be adjusted to suit their application. In this section, we discuss several factors that influence the ionic conductivity of hydrogel as well as common approaches that have been used to improve conductivity.

A. Water Content

Water content depends on the ability of the hydrogel to absorb water, also defined as water uptake or swelling ratio and it plays an important role in affecting ionic conductivity.[67] Higher water content increases the ionic conductivity of polyelectrolytes since the increased number of water molecules not involved in hydration shells enhances the μ and D_{eff} leading to higher conductivity.[86, 87] With an increase in water content, the activation barrier for the ion transport is lowered and ionic dynamics are sped up. [88] According to the findings by Guo et al., the greater the swelling ratio, the higher ionic conductivity. This result is consistent with equation 3. [88]

Crosslinking hydrogels plays a critical role in affecting the porosity and the water content with higher crosslinking resulting in lower porosity and lower water content

leading to lower ionic conductivity. In chemically cross-linked hydrogels, many cross-linking methods can be used to obtain polymerization such as irradiation, chemical reactions coupled with heating and/or pressure, grafting.[89] For instance, irradiation achieves cross-linking by applying high-energy radiations like gamma, x-ray or electron beam radiations to reap covalent bonds.[66] Ubiquitously, the types and degrees of cross-linkers influence the electrical properties of hydrogels. In order to increase the water content of a particular hydrogel, changing the crosslinker to a more hydrophilic one helps. This was reported by Chen-Jung Lee et.al where in order to increase the water content of poly(sulfobetaine methacrylate) (PSBMA) hydrogel and get increased conductivity simultaneously, they changed the cross-linker from N,N'-methylenebisacrylamide (MBAA), to tetraethylene glycol dimethactylate (TEGDMA), which is more hydrophilic.[67] As expected, hydrogels that were more hydrophilic will result in higher water uptake with associated higher porosity, which in turn favors higher ionic conductivity.

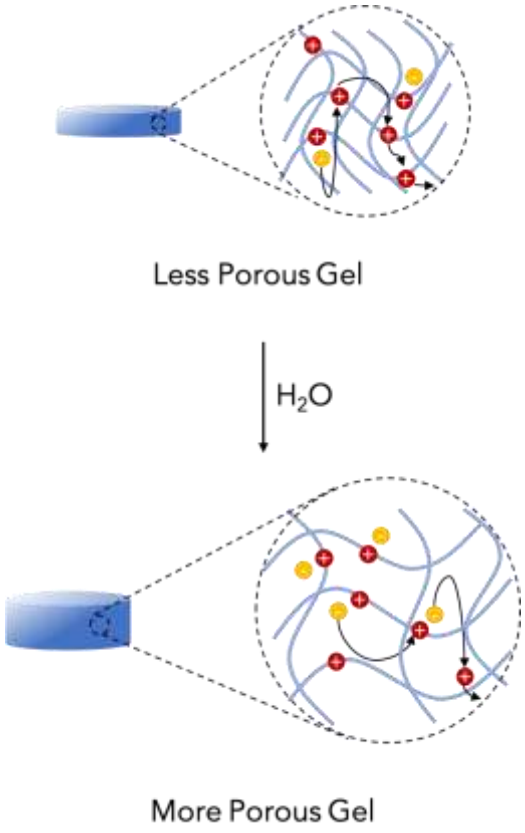

Figure 5 Increasing water content of the gel leads to an increase in porosity. Increased porosity enables faster transport of ions and more ions can move freely within the gel leading to greater ionic conductivity.

B. Charge Carrier Density

Charge carrier density can be defined as the total number of fixed charges per unit volume of the network.[37, 83] According to the simple relation of conductivity and mobility as seen in Equation 1, ionic conductivity is highly dependent on the charge carrier density.[67] Charge carrier density is determined by the number of charged

functional groups in the polymer network. Charge neutrality is an important aspect in a hydrogel. In hydrogels with acidic groups, when in a basic solution, the protons combine with hydroxyl groups to form water and this is compensated by the cations that enter the gel with another hydroxyl group thus maintaining charge neutrality.[85]As discussed earlier, impedance spectroscopy is an important technique in the calculation of charge carrier density. Ruano et al presented a comparative study between four ion conductive hydrogels where they utilized this method to evaluate the ionic properties of the various hydrogels and zero upon the best gel for their application. [90] Another way to measure charge carrier density adopted by Yan et.al is by computing the ion exchange capacity from the polymer's composition and then measuring the water sorption and ion sorption levels as a function of external electrolyte solution concentration. [91] They observed that both water and counter-ion sorption increased with an increase in fixed charge density.

C. Salt Concentration

The performance and sensitivity of bioelectronic devices is directly influenced by the ionic conductivity of the hydrogels used in them. Concentrations of salt solutions affect the ionic conductivity of hydrogels. Lee et. al performed a study to understand the influence of salt concentration on conductivity by measuring conductivities of hydrogels in solutions with different salt concentrations (Fig. 6). [67] As the change in salt concentration increases, there are varying degrees of improvement in the

conductivities of hydrogels. For example, the conductivity of cationic hydrogel poly(2-aminoethyl methacrylate hydrochloride) (cat-PAEMA) is approximately 1.3 S/cm in 2 mM $MgSO_4$ solution and increases to about 1.5 S/cm in 10 mM $MgSO_4$ solution. Eventually, the conductivity increases to ~2.2 S/cm in 100 mM $MgSO_4$ solution.

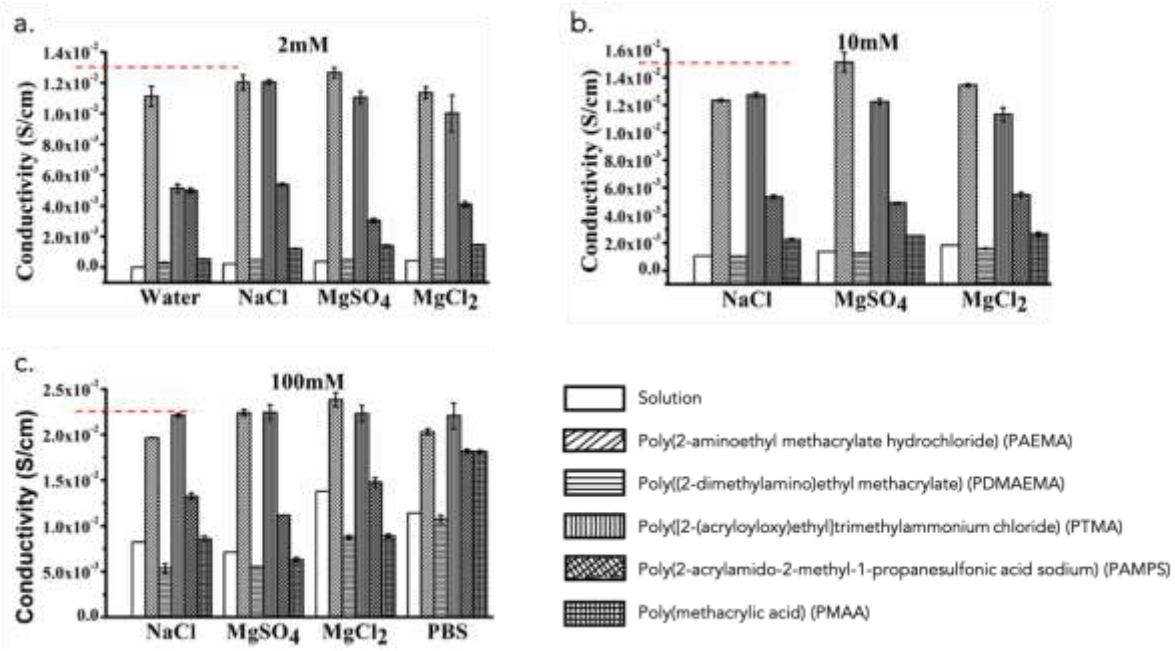

Figure 6: The conductivities of cationic and anionic hydrogels in different salt solutions with varying concentration. (a) conductivities of DI water, cationic and anionic hydrogels in 2 mM salt solutions including NaCl, $MgSO_4$ and $MgCl_2$; (b) conductivities of DI water, cationic and anionic hydrogels in 10 mM salt solutions; (c) conductivities of the same hydrogels in 100 mM salt solutions

For ion exchange membranes, higher salt concentration results in higher ionic conductivity owing to weaker Donnan exclusion. [92] As a result, the increase in concentration of saline solutions generates increased conductive capacity.

Reproduced from [93]

1.3 DEVICE FABRICATION AND CHARACTERIZATION

1.3.1 DEVICE FABRICATION

Bioelectronic ion pump devices are fabricated using microfabrication techniques. Traditionally, this has involved utilizing photolithography methods to sequentially pattern active and passive areas. Photolithography is an optical means of transferring a pattern onto a substrate. Ultraviolet light is used to transfer a pattern from an optical mask to a light-sensitive chemical known as photoresist. Depending upon the type of resist used (positive or negative), the resist either breaks down or hardens where it is exposed to UV light. The patterned film is then exposed to solvents known as developers, to remove softened parts of the resist.

The photoresist is applied onto the substrate by a process known as spin coating. In this process, the top layer of resist is quickly ejected from the wafer's edge while the bottom layer still creeps slowly radially along the wafer. The next step is to transfer a pattern from a photomask to the photoresist. For each device design, several patterned layers are needed, and hence, alignment of the several masks on the wafer is very important. The masks are aligned, and the photoresist is selectively exposed to UV light, usually of a specified wavelength (for example 365 nm) using a tool known as the mask aligner. The dose needs to be adjusted for the photoresist type and thickness and the substrate material, to avoid under- or over-exposures. Post-exposure, the substrates are immersed in a developer solution that dissolves the softened parts of the resist.

Evaporation is used in microfabrication to deposit thin films under vacuum. The vacuum allows vapor particles to travel directly to the target substrate, where they condense back to a solid state and form a thin film. The material to be deposited (source) is heated under vacuum and the evaporated particles are deposited evenly onto the target substrate where they condense and create a thin film. This method is used to deposit the desired metal (Au, Pt, Ti etc) to create electrodes, contacts, and electrical traces on a planar substrate for bioelectronic devices. Acetone and Isopropyl alcohol (IPA) are used to lift off excess metal thereby leaving behind the desired patterns.

Another important step in the fabrication of bioelectronic devices is encapsulation. The encapsulant covers the IEM, acts as a barrier between the reservoir and channel and the target system, and defines openings such as inlets and outlets. The function of the encapsulant is important since it assures that ion currents travel along the intended pathways, i.e. through IEMs and inlets and outlets. Any minor cracks or pinholes in the encapsulant will cause an ionic short circuit and cause failure of the device. The encapsulant should thus be a good insulator. SU-8 and Parylene-C are two commonly used encapsulation materials.

Reactive ion etching (RIE) is a method to use gaseous species to remove material. It can be used to etch away materials such as polymers and photoresists in unwanted regions leaving the materials only in the desired region. The etching rate is dependent on the substrate material and plasma parameters such as applied power, pressure, and gas mixture. The applied electromagnetic field in the plasma chamber directs the

reactive ions toward the substrate. Reactions between the ions and the materials on the substrate give a selective etching process.

Specifics of device fabrication are mentioned in chapters 2,3 and 4 for the respective ion pump geometry used.

1.3.2 DEVICE CHARACTERIZATION

To evaluate the performance of developed devices, several different characterization techniques are used. During device fabrication, most evaluation is performed using visual inspection by optical microscopes and surface profilers. The fabricated devices are later characterized in terms of electrical characteristics and released dose quantification. Additionally, theoretical investigations of device behavior with numerical simulations can be used to complement the electrical and chemical characterization techniques. These techniques are used in different sections within this work, each contributing to better characterizing device performance.

1.3.3 ELECTRICAL CHARACTERIZATION

The iontronic devices described in this work either behave as an ionic pn junction diode or as an ionic resistor. To electrically characterize these devices, either a constant voltage is applied (amperometry) or a constant current is applied (potentiometry), while measuring the other parameter. The ion pumps follow Ohm's law, i.e., they exhibit a linear voltage-current relationship for a given electrolyte and IEM resistivity (Fig 7a).

Integrating the current (I) over the time (t) during which the device was operational gives an estimate of the total charge transferred (Q)

$$Q = \int I(t)dt$$

The total charge transferred helps us understand how many ions were exchanged during device operation. The ratio of the number of moles of species transferred to the ratio of the number of moles of charge transferred is defined as the device efficiency.

The current generated by the device is largely dependent on the counter ions present in the electrolyte. The contribution of the co-ions is negligible. The resistivity of the IEM greatly affects the current produced by the device. Resistivity is dependent on factors such as the length of the IEM, cross-sectional area, water content, and level of hydration of the IEM. The size and mobility of the ions being transported also affect the resistance of the IEM. Smaller ions with high mobility offer lesser resistance. The change in resistance of the IEM can be recorded when the counter-ion is switched to a larger ion or an ion with lesser mobility thus providing insights into the suitability of the given IEM for various ions and biomolecules [94].

Another form of potentiodynamic measurement known as cyclic voltammetry (CV) was also used to characterize the devices (Fig 6b). In CVs, the electrode potential ramps linearly versus time in cyclic phases. The peaks formed for the I-V curves show the oxidation and reduction peaks for the electrochemical reaction occurring. In the context of bioelectronic devices, CVs are helpful in understanding the performance of the electrode material for the ion or biomolecule to be delivered. [95] In cyclic voltammetry, the current passing through the electrode is limited by the diffusion of species to the

electrode surface. This diffusion flux is influenced by the concentration of species at the electrode, and how fast the species can diffuse through the solution. By changing the cell voltage, the concentration of the species at the electrode surface is also changed, as set by the Nernst Equation. Therefore, a faster voltage sweep causes a larger concentration gradient near the electrode, resulting in a higher current. CVs are also useful for calculating electrode capacitance which determines how long can a device be used before it stops being useful for delivery.

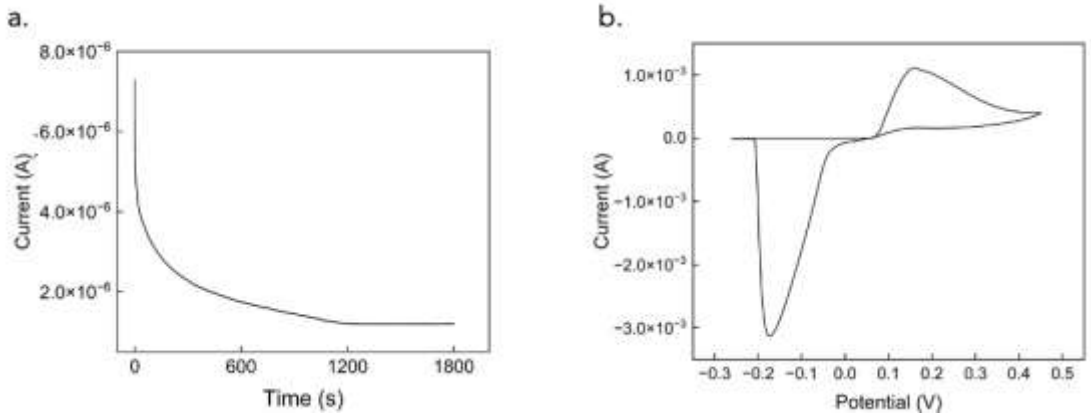

Figure 7: (a) I-t plot generated using chronoamperometry (b) Current–potential plot generated using cyclic voltammetry

1.3.4 FLUORESCENCE CHARACTERIZATION

Fluorescence microscopy was used to verify and quantify the number of ions released at the target due to bioelectronic delivery. Most ions such as H^+, K^+, Na^+, Ca^{+2} can be detected and quantified using fluorescent dyes that are sensitive to that ion. Fluorescent dyes are substances that absorb light waves of a certain wavelength and emit light waves with a wavelength greater than that of the absorbed light. Most of them are compounds containing a benzene ring or a heterocyclic ring with a conjugated double

bond. Under the microscope, it functions by absorbing light at a given wavelength and re-emitting it at a longer wavelength. This fluorescence produces different colors that can be visualized and analyzed.

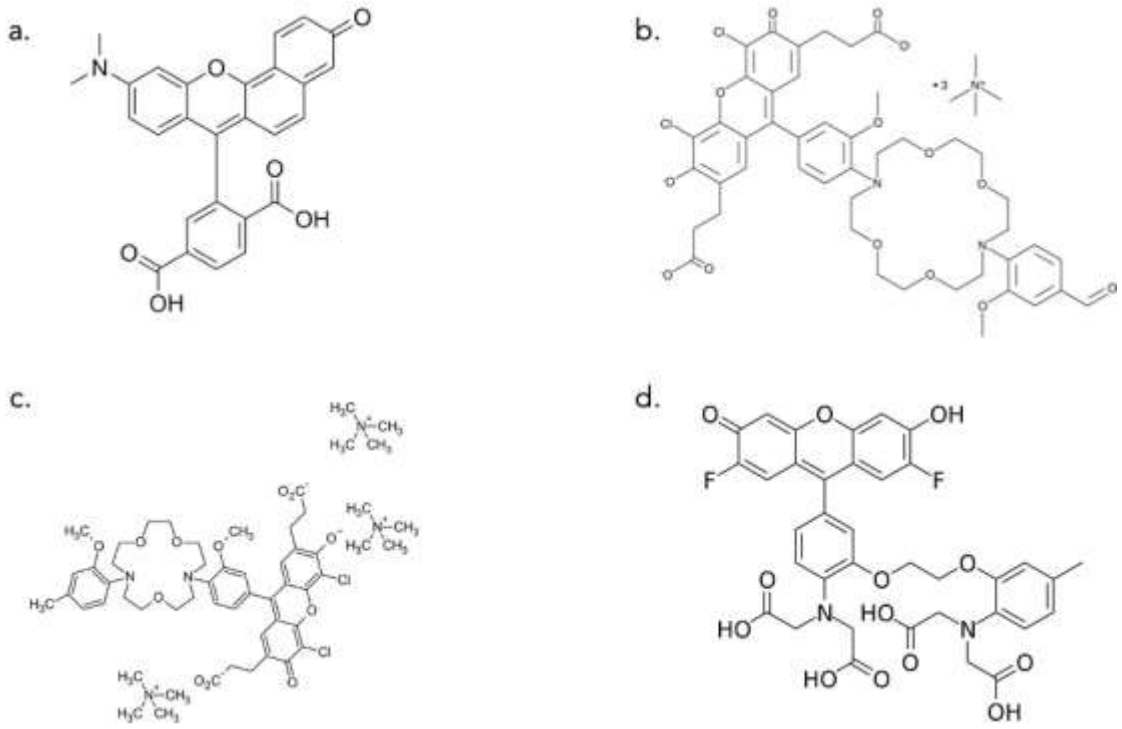

Figure 8: Chemical structure of fluorescent dyes (a) 5-(and-6)-Carboxy SNARF-1, pH-sensitive dye (b) ION Potassium Green -2, [K^+] sensitive dye (c) ION NaTRIUM Green -2, [Na^+] sensitive dye (d) Fluo-4, [Ca^{+2}] sensitive dye

Fluorescence microscopy offers great sensitivity for the detection and quantification of small amounts of substance, as well as allows real-time monitoring of the change dynamics. This is particularly helpful in applications such as bioelectronic delivery where the spatiotemporal resolution of delivery is high and offers ease of integration with machine-learning and feedback control algorithms thus creating closed-loop delivery systems.

The fluorescent dye molecules bind to the ion they are sensitive to, thus causing a change in the fluorescence intensity of the molecule. This change in intensity can be quantified to determine the change in concentration of the ion of interest. While most dyes exhibit a linear relationship between the concentration of the ion and fluorescence intensity, some dyes such as Carboxy SNARF exhibit a ratiometric response where the dye is imaged under two wavelengths and the resulting ratio is used to quantify the pH of the solution. The calibration and usage of these dyes are discussed more in detail in the research contributions section of this work.

For the in vitro cell experiments, fluorescent membrane voltage reporters such as ArcLight, $DiBAC_4(3)$, and Thioflavin T (ThT) were used to detect and quantify changes in membrane voltage (Vmem) of the cells. ArcLight was genetically encoded into the pluripotent stem cells to measure change in Vmem in Chapter 2.[39] Chapter 3 shows the use of $DiBAC_4(3)$ to detect a change in Vmem of macrophage cells [48] while the work in Chapter 4 uses ThT to detect Vmem changes in bacterial biofilms in response to a K^+ stimulus.

RESEARCH CONTRIBUTIONS

2. IONTRONIC ACTUATORS

2.1 PROTON PUMP FOR CELL ACTUATION

Life is built upon closed-loop feedback and regulation systems that maintain a delicate balance of environmental and metabolic conditions that support cellular function[96, 97]. Bioelectronic devices interface electronic devices with biology with potential for sensing and actuation[98] [18, 99-102]. A challenge for bioelectronic devices is translating between ionic and biochemical signals that dominate biology into electronic currents in the devices and vice versa. Iontronics addresses this challenge by modulating ions directly at the device level rather than electron and holes as in traditional semiconductors[35]. Electrophoretic ion pumps mediate the delivery of ions and charged molecules with an induced electric field[38, 103] to treat epilepsy[35], chronic pain[45, 104], inflammation[105], and to actuate movement in plants[106]. Additionally, bioprotonic devices can sense and actuate the flow of H^+ in field effect transistors (H^+-FETs)[107-110], enzymatic logic gates[108], and ion channels[111, 112].

A cell's resting potential, V_{mem}, is an electrical control signal that occurs between the interior of the cell and the extracellular environment regulated by ion channels[113-116]. In non-excitable cells[117], V_{mem} affects cell physiology and functions such as proliferation, differentiation, migration, and apoptosis, as well as cell-cell communication, and large-scale morphogenesis[42, 118]. Recently, optically actuated capacitors have achieved transient V_{mem} control in oocyte cells[102]. The ability to control V_{mem} for long-term is an essential enabling step to the modulation of cell

function, metabolism, and morphogenesis, especially in bioengineering, regenerative medicine, and synthetic morphology applications[119, 120].

Controlling cells with bioelectronics is difficult due to the complexity of cellular response to changing environmental conditions. Cellular processes are hard to model due to noise and uncertainty[121, 122]. This complexity limits most examples of biocontrol to simplified systems such as synthetic gene networks engineered with feedback to achieve noise rejection and adaptation[123-132]. As the complexity of biological systems scale up, the challenge of feedback design increases. Without a model, a standard approach to bioelectronic control would require information a priori of how the biological variable will respond to an electronic stimulus[133, 134]. This information is often not available. In addition, such an approach does not account for potential adaptation in system response or unknown changes in the environment or device response. For example, the commonly used controller in practice, known as the Proportional-Integral-Derivative (PID) controller, might not function properly when the system under control is exposed to the uncertainties, nonlinearities, and unknown disturbances caused by undesired phenomena such as varying environmental conditions[135-137].

Machine learning (ML) has successfully controlled biological systems when offline training and large datasets are available a priori[138-141]. However, deep-learning ML methods such as deep neural networks, deep recurrent neural networks, and generative adversarial networks are slow to update in response to system changes. Real-time ML-based methods, such as adaptive ML algorithms, in combination with tools from

control theory learn and respond to different operational conditions[142-144] and are able to work with nonlinearities, noise, and system uncertainty that are typical of cells or bioelectronic devices. Here, we leverage a single layer neural network with a "sense and respond" [145] composed of radial basis functions (RBF). RBF act as universal approximators[146] and are fast converging, thus ideal for real-time control applications[144, 147].

Here, we demonstrate an array of bioelectronic proton pumps[148, 149] merged with an adaptive machine learning-based controller that can provide control of V_{mem} for an extended amount of time (Fig. 9). In brief, a bioelectronic proton pump array adds or removes H^+ from solution and changes $[H^+]$ in proximity of human induced pluripotent stem cells (hiPSCs) (Fig. 9). In hiPSCs, an increase in extracellular $[H^+]$ results in cell depolarization (lower V_{mem}) and a decrease in extracellular $[H^+]$ results in cell hyperpolarization (higher V_{mem})[150, 151]. We measure relative changes in V_{mem} of the cells using ArcLight, a fluorescent reporter for membrane voltage that we expressed on the cell membrane[152]. To monitor and control the dynamics of V_{mem} in real-time, fluorescent images are taken at regularly spaced time intervals. To set and maintain a specific V_{mem} value for a given cell, we control the system using a machine learning (ML)-based algorithm that maps changes in V_{mem} to prior H^+ stimuli from the proton pump. Using this information, the ML algorithm decides whether the $[H^+]$ surrounding a specific cell should be increased or decreased to achieve the desired V_{mem} value and sends a control voltage (V_{H+}) to the proton pump in the array thus closing the control loop. The algorithm is not trained on any data a priori and makes no use of a model for

either the bioelectronic device or the fluorescently tagged hiPSCs. Based on the target goal and current state, the parameters of the neural network are updated in between the time-lapse fluorescent images such that the "learning" happens in real-time and the target V_{mem} is ultimately achieved.

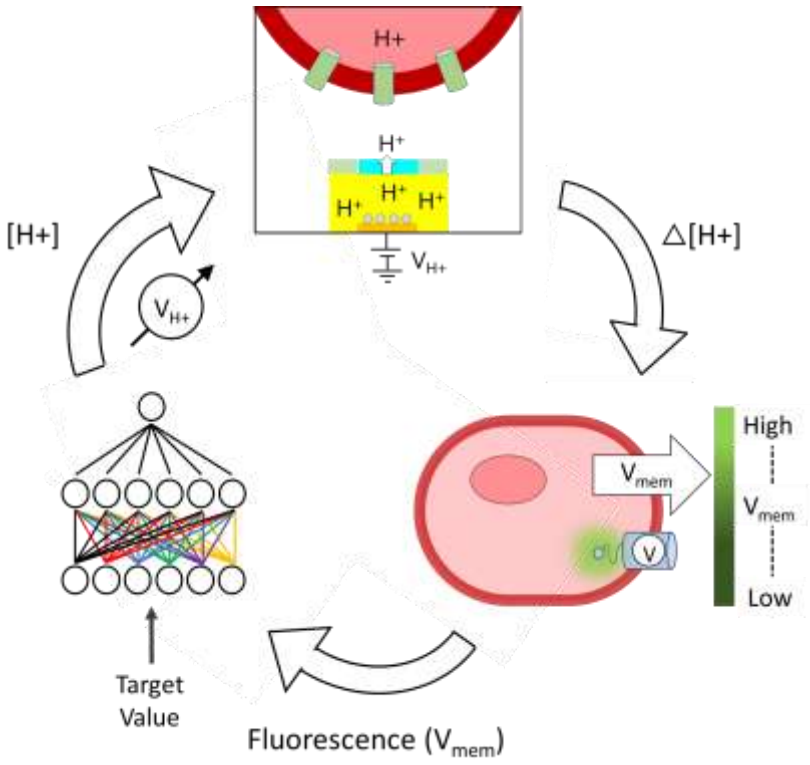

Figure 9: Closed-loop bioelectronic control of V_{mem}. An adaptive learning algorithm controls a proton pump array to change the pH of extracellular fluid and alter V_{mem} to a target value, V_{mem} is measured by a fluorescent indicator for feed back to the control algorithm.

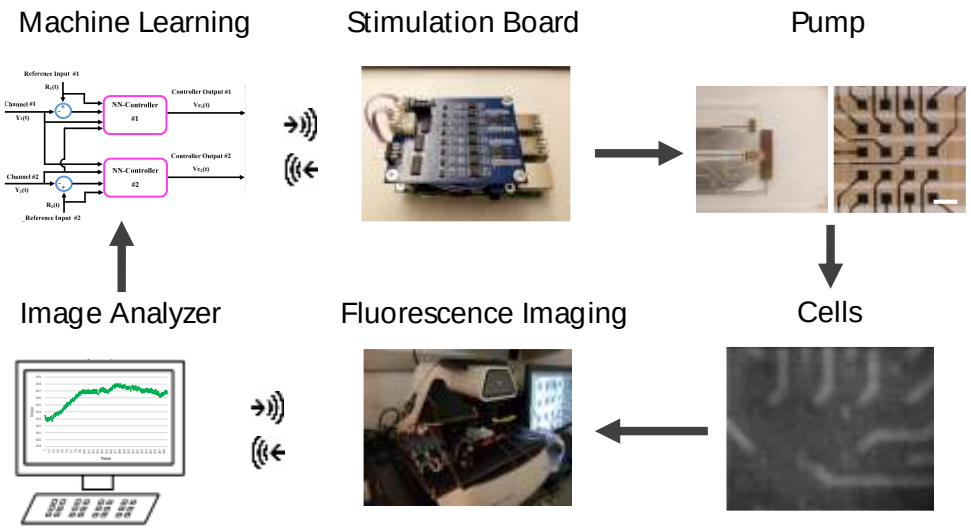

Figure 10: Subsystems of the closed-loop bioelectronic platform. An adaptive ML algorithm communicates a control voltage wirelessly to a stimulation board which controls an array of proton pumps and induces pH gradients around hiPSCs. Fluorescence imaging is used to record the V_{mem} of these cells which changes in response to variation in pH, images are transferred to an image analyzer that samples regions of the image before being feedback to the ML controller.

2.1.1 RESULTS

Each individual pump within the array is made of a Palladium/Palladium Hydride (Pd/PdH) contact that is able to transfer H^+ to and from the solution depending on an applied voltage V_{H+} (Fig. 11A) [108]. Previously described proton pump arrays[148, 149] were fabricated on transparent substrates with integrated microfluidic channels to enable on-chip cell culture and monitoring of device performance and cell responses via fluorescence microscopy. The reservoir and target chambers consist of two

microfluidic channels with 40 μm tall side walls and a ceiling of transparent microfluidic tape. At the closest point, the reservoir and target chambers run parallel to each other with a distance of 1mm, with the ion bridge (brown lines) connecting the two solutions (Fig. 11B). A 2 mm diameter window is excised from the microfluidic tape and aligned to the array of 100 μm x 100 μm proton pump array pixels aligned in a 5x4 grid with a 250 μm pitch in the target chamber prior to sealing the fluidics to allow for interfacing with removable polydimethylsiloxane (PDMS) slides through clamping (Fig. 12). The microfluidic channels allow for distinct electrolyte solution to be flown within the reservoir and target channels. Silver/silver chloride (Ag/AgCl) electrodes located in the reservoir and target channels are paired with the Pd/PdH electrodes located beneath the ion bridge at each pixel in the proton pump array to control ionic flux in and out of the device. A positive value for V_{H+} applied between the array pixel and the Ag/AgCl electrode in the target channel will release H^+ into the target channel thus increasing $[H^+]$ of the solution (Fig. 11C), a negative value for V_{H+} will absorb H^+ from the solution into the contact thus decreasing $[H^+]$ of the solution (Fig. 11D). A voltage V_{RES} between the array pixel and the reservoir can be used to move H^+ from reservoir to Pd contact forming PdH, which increase the efficiency of the proton pump by localizing H^+ to the array pixel although for the work presented here, only V_{H+} is used[148, 149].

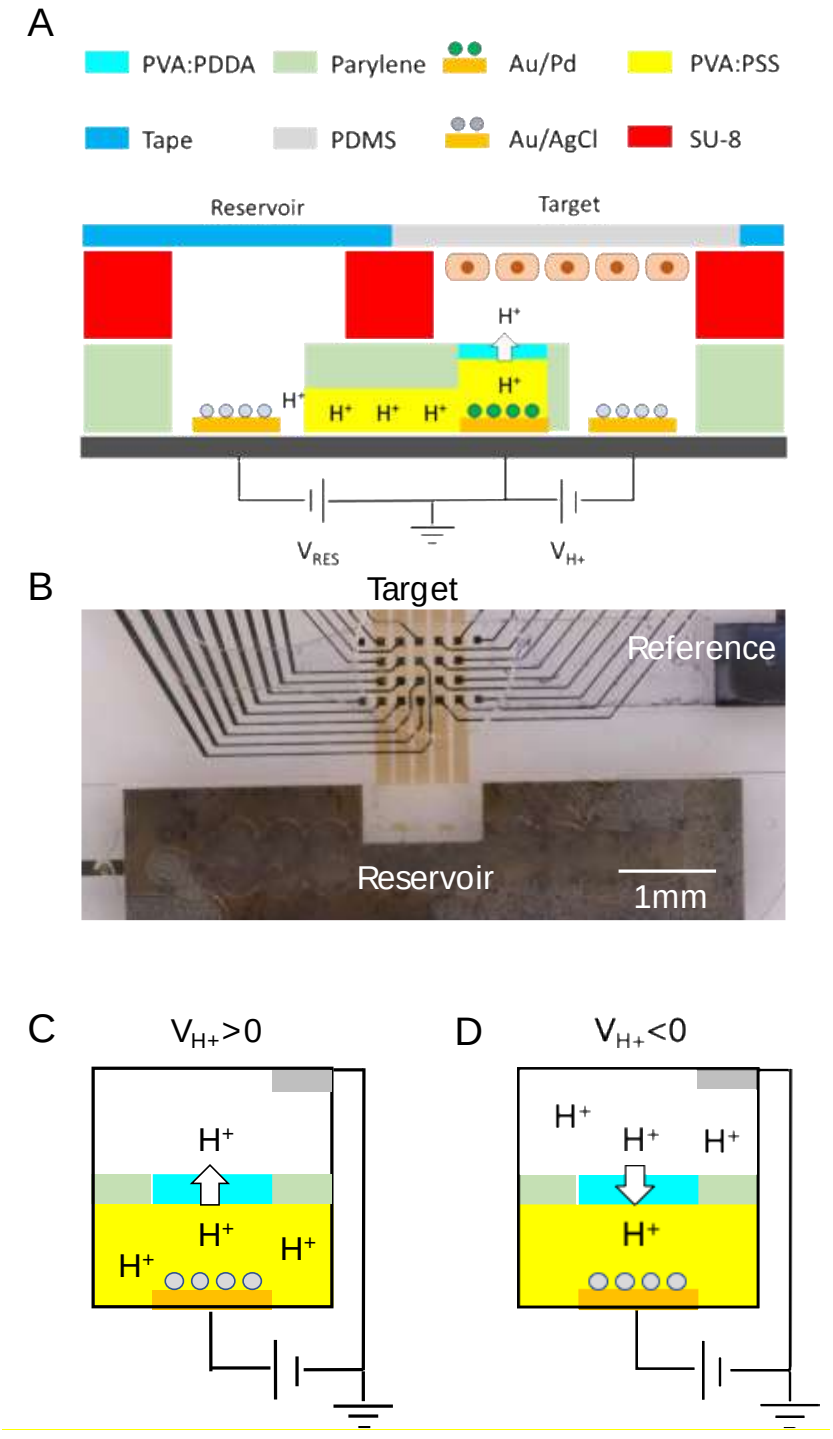

Figure 11: Proton Pump Design. (A) Device schematic (B) Optical image of the proton pump array pixels with the PVA:PSS ion bridge. Scale Bar: 1mm. (C) Proton delivery

to and (D) Proton removal from target solution upon applied bias V_{H+}, Ag/AgCl counter electrode is drawn out of plane for simplicity.

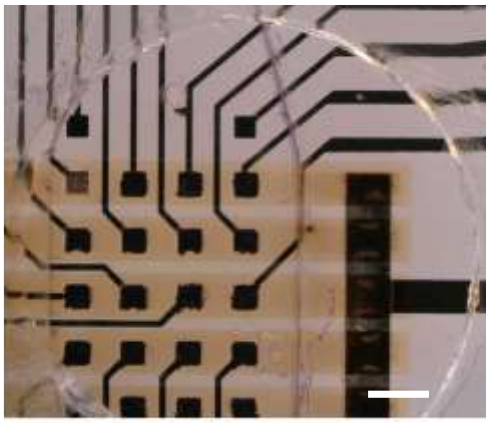

Figure 12: *Optical images of the proton pump array with microfluidic tape sealing the fluidic channel. A 2mm diameter hole is excised from the tape over the array to allow interfacing with stem cells. Scale bar: 250 μm.*

Given that cells and their associated V_{mem} are highly sensitive even to very small changes in $[H^+]$, we first demonstrate that we can precisely set $[H^+]$ in a desired location at a given time so that a specific $[H^+]$ value is regulated in the extracellular fluid (Fig. 13). To do so, we drive the proton pump with a ML-based control algorithm consisting of a radial-basis function-artificial neural network. In this case, $[H^+]$ response from an area of interest that is mapped using a dye whose fluorescence is inversely proportional to $[H^+]$ (SNARF)[153]. The algorithm leverages a neural network comprised of an input layer, a hidden layer, and an output layer (Fig. 13A). The input layer receives the error value between the desired and the measured $[H^+]$ values, information on prior [H+] stimuli, as well as, current and previous $[H^+]$ response to the applied V_{H+}. The desired

output consists of desired values at time k+1, k, and k-1, and the measured output consists of measured values at time k-1, k-2, and k-3.The hidden layer converges to a mapping that allows it to discern which value of V_{H^+} should be applied to the individual proton pump surrounding the area of interest to achieve the desired $[H^+]$.

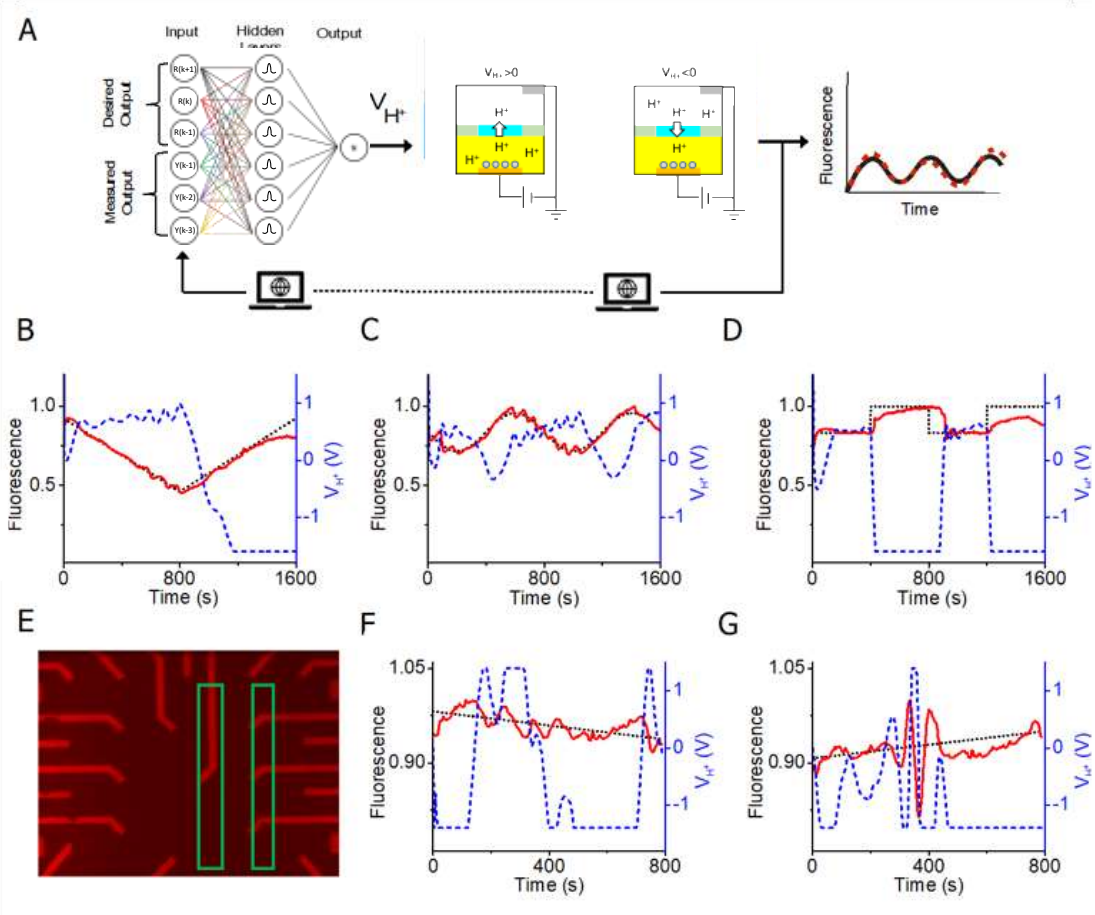

Figure 13: Control of H^+ pump with machine learning controller generates pH gradients in buffered media. (A) A schematic of the experimental setup, the H^+ pump array induces pH gradients in solution upon stimulation by a stimulation board. Fluorescence signals from pH sensitive dye SNARF-1 in media are captured and fed into a neural network machine learning algorithm which attempts to control the

stimulation board voltages to match a prescribed fluorescence pattern. Temporal control of pH monitored through the fluorescence response of SNARF-1 dye over the actuated column of proton pumps (red traces) maps to the target triangle (B), sine (C), and square (D) waveforms (black dotted traces). V_{H+} *(blue dotted traces) for these waveforms responds to the error in the experimental fluorescence value compared to the target value. (E) Fluorescence image of microelectrode array with SNARF-1 dye with labels for multi-column bi-directional control, two separate electrode columns were actuated (yellow) and the fluorescence intensity of SNARF in an area adjacent to the columns (green) was sampled. The fluorescence response (red traces) follows target ramp functions (black dotted traces) both with a negative slope (F) and a positive slope (G),* V_{H+} *is controlled in responds to the error in the experimental fluorescence compared to the target value (blue traces).*

Open-loop tests of the proton pump with SNARF dye in 0.1M Tris buffer show pH gradients forming locally around actuated pixels (Fig. 14).

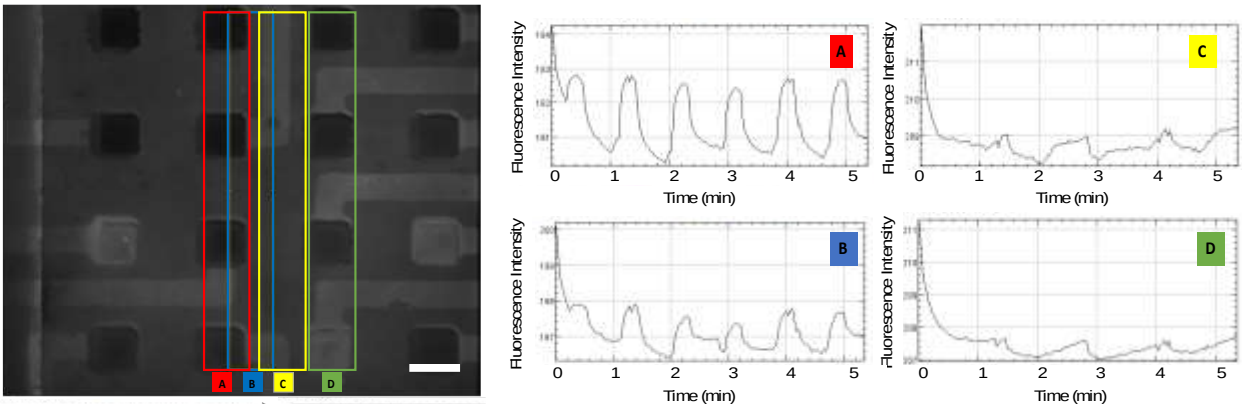

Figure 14: Fluorescence response of SNARF dye during pH cycling. Proton pump pixels outlined in red were stimulated to oscillate the pH in a SNARF solution in 0.1M Tris buffer. Scale bar: 100 μm.

For closed-loop testing with ML-based controller, we start with relatively simple target changes in $[H^+]$ to simulate what may be needed when working with cells over 1600 second trials. In all experiments, we first set a target $[H^+]$ as measured by the fluorescence intensity of SNARF (black dashed line) and we compare it with the actual solution $[H^+]$ as measured by the fluorescence intensity of SNARF (red line) (Fig. 13B). A difference between target $[H^+]$ and actual $[H^+]$ results in an error value, which in turn triggers V_{H+} actuation of the specific pixel (blue line). We show the ability of the proton pump to perform temporal control over the pH in the form of ramp functions with both positive and negative slopes, these ramp functions combined form a triangle wave (Fig. 13B). To test repeated stimulation over time, we demonstrate the ability of the proton pump to perform temporal control over the pH in the form of a sine wave over two periods (Fig. 13C). Additionally, the sine function displays the ability of the ML-based controller to track a function with a gradually changing slope – a challenging feature to achieve with open-loop control. Finally, we use a square wave to step-to and maintain certain pH (Fig. 13D). In addition to temporal control, we achieve spatial control by independently setting $[H^+]$ for two separate areas using two sets of proton pumps (Fig. 13E-G). To this end, we set for $[H^+]$ to increase as function of time in the area on the left of Figure 13E(green boxes) while we set for $[H^+]$ to decrease as a function of time in the selected area on the left of Figure 13E (green boxes). These $[H^+]$

set points correspond to the downward sloping black trace in Figure 13F and the upward sloping black trace in Figure 13G, respectively. With this strategy, we are able to independently increase and decrease [H^+] in two areas that are separated by only 450 um from each other (Fig. 13F, G). Diffusion of H^+ across the boundaries and cross talk of the electric fields generated by the contacts makes this is a remarkably challenging task. This challenge is confirmed by the relatively large swings of V_{H+} for the proton pumps on both sides that are being actuated trying to control [H^+] (Fig. 13G). These large swings cause the actual [H^+] (red trace) to oscillate visibly around the target value (black trace) until it reaches its set point towards the end of the measurement. With little a-priori knowledge, the ML-based controller adapts quickly to unknown and achieves the target value.

Having demonstrated that our proton pump array precisely set [H^+] as a function of time in specific locations, we used this ability to demonstrate proof-of-concept control of V_{mem} in hiPSCs (Fig. 15). The V_{mem} of proliferative cells such as hiPSCs, embryonic cells, and cancer cells has a large effect on their proliferative state[41]. Voltage responsive hiPSCs were generated by using a PiggyBac transposase system to integrate a genetically encoded voltage indicator called ArcLight Q239 with codon optimization for mammalian expression and sequences for membrane trafficking[154]. To integrate the reporter hiPSCs with the proton pump array, we first grow the hiPSCs on a PDMS slab that is then placed on the top of the proton pump array with the cells facing the proton pump contacts. We select a specific area for [H^+] actuation upon visual inspection of cells and their responsiveness to V_{mem} stimulation (yellow box) Figure

14A. We monitor V_{mem} of cells by measuring the fluorescence intensity of the membrane reporter ArcLight within the red box of Figure 15A. In brief, higher fluorescence intensity corresponds to a hyperpolarized V_{mem} which is sensitive to changes in pH between 7.1 and 8.8. To demonstrate short term control, we first attempt to set V_{mem} for the selected hiPSCs along a triangle waveform (black trace) for a period of 1,400 seconds (Fig. 15B). We set imaging of ArcLight and subsequent ML-based control of $[H^+]$ based on measured V_{H+} to occur every ten seconds to avoid photobleaching. As a result, V_{mem} as measured by ArcLight fluorescence (red trace) oscillates around the target function (black).

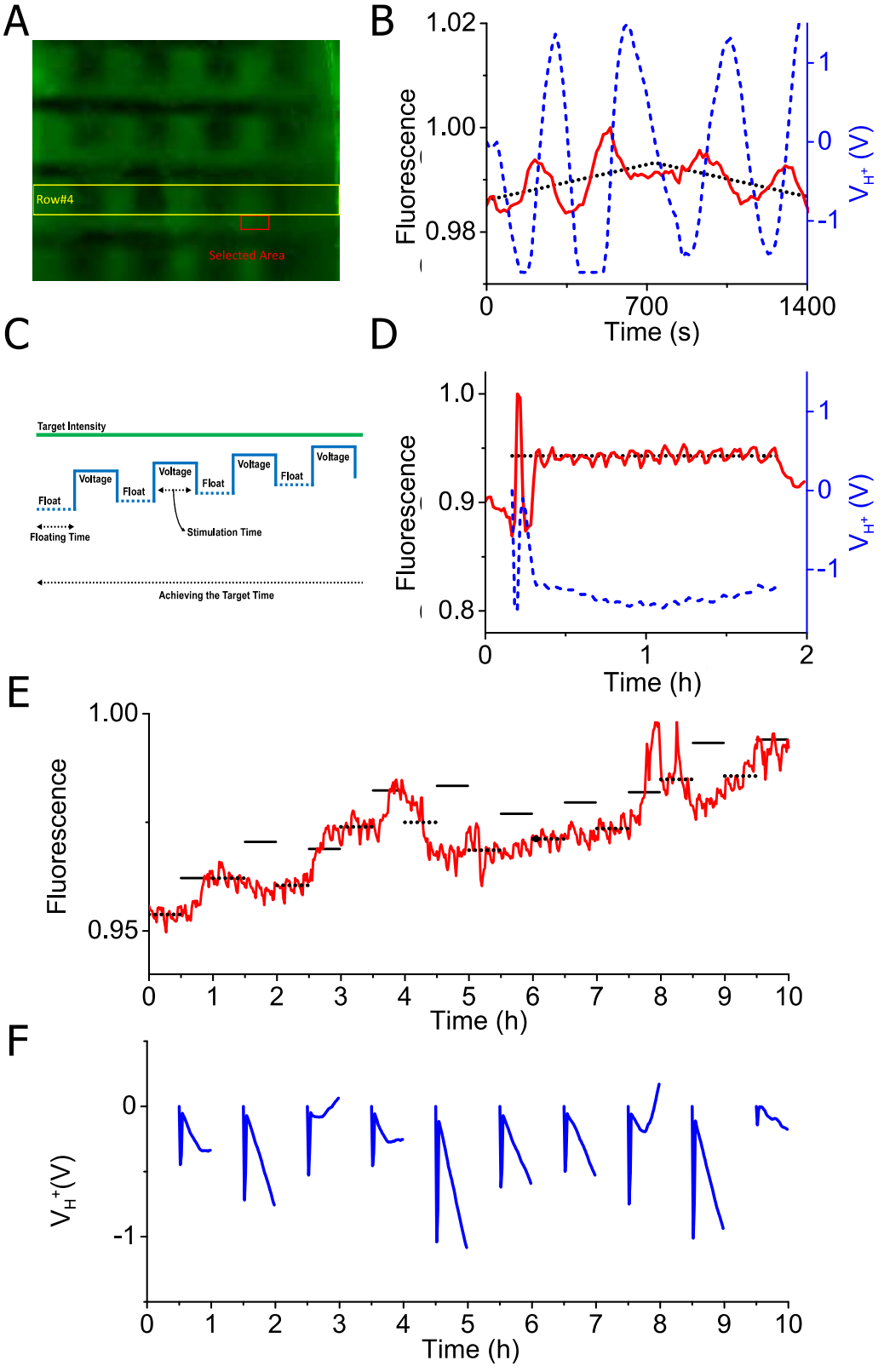
A
Row#4
Selected Area
B
Fluorescence
1.02
1.00
0.98
0
700
1400
Time (s)
1
0
-1
V_{H^+} (V)
C
Target Intensity
Voltage
Float
Floating Time
Stimulation Time
Achieving the Target Time
D
Fluorescence
1.0
0.9
0.8
0
1
2
Time (h)
E
Fluorescence
1.00
0.95
0
1
2
3
4
5
6
7
8
9
10
Time (h)
F
V_{H^+}(V)
0
-1
Time (h)

Figure 15: Proof of Concept - patterned membrane potential changes induced in hiPSCs. (A) Fluorescence of the proton pump array with hiPSCs within the microfluidic channel. A row of proton pumps is actuated (yellow box) and the area where cell fluorescence is sampled (red box). (B) The fluorescence intensity of Arclight-hiPSCs (red trace), indicative of V_{mem}, follows the target triangle waveform (black dashed trace), V_{H+} (blue dashed trace) responds to the error in experimental vs. target values. (C) The pulsed-control algorithm used for prolonged control of hiPSCs. While working towards a target fluorescence intensity (green trace), the controller switches between periods of stimulation where V_{H+} is being driven by the ML controller, and periods of no stimulation where the proton pumps are left floating (blue dotted traces). (D) Medium-term control of V_{mem} monitored through the fluorescence intensity of Arclight-hiPSCs (red trace) to form a step increase and holding at a target fluorescence intensity (black trace). V_{H+} is pulsed according to the pulsed-control algorithm with the stimulation and rest duration being 2.5 minutes each. (E) Long-term control for V_{mem} monitored through the fluorescence intensity of Arclight-hiPSCs (red trace) towards increasing the V_{mem} over the course of 10 hours. The mean fluorescence intensity over the floating period of the pulsed-control algorithm was calculated (black dotted lines) and the target fluorescence intensity during stimulation is set to 2 fluorescence units above that value (black solid lines). (F)V_{H+} is controlled during the stimulation periods of the pulsed-control algorithm to raise the V_{mem} and decreases in voltage over the stimulation period indicating a shift towards alkaline conditions around cells which is expected to raise V_{mem}.

For long term V_{mem} control, we adopt a different sequence for stimulating the hiPSCs in which we alternate periods in which the proton pumps are active with periods during which the proton pumps are left floating (Fig. 15C). We adopted this sequence after observing stimulating the cells for longer than 30 minutes at a time makes the cells less responsive to changes in $[H^+]$. With this sequence, we were able to stepwise increase the V_{mem} of the hiPSCs in the selected locations and maintain this for over one hour (Fig. 15D). We estimate that we were able to increase V_{mem} by about 10 mV respect from the resting V_{mem} by measuring the change in ArcLight fluorescence [155]. These changes are consistent with what we measured with patch clamping on cells exposed to solutions of different pH (Fig. 16). During this time period, the ML-based control algorithm holds V_{H+} negative, which corresponds to a lower $[H^+]$ concentration than neutral in solution and it is consistent with what we have observed using electrophysiology. To confirm that V_{H+} is having an effect on V_{mem}, we notice that when the cells are not being stimulated, V_{mem} slowly drops towards its initial value likely because $[H^+]$ returns to its neutral level due to the diffusion of ions from the surrounding areas (Fig. 15D). This diffusion is slower than the timescale of our sequence so that we are able to keep V_{mem} to a set value with minimal oscillations. We demonstrate proof-of-concept V_{mem} control for a period of 10 hrs by setting the target ArcLight fluorescence 2 fluorescence units higher than the average measured V_{mem} of the 30 min period prior (Fig. 15E, F). We observe that the V_{mem} of the cells becomes

more polarized during the 30 minutes of stimulation and depolarizes during the floating periods (red trace). Over the course of the trial the extent of polarization during the pumping period is greater than the depolarization in the floating period resulting in a gradual trend towards polarization for the hiPSCs. By calibrating the fluorescence change in the Arclight reporter, we estimate that we were able to achieve an increase V_{mem} of the selected hiPSCs by 10 mV in the 10 hr period.

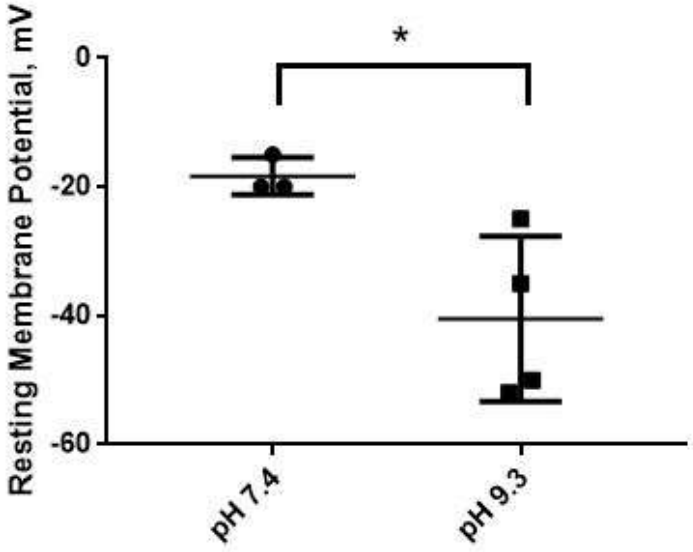

Figure 16: Electrophysiology measurements of hiPSC resting membrane potential. Current clamp at 0 pA was used to find the resting membrane potential of hiPSC ArcLight cells in mTeSR no phenol red at the control pH of 7.4 and the high pH of 9.3.

2.1.2 DISCUSSION

Bioelectronic actuators are an important part of realizing two-way communication with living systems. Inherent challenges in actuating biological tissues such as information

carrier mismatch and system dynamics have limited the field to a point where the number of examples of bioactuators is relatively few compared to that of biosensors. Here, we show that it is possible to combine proton pumps as bioactuators with machine learning-based control approaches into biohybrid system that can address these issues to achieve precise closed-loop control of pH, which in turns allows long term proof-of-concept closed-loop control of membrane voltage in cells. To the best of our knowledge, this is the first proof- of-concept control of V_{mem} on non-electrically excitable cells using closed-loop bioelectronic devices. Our ML approach did not experience failure modes dealing with uncertainties associated with over-stimulation of the biology, device variability, and saturation of the system. To this end, we can manipulate V_{mem} for periods as long as 10 hrs opening the opportunity for long-term control of cell function and proliferation. This ability to induce V_{mem} changes on non-excitatory cell types is of interest for applications in regenerative medicine and synthetic biology. In the future, a combination of additional monovalent and divalent ion species, and small ionic molecules, can increase the capabilities of our system. Importantly, closed-loop biohybrid systems, such as this one, are highly anticipated due to their broad applicability across the fields of biology and engineering. Thus, new technology in synthetic biology and bioelectronics with closed-loop control could result in unprecedented spatiotemporal control over nature.[99, 100]

2.1.3 METHODS

Device Fabrication: Ion pump arrays were fabricated on borosilicate glass wafer substrates which were cleaned via sonication for 10 minutes in acetone and isopropanol

prior to a rinse with water. Au contacts and traces were patterned photolithographically with positive photoresist (S1813, Micro-Chem Corp.) and e-beam evaporation (10nm Ti, 100nm Au) followed by liftoff in acetone. Subsequent patterning with S1813 photoresist defined electrode regions for electrodeposition (see electrodeposition section in materials and methods). After electrodeposition, a 1.4 μm insulating layer of parylene-C was deposited (Specialty Coating Systems Labcoter 2 system) in the presence of A174 adhesion promoter in the deposition chamber. The parylene was etched with an oxygen plasma at 200V with the regions over the electrodes and contact pads exposed, and the interconnecting regions protected by a thick positive photoresist (SPR220-4.5, Micro-Chem Corp.). Prior to deposition of polymer coatings, wafers were treated with the a 5% solution of (3-Glycidyloxypropyl)trimethoxysilane (GOPS) in ethanol via spin coating at 1000 rpm for 30s and then baked at 110C for 5 minutes to promote adhesion of the ion bridge. A mixture of 8%wt polyvinyl alcohol (PVA) and 2% polystyrene sulfonic acid (PSS) in water was then passed through a 0.8 μm MCE syringe filter and spin coated on the wafers at 3000rpm for 30s followed by baking at 120C for 2 hours. The PVA:PSS CEM was etched with an oxygen plasma at 200V with the desired pattern defined with SPR220-4.5 photoresist. A second 1.4 μm coating of parylene was then deposited with the same protocol as above to insulate and protect the ion bridge from the subsequent steps. To promote adhesion between the parylene and SU8 photoresist, GOPS was again deposited using the above process prior to SU8 patterning. SU8 was spun onto the wafer at a speed of 1250 rpm for 30 s and a ramp of 300 rpm, microfluidic channels of height 40 μm were patterned forming the

sidewalls reservoir and target chambers. The parylene insulation layer protecting the ion bridge openings in the reservoir and target channels were defined and etched using the same process as the previous parylene etch. A mixture of 2.5% wt PVA and 5% wt poly(diallyldimethylammonium chloride) (PDDA) in water was passed through a 0.8 μm MCE syringe filter and spin coated on the device at 6000rpm for 30 seconds prior to baking at 120C for 1 hour prior to etch features being patterned in SPR220 photoresist and etching with O_2 reactive ion etching. Devices were then diced from the wafers prior to sealing the microfluidics. Single sided microfluidic transparent diagnostic tape (3M 9964) was used to seal the microchannels on the proton pump array after the devices were diced. Features in the tape layer were punched out with 1 mm and 2 mm diameter biopsy punches for fluidic inlets and openings for cell clamping respectively. The tapes were then aligned to features on the device and pressed to seal by hand.

Electrodeposition: Pd nanoparticles were deposited onto the MEAs using a 1wt.% Palladium Nitrate solution which was made by diluting a 10wt.% PdNO3 solution with DI-water. The nanoparticles were electrochemically deposited by applying a DC voltage of –0.3V for 4 seconds using an AgCl reference electrode and Pt counter electrode. An Autolab Potentiostat was used for the electrodeposition.

Stimulation Board: The stimulation unit is a custom designed modular circuit board for stimulating up to 64 electrodes simultaneously. The design consists of single-board computer, adjustable voltage sources, ammeters, and an analog switch. The adjustable voltage source can be controlled in a range of -4 V to +4V with a resolution of 1.95

mV and able to source current up to 30 mA. Stimulate current can be measured in a range of -1,650 nA to +1,650 nA with a resolution of 0.8 nA using built-in ammeters. Ultra-Low-Leakage CMOS Analog switches allow the stimulation unit to connect/disconnect individual electrodes results in the addition output stage, floating. The stimulation unit can operate in two different modes, standalone and network. The standalone mode is where the output stages(voltage) of the stimulation unit are pre-programmed and run sequentially. On the other hand, in network mode, the stimulation unit will be listening to an incoming UDP packet, and output stages can be programmed in real-time via a wireless connection. The network mode allows the machine learning control algorithm, which runs in a different machine to perform closed-loop control using feedback from both fluorescent images and measured current.

$[H^+]$ measurement**:** We used microscope based real-time imaging over the MEAs to monitor $[H^+]$ change. We used 50 uM SNARF dispensed in 0.1M Tris buffer as a fluorescent $[H^+]$ indicator, which was flowed into the target chamber via a sealed microfluidic channel. Thereafter, the device was monitored by BZ-X710 fluorescence microscope with10x Nikon objective (excitation: 560/40 nm, emission: 630/75 nm), and data were collected every 2s in real-time. Each set of experiments was repeated a minimum of three times, representative recordings are presented. Data were analyzed using ImageJ software.

Machine Learning-based controller algorithm: Machine Learning-based controller performs in real-time and updates its parameters online. The technique could roughly be considered as supervised learning since we know our target response for the cellular

system and actively correct bad behavior by the algorithm. There was no training of the ML-based algorithm prior to the initiation of the experiments. Hyperparameters were tuned on the fly at the beginning of the experiment (if needed) and the radial-basis neural network parameters were randomly initialized. The "training" happened in real-time by learning each time a new data point was generated through the course of the experiment. To provide an appropriate real-time ML-based controller, the total instantaneous error energy function of the system (i.e., $E(k) = \frac{1}{2}e^2(k)$) is considered as a Lyapunov candidate to be utilized for updating the ML-based controller's parameters for guaranteed convergence. Here e(k) is the system error (i.e., $e(k) = R(k) - Y(k)$), R(k) is the target of the system, and Y(k) is the output of the system. The updates to the adaptive ML-based controller's parameters are made by computing the appropriate gradients which are all derived utilizing the above mentioned Lyapunov candidate. The ML-based controller updates its centers' c_i, weights' w_i, and bias term w_0 by using equations (S5, S6, and S7) in supplementary materials, respectively. Algorithm S1 (in supplementary material) is summarizing the overall real-time adaptive machine learning-based control methodology employed in this paper as pseudo-code.

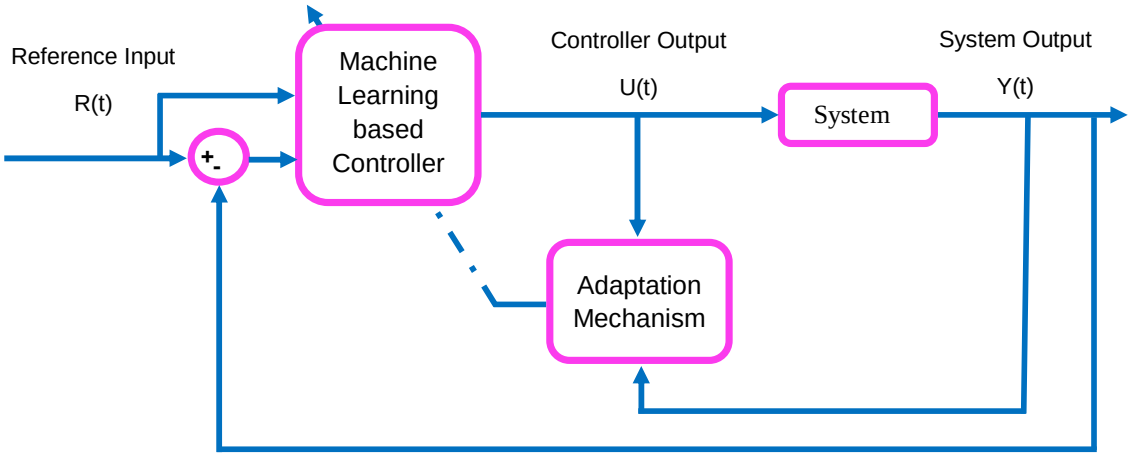

Figure 17: Architecture of online machine learning based direct controller designed for controlling the system.

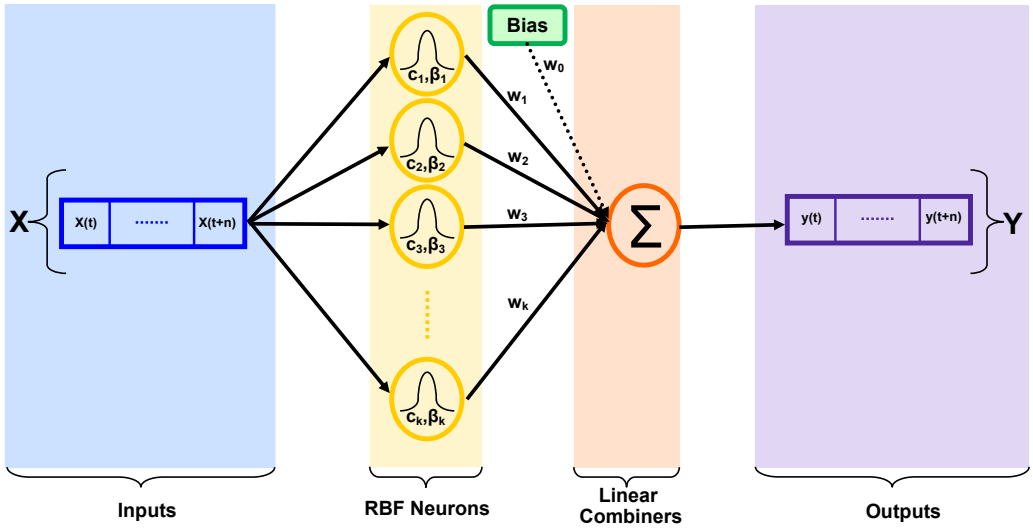

Figure 18: Architecture of Radial Basis Function Neural Network.

Cells: hiPSCs were a generous donation from David Kaplan's group (ND418566, NINDS Human Genetics and DNA Cell Line Repository[156]. Stem cells were maintained at 5% CO_2 in StemFlex Medium (A3349401, ThermoFisher) on hESC Qualified Matrigel Matrix (354277, Corning) coated plates with the dilution recommended by the manufacturer. Cells were disassociated with TrypLE Select (12563029, ThermoFisher). Transgenic cells were made by transfecting 500 ng of plasmid via 1 µL of lipofectamine 3000 (L3000008, ThermoFisher) per well of 24 well plate containing 500 µL of Opti-MEM (31985062, ThermoFisher) with 1X RevitaCell (A2644501, ThermoFisher). Reagent was removed after 4 hrs and replaced with StemFlex. Cells were allowed to recover for 3 days before being selected with 50 µg/mL G418 in StemFlex with 10 µg/mL ROCK inhibitor Y-27632 (72304, STEMCELL Technologies). After selection, a stable, clonally pure line was made by serial dilution using StemFlex with 1X RevitaCell. Clones were expanded in StemFlex and then assayed for alkaline phosphatase activity (SCR004, Millipore). The clone with best membrane localization and expression of ArcLight was chosen for further experimentation and frozen down using NutriFreez D10 (05-713-1E, Biological Industries). Prior to being used in experiments, hiPSC ArcLight cells were plated in mTeSR1 no phenol red (05876, STEMCELL Technologies) and allowed to expand for two passages prior to seeding on PDMS slabs that were coated in hESC Qualified Matrigel Matrix. Slabs were used in bioelectronic chips one to three days after seeding. Cells were perfused with mTeSR1 no phenol red during experiments.

Plasmid Construction: A pENTR1A plasmid with a CAG promoter and multiple cloning site followed by a SV40 poly A was used to clone in the mammalian codon optimized ArcLight Q239 from the plasmid CMV ArcLightCo (Q239)-T2A-nls-mCherry, a gift from Vincent Pieribone (Addgene plasmid # 85806 ; http://n2t.net/addgene:85806 ; RRID:Addgene_85806). Cloning was done by In-Fusion HD Cloning Plus (638909, Takara) with HindIII and SalI restriction enzyme sites added. PCR was done using PrimeSTAR GXL DNA polymerase (R050A, Takara). The resulting pENTR1A CAG ArcLightCo construct was then Gateway LR clonased (11791020, ThermoFisher) into the hyperactive piggyBac transposase-based, helper-independent and self-inactivating delivery system, pmhyGENIE-3 containing a neomycin resistance gene in the backbone for selection, a gift from Stefan Moisyadi[157]. The resulting plasmid HypG3NeoBBArcLightCo (Q239) was used for subsequent transfections.

hiPSC ArcLight pH Response Assay: A PDMS microfluidic chip with multiple inputs was used to sequentially add mTeSR1 no phenol red media set at different pH by adding 5N NaOH or 1N HCl to large colonies of hiPSC ArcLight cells. The pH of the media was tested before and after the experiment to make sure that it had stayed constant during the experiment. Each pH solution was flowed over the cells for 5 minutes followed by the control media and images were taken of the cells every minute using an EVOS FL Auto2 imaging system with a standard GFP filter. Each solution was tested twice to make sure that the genetically encoded reporter was still responsive even after high pH media was applied.

Electrophysiology: hiPSC ArcLight cells were grown in mTeSR1 with no phenol red for two passages. Cells were then seeded on hESC Qualified Matrigel Matrix coated cover slips at a very low density. Cells were patched using mTeSR no phenol red media as the external media with or without 8.31 mM NaOH. The internal solution was 130 mM KCl, 10 mM NaCl, 0.5 mM MgCl2, 10 mM HEPES, 1 mM EGTA, 2 mM Mg-ATP, adjusted to pH 7.2 with NaOH. Resting membrane potential recordings were obtained by current clamp at 0 pA for 10 sweeps for 10 seconds each.

Reproduced from [39]

2.2 CHLORIDE PUMP

Ranging from intercellular communication to organ function, ionic species play an important role in natural systems.[1] A majority of physiological processes, such as muscle contraction, neuronal signaling, and metabolism, involve the exchange of ions between cells.[2] On the other hand, electrons and holes dominate communication between electronic devices. Bioelectronics bridges natural systems and electronic devices by translating ionic signals in the body into electronic signals for sensing and control.[3-7] Iontronic devices, for example, address individual ions and small molecules to control specific physiological pathways. [4, 8, 9] These include the precise delivery of Ca^{2+}, K^{+} and gamma-Aminobutyric acid (GABA) to control epileptiform activities, and treat neuropathic pain with low dosage and less side effect.[10, 11] To this end, our group has demonstrated the control of H^{+} in field-effect transistors [12] and memories[13], enzymatic logic gates and bioluminescence[14], ion channel devices[15-18], H^{+} modulators for delivery of cargo[19, 20] and glucose sensing[20]. These devices are enabled by using

Pd/PdH_x contacts, also known in the reversible H reference electrode, to translate electronic signals into H^+ signals. This translation occurs according to the potential dependent reversible reduction, $H^+ + e^- \leftrightarrow H$, at the Pd/PdH_x - solution interface and the subsequent physisorption of H onto Pd to form PdH_x.[21] An electrical potential applied on the Pd/PdH_x contact shifts the reaction equilibrium and induces the transfer of H^+ to and from the solution, which effectively controls $[H^+]$ in the solution. Cl^- is a major anion in physiological environment and functions importantly in many fundamental biological processes, including regulation of intracellular pH gradients, maintenance of intracellular volume, and resting membrane potential.[22-25] Controlling $[Cl^-]$ in solution has great significance in regulating extra- and intra- cellular distribution of chloride, which influences cell growth and differentiation, metastatic conversion, patterning of innervation, and neuronal excitability in the central nervous system.[25-28]

Here, we control $[Cl^-]$ in solution by exploiting perhaps the best-known reference electrode, Ag/AgCl.[23, 29-32] We do so by driving the reaction $Ag + Cl^- \leftrightarrow AgCl + e^-$ out of equilibrium condition with a potential (V_{Cl^-}) on the Ag/AgCl contact to effectively transfer Cl^- across the contact/solution interface (Fig 18). While Ag/AgCl is a well-known system, the use of Ag/AgCl to control $[Cl^-]$ as an e^- to Cl^- transducer has yet to be reported to the best of our knowledge. Furthermore, we adapt Ag/AgCl contact to a bioelectronic device, a chloride modulator with a Chloride reservoir and a target chamber that is able to host cells. We use this Chloride modulator to demonstrate proof-of-concept actuation of membrane voltage (V_{mem}) on human pluripotent stem cells (hiPSCs).

2.1.1 Cl^- TO ELECTRON TRANSDUCER

First, we use an Ag/AgCl wire as a chloride transducer to show the ability of Ag/AgCl to control [Cl^-] in solution. We do so in a standard three-electrode configuration with the Ag/AgCl wire as working electrode (W), a glass Ag/AgCl as the reference electrode (R), platinum (Pt) wire as the counter electrode (C). Figure 19a describes how an anodic voltage, V_{Cl-}, transfers Cl^- from solution to the Ag/AgCl wire according to $Ag + Cl^- \rightarrow AgCl + e^-$ and thus reduces [Cl^-]. The excess e^- flows out of the Ag/AgCl contact into the lead. We use (N-(Ethoxycarbonylmethyl)-6-Methoxyquinolinium Bromide) (MQAE) to monitor [Cl^-]. MQAE is a diffusion-limited collisional Cl^--quenched fluorescent dye whose intensity decreases when [Cl^-] increases. We calibrate MQAE using the Stern–Volmer equation (Fig. 22) and quantify [Cl^-].[33] Figure 19b shows [Cl^-] decreases from 50 mM to 32 mM when $V_{Cl-} = 0.4$ V for 100 s. Figure 19c describes how a cathodic voltage, V_{Cl-}, transfers Cl^- from the Ag/AgCl wire to the solution according to $AgCl + e^- \rightarrow Ag + Cl^-$ and thus increases [Cl^-]. Figure 19d shows that [Cl^-] increases from 0 mM to 48 mM when $V_{Cl-} = -0.4$ V for 100 s. These ranges and changes for [Cl^-] are comparable to changes in [Cl^-] plasma, interstitial fluids, and intracellular fluids [22] and they are thus relevant for biological applications.

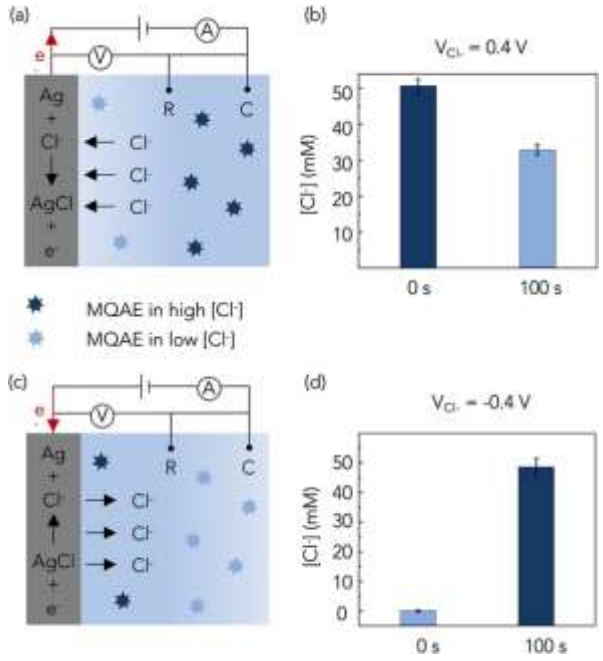

Figure 19: Schematic of prototype chloride transducer and working mechanism. This setup has a standard three-electrode configuration. MQAE is a fluorescence dye monitoring [Cl^-] change in solution, whose intensity increases with lower [Cl^-]. (a) Anodic voltage transfers Cl^- from solution into the Ag/AgCl contact, which decreases [Cl^-] and brightens MQAE. (b) [Cl^-] changes from 50 mM to 32 mM by applying 0.4 V for 100 s. (c) Cathodic voltage transfers Cl^- from the Ag/AgCl contact into solution thus increasing [Cl^-] and quenching MQAE. (d) [Cl^-] changes from 0 mM to 48 mM by applying -0.4 V for 100 s.

One of the advantages of using AgCl to transfer Cl^- to and from solution is the fact that AgCl is selective to Cl^- and is able to affect [Cl^-] in physiological conditions with little to no interference from other ions. To this end, we demonstrate that the Cl^- transducer works in a complex solution such as stem cell culture media (Neurobasal™-A Medium, ThermoFisher) that contains 79.6 mM NaCl, 26 mM $NaHCO_3$, and 0.9 mM KH_2PO_4.

With V_{Cl^-} = 0.6 V for 100 s, we are still able to remove Cl^- from solution and reduce $[Cl^-]$ from 79.6mM to 47 ±2 mM. Repeating the experiment without HCO_3^- and $H_2PO_4^-$ ions leads to the same result with the final $[Cl^-]$ = 46 ± 5 mM (Fig. 22). While we are not able to monitor the change in concentration of the other anions, these results indicate that the presence of other anions does not affect the Cl^- transducer indicating that AgCl is indeed specific to Cl^-. From our work with the AgCl wire, we found that transferring Cl from the Ag/AgCl contact into the solution is more efficient than transferring Cl from the solution to the contact. One of the reasons can be that when applying an anodic voltage, Cl^- are absorbed into Ag/AgCl electrodes immediately and a depletion area forms around the electrodes.[34] Then, the reaction is limited by Cl^- migration to the contact/solution interface. We further investigate the electrode kinetics of Ag/AgCl conversion in the next section to verify the hypothesis.

2.2.2 KINETICS OF THE CONVERSION BETWEEN Ag AND AgCl

To better understand and optimize the Cl^- transducer, we investigate the kinetics of Cl^- transfer at different potentials. Surprisingly, not many investigations on the kinetics of the conversion between Ag/AgCl under dynamic polarization or under other non-equilibrium exist.[35] For a Ag/AgCl electrode in solution containing Cl^-, the Cl^- in the AgCl are in equilibrium with the $[Cl^-]$ in solution. As such, a Ag/AgCl contact shows a lower electrode potential in a solution with higher $[Cl^-]$ and vice versa.[23] The well-known Ag/AgCl reference electrode takes advantage of this relationship by reading a constant potential when encapsulated in an internal electrolyte with a constant $[Cl^-]$.[36]

AgCl has been used as gate electrode in organic electrochemical transistors (OECTs), which utilized its faradaic reactions in halide electrolytes to achieve higher current modulation compared to Pt electrodes.[37] However, there are few work exploring the dynamic change of Ag/AgCl system. Little is known about the kinetics of the conversion between Ag and AgCl.[35, 38] Although people have reported the open circuit potential (OCP) and cyclic voltammetry (CV) of Ag/AgCl, the analysis about the conversion between e^- and Cl^- is absent. Here, we explore the kinetics of Ag/AgCl conversion of miniaturized on-chip Ag/AgCl nanoparticles (NPs) electrodes. We use Ag/AgCl NPs to create an interface with higher surface area and capacitance for better conversion efficiency.[39] The conversion between Ag/AgCl under non-equilibrium conditions is consistent with Cl^-/e^- transformation, which is critical for controlling [Cl^-] with electronic means.

We electroplate Ag NPs on thin-film Au contacts and chlorinate the Ag NPs into Ag/AgCl NPs in a 50 mM KCl solution (Fig. 24). The bare Ag/AgCl NPs electrode we make here is a "quasi-reference electrode", whose electrical potential depends on [Cl^-] in solution according to the thermodynamically-based Nernst relationship.

$$V_{Cl-} = V^0_{Cl-} - 0.059\, lg[Cl^-] \qquad (1)$$

where V^0_{Cl-} is the standard potential of Ag/AgCl.

Ag/AgCl conversion depends on [Cl^-] in solution and the applied potential (V_{Cl-}). Here we record the open circuit potential (V_{OCP}) of Ag/AgCl contact in various [Cl^-] solution under equilibrium conditions with a three-electrode configuration at room temperature.

Figure 19a shows the V_{OCP} of Ag/AgCl in 1 mM, 10 mM, 100 mM and 1 M KCl, respectively. V_{OCP} and logarithmic scale of $[Cl^-]$ shows a linear relationship with a slope of -55.35 mV and $R^2 = 0.999$, as expected from the Nernst equation. We use the values of V_{OCP} to define process map for the Cl^- transducer as a function of $[Cl^-]$ and V_{Cl^-} (Fig. 20a). The straight line in the graphs joins the V_{OCP}'s at different $[Cl^-]$ and represents equilibrium (as many Cl^- transfer from the solution into the electrode as they transfer from the electrode into the solution). This line also marks the threshold of the Ag/AgCl conversion. For a combination of V_{Cl^-} and $[Cl^-]$ in the gray area below the line, Cl^- transfer into the solution increasing $[Cl^-]$ and for a combination of V_{Cl^-} and $[Cl^-]$ above the line in the white area Cl^- transfer from the solution decreasing $[Cl^-]$.

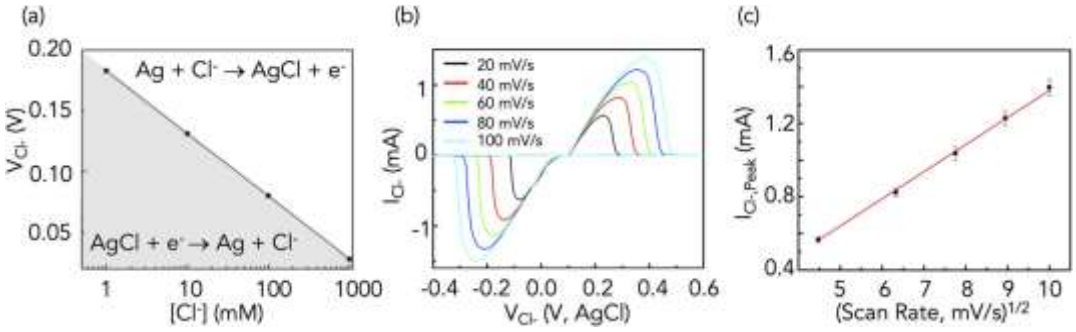

Figure 20: *Kinetics of the conversion between Ag/AgCl. (a) The linear relationship between V_{OCP} and logarithmic scale of $[Cl^-]$ represents equilibrium as well as the threshold of Ag/AgCl conversion. In the white area above the line, $AgCl + e^- \rightarrow Ag + Cl^-$; in the gray area under the line, $AgCl + e^- \leftarrow Ag + Cl^-$, (b) CV of Ag/AgCl electrodes with a series of scan rates, 20 mV/s, 40 mV/s, 60 mV/s, 80 mV/s, 100 mV/s. The redox peaks show that the reaction is electron transfer dominated, and the current increases with higher scan rate due to reduced diffusion layer. (c) Relationship of anodic peak*

current of Ag/AgCl ($I_{Cl^-,Peak}$) versus square root of the scan rate in CV measurements. The excellent linear relationship shows that the reaction is limited by the diffusion of Cl^- to the electrode following Randles−Sevcik equation. The standard error is derived from 3 electrodes.

To further study the electrode kinetics at the interface of Ag/AgCl contact and solution, we investigate the limiting mechanism of this electrochemical reaction (Fig 20b). In detail, we cycle the voltage of Ag/AgCl NPs electrodes between -0.8 V and 0.8 V, versus a glass Ag/AgCl electrode. Pt wire is the counter electrode as usual. We use a series of scan rates, 20 mV/s, 40 mV/s, 60 mV/s, 80 mV/s and 100 mV/s, respectively. Taking 40 mV/s as an example, the interfacial reaction can be explained as below. During the scan of V_{Cl^-} from 0 V to 0.8 V, Cl^- is absorb onto Ag/AgCl and oxidizes Ag to AgCl. I_{Cl^-} increases to a peak with higher V_{Cl^-} and then becomes smaller by the delivery of Cl^- from the bulk solution. Thus, the mass transport of Cl^- becomes the limitation of the electrochemical reaction, and the current decays gradually.[40] After the scan direction is switched to negative, V_{Cl^-} is still sufficiently positive to oxidize Ag, so I_{Cl^-} continues until V_{Cl^-} becomes strong enough to reduce AgCl. Then Cl^- starts to be released from the electrode, reaches a cathodic peak and decays as AgCl is consumed. With the scan rate increase, the diffusion layer becomes smaller and it takes less time to record one cycle, inducing I_{Cl^-} increases.[41, 42] The measured current in CV with a redox couple is mainly faradaic current, which is from the charge transfer at the interface of the electrode contact/solution and depends on the kinetics of charge transfer

at the surface and the redox species diffusion to the surface.[41] We plot the peak currents ($I_{Cl^-,Peak}$) of CV versus the square root of scan rates of 3 electrodes in Figure 25, which all show an extraordinary proportional relationship, and the standard error is shown in Figure 20c. According to Randles−Sevcik equation (Equation 2), the analytes, Cl^-, are not adsorbed on the electrode but freely diffused in the solution. Thus, we conclude that Ag/AgCl conversion is a Cl^--diffusion controlled reversible electrochemical reaction.[40]

$$I_{Cl-,Peak} = 0.4463nFAC(\frac{nFvD}{RT})^{\frac{1}{2}} \quad (2)$$

Where $I_{Cl^-,Peak}$, R, F, T are peak current of cathodic or anodic reaction, gas constant, Faraday constant, absolute temperature, respectively. A, C, D, v, are electrode area, concentration of the analyte, diffusion coefficient and scan rate of CV.

2.2.3 CHLORIDE MODULATOR WITH CELLS

As the translation between Cl^- and e^- is in parallel with the conversion between Ag/AgCl, which depends on V_{Cl^-} and $[Cl^-]$ in solution, we can feasibly adapt Ag/AgCl electrode to various bioelectronic devices and utilize it to selectively control $[Cl^-]$ in solution with V_{Cl^-}. Here we design a chloride modulator, which transfers Cl^- from a reservoir electrolyte with rich Cl^- source to a target electrolyte under control. The Ag/AgCl NPs are the working electrode. The selectivity of AgCl to Cl^- ensures it a storage media specifically to Cl^- and allows Cl^- to move between reservoir and target depending on V_{Cl^-}. Thus, the chloride modulator can manipulate $[Cl^-]$ in a much more

extensive range than a single Ag/AgCl contact. As proof-of-concept, we culture cells in the target chamber and study the effect of [Cl^-] modulation on their function.

Figure 21a shows the schematic of the chloride modulator (side view), and the design is similar to previously reported proton modulator with Pd/PdH_x electrodes.[19] The chloride modulator is composed of two independent chambers, referred as reservoir (left) and target (right), respectively, connected by an anion exchange membrane (AEM). Figure 21b shows the optical image of the device. Reservoir has 0.1 M KCl to provide a rich Cl^- source, and we change [Cl^-] of the target solution, which can contain 100 uM MQAE in DI water (Figure 21c), or cells (Figure 21d, e). We use an Ag/AgCl NPs microelectrode as the working electrodes, providing multiple independent openings for Cl^- to enter / leave the target solution. Here we define the potential different between Ag/AgCl and Pt electrode in reservoir as $V_{Cl-,R}$, the potential difference between Ag/AgCl and Pt electrode in target as V_{Cl-}. AEM is a polymer with high conductivity for anions due to their large amount of fixed cationic groups that support the storage and transport of mobile anions through the membrane, and its exclusion to cations ensures the majority of measured currents are from the moving of anions.[43] Here, AEM is a mixture of polyvinyl alcohol (PVA) and Poly (diallyldimethylammonium chloride) (PDDA), which work as the hydrophilic matrix and polycation, respectively. To avoid the undesirable passive diffusion current caused by the [Cl^-] gradient between reservoir and target, we pattern a thin cation exchange membrane (CEM), PVA and polystyrene sulfate acid (PSS) mixture at the opening of the MEAs to form a Donnan exclusion barrier. The AEM and CEM function together

to provide a bridge that allows for an electrophoretic Cl^- flow during stimulation with a voltage across the bridge and minimization of passive diffusion current. More details about device fabrication are in Figure 25.

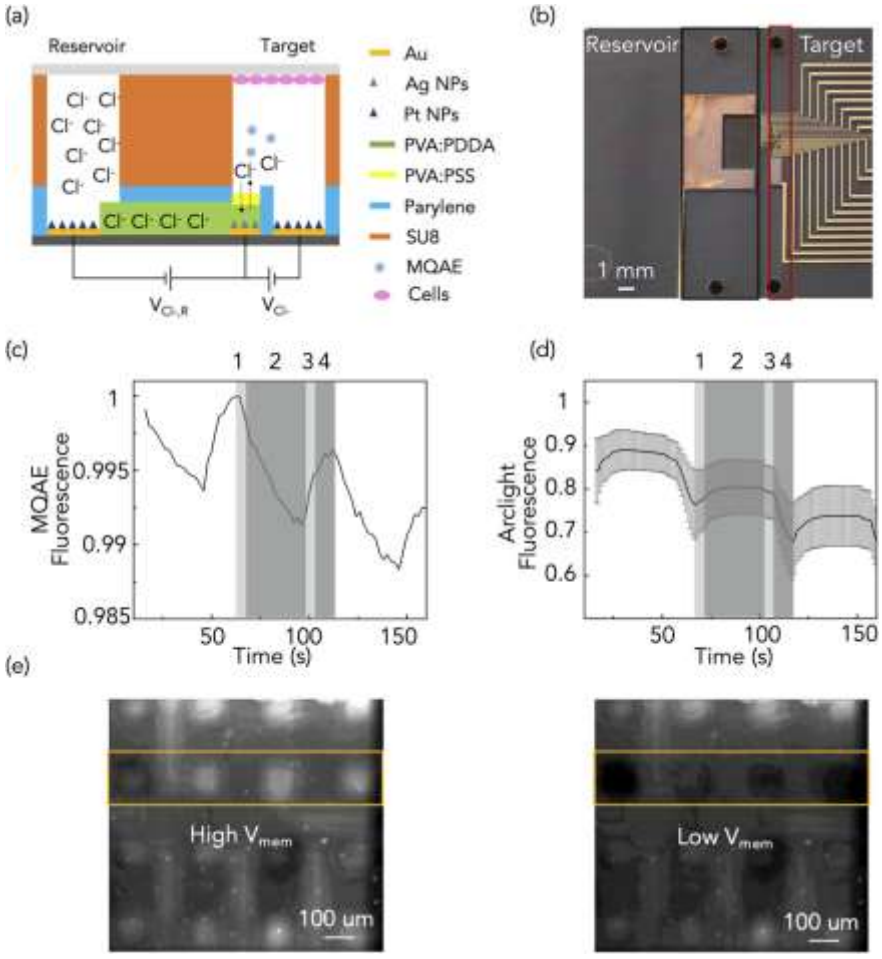

Figure 21: Chloride modulator. (a) Schematic of the chloride modulator (side view) and operating principle. Reservoir and target are connected by an anion exchange membrane (AEM), in which Cl^- are driven by $V_{Cl^-,R}$. Reservoir has a high [Cl^-] solution providing Cl^- source, and [Cl^-] in target is under control. (b) Optical image of the chloride modulator. The reservoir (black line) and target (red line) are separated by SU 8 microfluidic channels and the holes on the glass slide provides the inlet and outlet.

(c) [Cl^-] change results from the 4-step process in Table 1 for 3 cycles, which is indicated by the MQAE fluorescence intensity. Temporal change corresponding to each step is shown with different colors in the second cycle as a representation. (d) V_{mem} change of cells results from the same operation is indicated by ArcLight fluorescence intensity. The data come from 3 devices. (e) Fluorescence images of the cells over MEAs with high V_{mem} (t = 75 s) and low V_{mem} (t = 119 s). The highlighted row is under operation.

Table 1: 4-step process that modulates [Cl^-] in target solution

	Step	$V_{Cl-, R}$ (V)	V_{Cl-} (V)	Time (s)	[Cl^-]
1	Transfer Cl^- from Reservoir to AgCl	2	0	5	High
2	AgCl release Cl^- to Target	0	-1.5	30	High
3	Remove Cl^- from AgCl to Reservoir	-1	0	5	Low
4	AgCl absorb Cl^- from Target	0	1	10	Low

We design a 4-step process in Table 1 to control [Cl^-] in target solution periodically by driving Cl^- from and back to the reservoir, which results in the [Cl^-] changes shown in Figure 21c. The Cl^- modulator also achieves diffusion limited spatial resolution with larger [Cl^-] changes occurring close to the contacts that are active, with little or no [Cl^-] changes observed in the non-active region (Fig. 28).

As proof-of-concept, we used the chloride modulator to study the effects of extracellular [Cl^-] on human pluripotent mammalian stem cells (hiPSCs) and their V_{mem} (Figure 21d and e). A cell's resting potential, V_{mem}, is an electrical control signal that occurs between the inside of the cell and the extracellular environment.[44] V_{mem} affects cell physiology and functions such as proliferation, differentiation, migration and apoptosis, as well as cell-cell communication, and large-scale morphogenesis.[45]

Chloride is the major anion in extracellular environments. In hiPSCs, an increase in extracellular [Cl^-] results in cell hyperpolarization (higher V_{mem}), and a decrease in extracellular [Cl^-] results in cell depolarization (lower V_{mem}).[46] We measure V_{mem} of the hiPSCs using ArcLight, a fluorescent reporter that we expressed on the cell membrane, whose fluorescence intensity increases when V_{mem} increases.[47] By switching the environment between high [Cl^-] and low [Cl^-] conditions using the same protocol in Table 1, we observe that V_{mem} of hiPSCs shifts with the expected pattern as measured by the ArcLight fluorescence intensity (Figure 21d). Figure 21e shows the fluorescence images of the cells at t = 75 s and t = 119 s, corresponding to high (hyperpolarized) and low V_{mem}(depolarized), respectively. This change in fluorescence occurs close to the activated area and not far away from the active electrodes indicating that the induced change in [Cl^-] is responsible for the measured V_{mem} change. While this is a proof-of-concept, it shows how the Cl^- modulator is able to affect cell function.

2.2.4 CONCLUSION

Ag/AgCl is a well-known reference electrode that has been used in electrochemistry for decades. Here we first demonstrate Ag/AgCl as a Cl^- transducer that controls $[Cl^-]$ by transferring Cl^- from and to solution controlled by an applied voltage, V_{Cl-}. Furthermore, we investigate kinetics of the conversion between Ag/AgCl by electrochemical techniques, which is consistent with Cl^-/e^- transformation and critical for controlling $[Cl^-]$ with electronic means. This control paves the way to the integration Ag/AgCl into complex bioelectronic devices, for dynamic control of bioelectric signaling in vivo and in vitro models of physiology and morphogenesis. As a proof of concept, we adapt Ag/AgCl into a chloride modulator that precisely regulates $[Cl^-]$ in solution and affect membrane voltage of pluripotent stem cells. Since Cl^- is a critical anion in bioelectricity, the accurate regulation of $[Cl^-]$ is currently in high demand and has potential in bioelectronic therapies.

2.2.5 METHODS

MQAE calibration in PDMS well: We use Keyence fluorescence microscope to take images of MQAE solution in the PDMS wells using DAPI filter, and ImageJ to analyze the fluorescence intensity. According to Stern–Volmer equation (Equation 1), $[Cl^-]$ shows linear relationship with ($F_O/F - 1$) between 0 – 100 mM.[158] We did the calibration by making 100 uM MQAE solution in 0 mM, 2 mM, 8 mM, 10 mM and 50 mM KCl solution and measure the fluorescence intensity with the same imaging parameters, as shown in Figure 22. We're able to convert the intensity of the MQAE to $[Cl^-]$ to estimate the $[Cl^-]$ in the solution.

$$\frac{F_O}{F} - 1 = K_{SV}[Cl^-] \text{ (1)}$$

where F_O is the fluorescence intensity without Cl^-; F is the fluorescence intensity in the presence of Cl^-; K_{SV} is the Stern–Volmer constant.

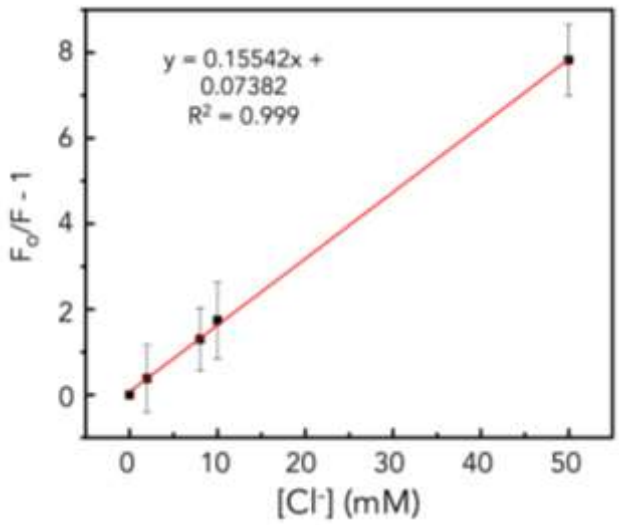

Figure 22: Stern–Volmer plot for quenching of MQAE by chloride. The volume of the solution is 20 µL.

Selectivity of AgCl to Cl^-:

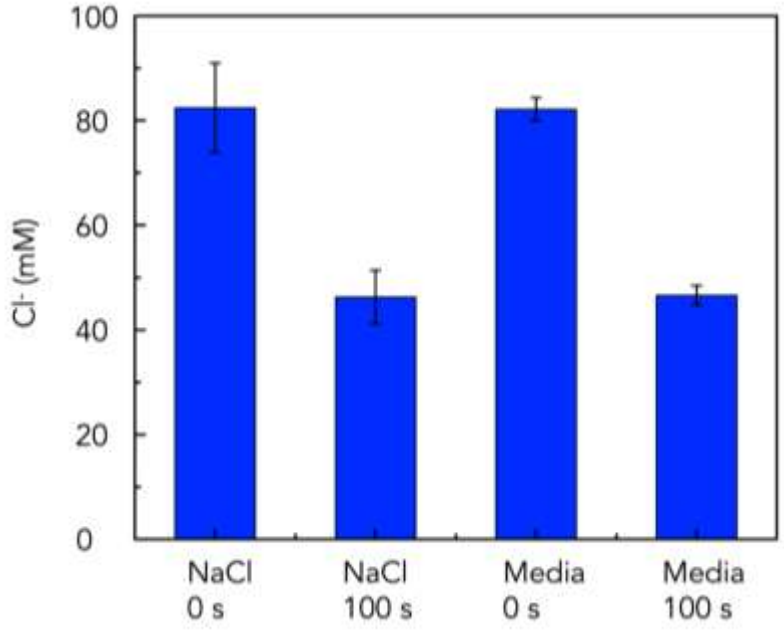

Figure 23: Selectivity of AgCl to Cl- in stem cell culture media

Electroplating Ag/AgCl NPs: Figure 24(a) shows that silver chloride nanoparticles (Ag NPs) are electroplated on top of thin-film gold contacts on glass (2*2 mm^2). The electroplating process is accomplished from 10 mM $AgNO_3$ in 0.1 M KNO_3 using a three-electrode configuration at room temperature. An Ag/AgCl pellet serves as reference electrode, and a platinum wire coil serves as counter electrode. The following procedure yields the most repeatable and stable results among several plating procedures tested. First, we applied -0.3 V on Au contact for 150s and the surface becomes silver white color. In this process, approximately 0.005 C charges are measured in the circuit, which theoretically equals to the amount of Ag^+ deposited. Then, we oxidize approximately 20% Ag NPs to AgCl NPs by applying a constant anodic current (100 uA) for 10s on Ag NPs in 50 mM KCl solution at room

temperature. We observe a clear color change from silver white to dark grey indicating the formation of AgCl NPs. Furthermore, we inspect the surface morphology with scanning electron microscopy (SEM). Figure 24(b) shows Ag NPs electroplated here, which uniformly covers the whole electrode surface. With higher magnification, it shows the signature cubic geometry of Ag NPs with 200 nm grain size in Figure 24(c). Figure 24(d) shows 20% chlorinated Ag/AgCl NPs. It's clear that an additional layer is visible on top of Ag NPs, and the grain of AgCl NPs is more amorphous with approximately 500 nm size. With further chlorination of Ag NPs (40%), the SEM image in Figure 24(e) shows more AgCl NPs.

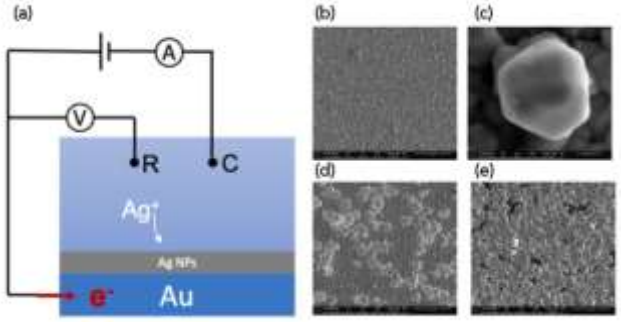

Figure 24: (a) Ag/ AgCl NPs electroplating and chlorination. (b-e) Morphology of Ag/AgCl NPs by SEM images of (b) Ag NPs after electroplating; (c) single Ag NPs with the signature shape; (d) Ag/AgCl with 20% chlorination; (e) Ag/AgCl with 40% chlorination.

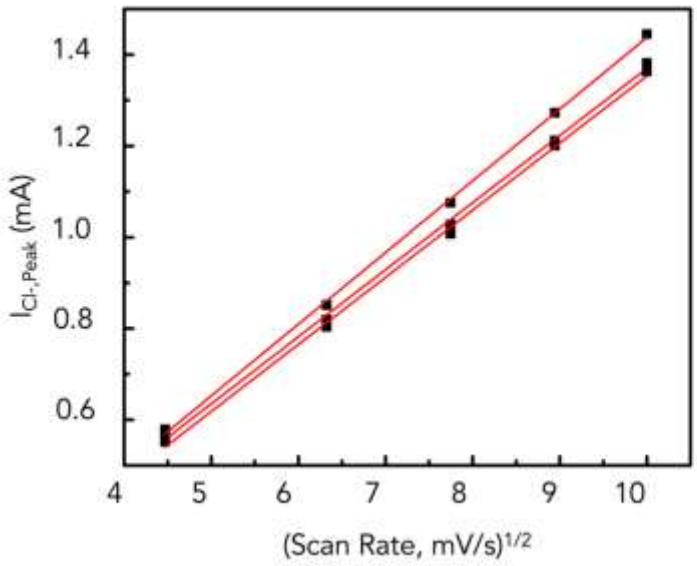

Figure 25: Relationship of anodic peak current of Ag/AgCl ($I_{Cl-,Peak}$) versus square root of the scan rate in CV measurements of 3 AgCl NPs electrodes, which all show excellent linear relationship.

The slight difference of the slope is from the surface area difference of each electrode according to Randles−Sevcik equation, which happens in the AgCl NPs deposition process.

Device Fabrication: Micrometer size Cl^- modulator was fabricated using photolithography. Glass slides were sonicated for 20 min in 80% v/v acetone and 20% v/v iso-propanol (IPA), and dried with N_2. S1813 (Dow chemicals) photoresist was deposited on top of the glass substrates, following standard protocols (spin-coated at 3000 rpm, baked 1 min. at 110 °C) to create the Au patterns. Ti 10 nm and Au 100 nm were evaporated using an e-beam evaporator, and a lift-off process (sonication in 80%

v/v Acetone and 20% v/v IPA for 5 min) defined the metal contacts and interconnects. An additional S1813 process defined the area of the Au contacts for electrodeposition of Ag/AgCl NPs and Pt NPs, while the metal interconnects were insulated. Then, a 1.4 μm insulating layer of parylene-C was deposited (Specialty Coating Systems Labcoter 2 system) in the presence of A174 adhesion promoter in the deposition chamber. The parylene was etched with an oxygen plasma at 200 W with the regions over the electrodes and contact pads exposed, and the interconnecting regions protected by a thick positive photoresist (SPR220-4.5, Micro-Chem Corp.). Prior to deposition of polymer, wafers were treated with the a 5% solution of (3-Glycidyloxypropyl)trimethoxysilane (GOPS) in ethanol via spin coating at 1000 rpm for 30 s and then baked at 110C for 5 minutes to promote adhesion of the polymer. The AEM is a blend of 10 wt% polyvinyl alcohol (PVA) and 20 wt% Poly (diallyldimethylammonium chloride) (2:1 weight ratio), which was thoroughly mixed (PVA: PDDA solution) and sonicated for 45 min. The PVA: PDDA solution was filtered with a filter porous size of 0.8 μm and was spin-coated on top of the samples at 1500 rpm for 30 s and baked in 120 °C for 2h, yielding a film thickness of 2 um. The PVA: PDDA AEM was etched with an oxygen plasma at 200 W with the desired pattern defined with SPR220-4.5 photoresist. A second 1.4 μm coating of parylene was then deposited with the same protocol as above to insulate and protect the ion bridge from the subsequent steps. To promote adhesion between the parylene and SU8 photoresist, GOPS was again deposited using the above process prior to SU8 patterning. SU8 was spun onto the wafer at a speed of 1000 rpm for 30 s and a ramp of

300 rpm, microfluidic channels of height 40 μm were patterned forming the sidewalls reservoir and target chambers. The parylene insulation layer protecting the ion bridge openings in the reservoir and target channels were defined and etched using the same process as the previous parylene etch. Then, a mixture of 8%wt polyvinyl alcohol (PVA) and 2% polystyrene sulfonic acid (PSS) in water was then passed through a 0.8 μm MCE syringe filter and spin coated at 3000rpm for 30s followed by baking at 120C for 2 hours. The polymer film was patterned in SPR220 photoresist and etched with O2 reactive ion etching. Finally, Single sided microfluidic diagnostic tape (3M 9956) was cut by CNC machine to make the openings over AgCl MEA for imaging and then aligned to features on the device and pressed to seal the microchannels by hand.

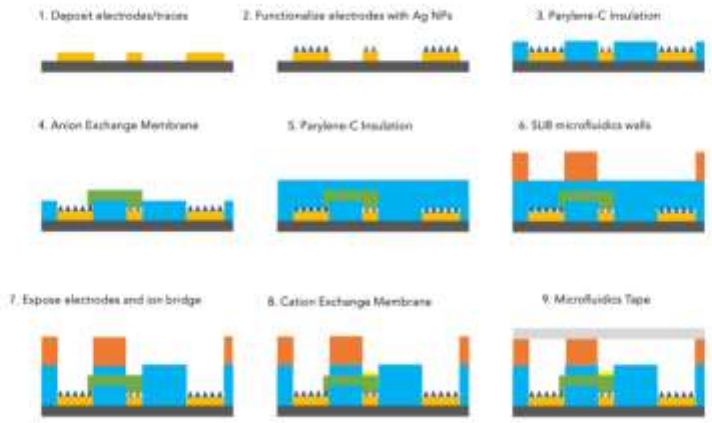

Figure 26: Fabrication scheme for the proton pump array. (1) E-beam deposition of Au electrodes and traces. (2) Electrochemical deposition of Pd and Ag on the electrodes, followed by chlorination of Ag to form AgCl. (3) Parylene-C deposition. (4) Spin-coating of PVA: PDDA AEM and etching. (5) Parylene-C deposition. (6) SU8 patterning to form microfluidic walls. (7) O_2 etch of Parylene-C to expose the ion

bridge and the AgCl electrodes. (8) Spin-coating and patterning of the PVA: PSS CEM. (9) Sealing the fluidics with a thin microfluidic tap.

Electrodeposition of platinum nanoparticles: Pt NPs are electrodeposited on top of the Au contacts of two auxiliary electrodes by using 0.5 mg / ml H_2PtCl_6 water solution with a constant voltage of −0.06 V for 20 s and 160 s, respectively. Commercial Ag/AgCl electrode is used as a RE and Pt wire was used as a counter electrode (CE).

Device operation: We assemble the chloride modulator on an acrylic support rig that allows for low pressure clamping of a PDMS slab over the opening of the target microfluidics channel. The acrylic rig also provides a pogo-pin interface for connecting to a custom stimulation board that can stimulate eight independent channels simultaneously.

The custom design stimulation unit is used to stimulate eight individual channels. Each channel has an output range of -4 to +4V with a resolution of 1.95 mV, and the current measurement range from -1.6 to +1.6 uA with a resolution of 0.8 nA. Also, the stimulation unit has an open-circuit feature where it can completely disconnect some channels without changing the experiment setup. The stimulation has two operating modes: (1) standalone - the unit follows a pre-program protocol (2) networking mode - the unit waits for a command from an external controller (e.g., Machine learning algorithm) via a wireless connection.

Spatial resolution of the Cl- modulator:

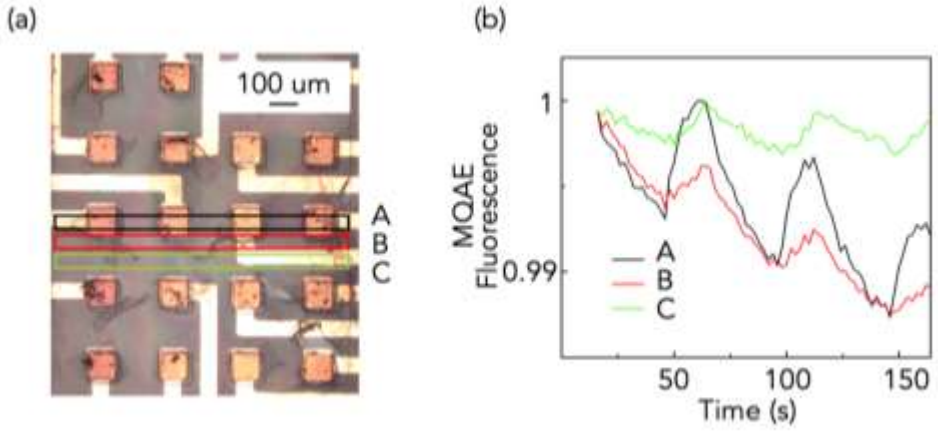

Figure 27: Diffusion limited spatial resolution of the Cl^- modulator.

In Figure 27, we activate microelectrodes in area A, and analyze [Cl^-] distribution in area A, B, C. When we transfer Cl^- from reservoir to target solution, [Cl^-] change in area B is slightly less than that in area A, because there are sufficient Cl^- supply from reservoir. However, it shows much less change when transferring Cl^- from target solution to the reservoir, because the reaction to absorb Cl^- from target solution is confined by Cl^- diffusion from area B to area A. Moreover, when the distance gets further to area C, [Cl^-] change is significantly less and shows temporal delay compared to that in area A.

Cells: hiPSCs were a generous donation from David Kaplan's group (ND418566, NINDS Human Genetics and DNA Cell Line Repository[156]. Stem cells were maintained at 5% CO_2 in StemFlex Medium (A3349401, ThermoFisher) on hESC Qualified Matrigel Matrix (354277, Corning) coated plates with the dilution

recommended by the manufacturer. Cells were disassociated with TrypLE Select (12563029, ThermoFisher). Transgenic cells were made by transfecting 500 ng of plasmid via 1 µL of lipofectamine 3000 (L3000008, ThermoFisher) per well of 24 well plate containing 500 µL of Opti-MEM (31985062, ThermoFisher) with 1X RevitaCell (A2644501, ThermoFisher). Reagent was removed after 4 hrs and replaced with StemFlex. Cells were allowed to recover for 3 days before being selected with 50 µg/mL G418 in StemFlex with 10 µg/mL ROCK inhibitor Y-27632 (72304, STEMCELL Technologies). After selection, a stable, clonally pure line was made by serial dilution using StemFlex with 1X RevitaCell. Clones were expanded in StemFlex and then assayed for alkaline phosphatase activity (SCR004, Millipore). The clone with best membrane localization and expression of ArcLight was chosen for further experimentation and frozen down using NutriFreez D10 (05-713-1E, Biological Industries). Prior to being used in experiments, hiPSC ArcLight cells were plated in mTeSR1 no phenol red (05876, STEMCELL Technologies) and allowed to expand for two passages prior to seeding on PDMS slabs that were coated in hESC Qualified Matrigel Matrix. Slabs were used in bioelectronic chips one to three days after seeding. Cells were perfused with mTeSR1 no phenol red during experiments.

Plasmid Construction: A pENTR1A plasmid with a CAG promoter and multiple cloning site followed by a SV40 poly A was used to clone in the mammalian codon optimized ArcLight Q239 from the plasmid CMV ArcLightCo (Q239)-T2A-nls-mCherry, a gift from Vincent Pieribone (Addgene plasmid # 85806 ;

http://n2t.net/addgene:85806 ; RRID:Addgene_85806). Cloning was done by In-Fusion HD Cloning Plus (638909, Takara) with HindIII and SalI restriction enzyme sites added. PCR was done using PrimeSTAR GXL DNA polymerase (R050A, Takara). The resulting pENTR1A CAG ArcLightCo construct was then Gateway LR clonased (11791020, ThermoFisher) into the hyperactive piggyBac transposase-based, helper-independent and self-inactivating delivery system, pmhyGENIE-3 containing a neomycin resistance gene in the backbone for selection, a gift from Stefan Moisyadi[157]. The resulting plasmid HypG3NeoBBArcLightCo (Q239) was used for subsequent transfections.

Reproduced from [159]

3. ACTUATORS FOR WOUND HEALING: IONS AND BIOMOLECULES

3.1 DELIVERY OF K+ FOR IN VITRO APPLICATIONS

3.1.1 INTRODUCTION

Bioelectronics bridges the gap between biology and electronics in sensing and actuation.[3-6] One of the main challenges for bioelectronic devices is translating ionic currents prevalent in biology to electronic signals and vice versa. This is because signal transmission in biological systems relies on the movement of ions and biomolecules instead of electrons and holes.[31-33] Ion pumps address this issue by translating currents to the flow of a particular species of ions and biomolecules at the device level.[35-37] They facilitate the movement of ions and molecules with an induced electric field[38]

and have various applications such as reducing inflammation[3], treatment of epilepsy[4], influencing cell differentiation[39], and promoting wound healing.[40]

The potassium ion is of great significance in biological systems.[160] It plays a vital role in cell membrane physiology, particularly in maintaining cell membrane potential (V_{mem}) and generating action potentials.[161] Propagating waves of potassium have also been shown to trigger the conductance of long-range electrical signals in bacterial colonies.[44] The active transport of potassium ions across the cell membrane is essential to nerve function.[160, 162] Potassium ions are also important in maintaining cardiovascular function.[163]

Cell-based in vitro studies are increasingly becoming popular with applications in drug discovery, tissue engineering, and regeneration due to their lower cost and ease of standardization compared to in vivo studies.[164] There is a need to develop bioelectronic systems to interface with and control these in vitro systems.[165]

This work presents two bioelectronic potassium ion pumps that modulate the ion concentration for in vitro cell culture. The first ion pump is designed to integrate directly with 6-well cell culture plates for optimal ease of integration with in vitro cell culture and is fabricated using simple replica molding with polydimethylsiloxane (PDMS) and 3D printed molds. The second on-chip ion pump evolved from the first ion pump with an on-chip cell culture chamber and a 3 x 3 microchannel array to interact with cells with a high spatial resolution of K^+ delivery and is fabricated using photolithography with SU-8. The on-chip ion pump eliminates a cell culture plate and provides a continuous flow of cell culture media for long-term cell activity monitoring.

3.1.2 RESULTS AND DISCUSSION

The PDMS-based bioelectronic ion pump [Fig. 28(a)] is placed in a 3D-printed adapter that fits directly into a 6-well cell culture plate. This increases the ease of integration of the ion pump with in vitro cultures [Fig. 28(b)]. The ion pump transfers potassium ions from a reservoir to a target with a voltage ($V_{K+,}$ typically between 0.5V and 2V) applied between a working electrode (WE) and a reference electrode (RE). The target refers to the well in a 6-well cell culture plate. A capillary filled with an anionic hydrogel selectively transports cations between the target and the reservoir[94],[166] [Fig. 28(c)]. In the reservoir, K^+ comes from KCl salt (1 M) that exists in solution mainly as K^+ and Cl^- (stability constant, log K = 0.10 at 25 °C).[167] For a positive V_{K+}, the negative Cl^- is attracted to the Ag surface of the WE. When Cl^- reaches the Ag surface, it oxidizes to Cl. Subsequently, the Cl physisorbs onto the Ag surface to form AgCl. The resulting K^+ is then pushed by the electric field from the reservoir containing the WE into the target through the capillary [Fig. 28(d)]. Simultaneously at the RE, the AgCl undergoes reduction to form Ag.

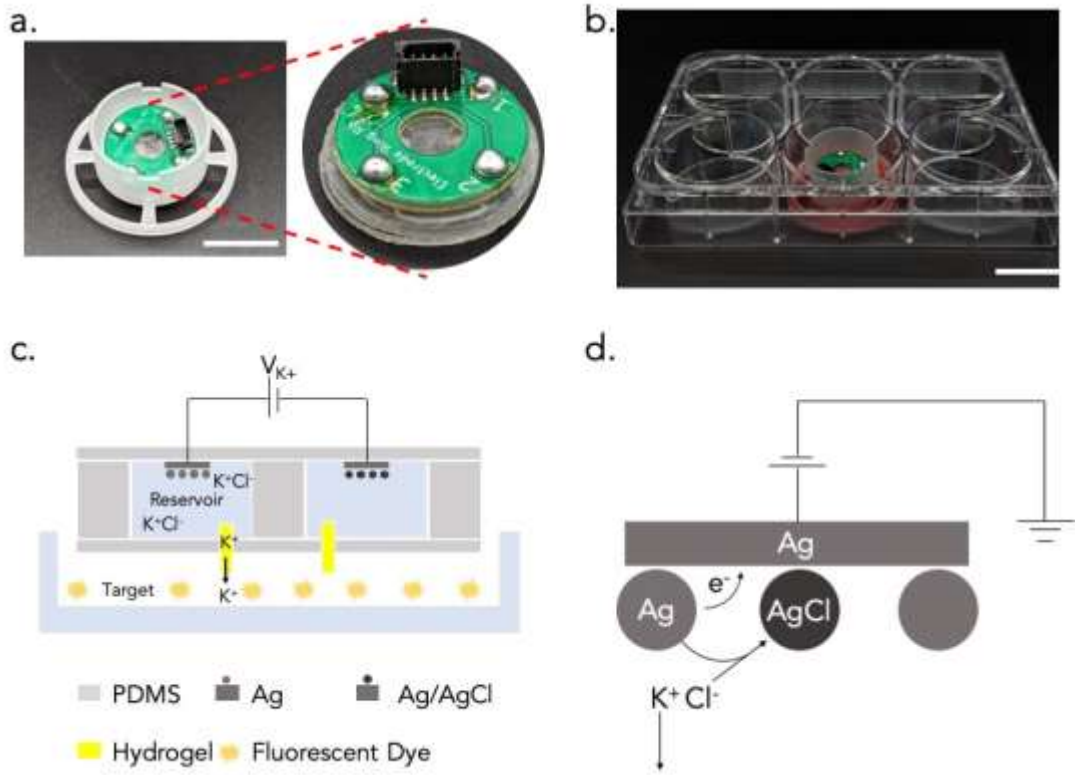

Figure 28: (a) Image of the ion pump with the adapter. Scale bar 1 cm. (b) Image of the device and adapter in a six-well plate. Scale bar 1.5 cm. (c) Schematic of the ion pump. (d) Reactions taking place at the working electrode.

We set up the well plate under a fluorescence microscope (Keyence BZ-X710) to demonstrate and monitor K^+ delivery from the ion pump in real time [Fig. 29(a)]. The target now consists of a solution of ION Potassium Green-2 dye. This dye changes fluorescence intensity linearly with changes in [K^+] [Fig. 29(b)]. We applied 5 alternating pulses of V_{K+} of +1.5 V and -1.5 V with each voltage applied for 2 minutes at a time. The positive voltage is to push K^+ from the reservoir to the target, while the negative voltage is to move cations in the opposite direction. The current produced

upon applying V_{K+} was recorded and is presented in Fig. 29(c). An electron is transferred from the RE to the WE for each ion being delivered. To measure the amount of K^+ delivered, we recorded the change in fluorescence intensity of the target during the course of actuation. An increase in $[K^+]$ is indicated by an increase in the fluorescence intensity of the dye [Fig. 29(d)]. We then calculated the amount of K^+ delivered to the target by calibrating the fluorescent dye with solutions of known $[K^+]$. We use the current and fluorescence intensity to determine the amount of charge transferred, and potassium ion delivered, respectively to calculate the delivery efficiency. The efficiency is given by the following equation:

$$Efficiency = \frac{Number\ of\ moles\ of\ ions\ delivered}{Number\ of\ moles\ of\ electrons\ transferred} \times 100\ \%$$

We calculated that potassium ion was delivered with an efficiency of approximately 33% across all devices tested.

To study the effect of V_{K+} on the delivery dosage of K^+, we actuated the pump with various voltages from 0.2 V to 1.2 V and recorded the current produced by actuation. The ion pump produced a steady state current of approximately 8 μA for an actuation voltage of 1.2 V. In contrast, it produced a steady state current of approximately 3 μA for an actuation voltage of 0.2 V [Fig. 29(e)]. This is consistent with our expectation that a higher V_{K+} would result in a higher current since the ion pump behaves as an

ionic resistor. This higher current, in turn, results in more K^+ delivered from the reservoir to the target.

Another factor that could affect the amount of potassium ion delivered is the concentration of the solution used in the reservoir. To study the effect of reservoir concentration on potassium ion delivery, the reservoirs were filled with 100 mM KCl and 1 M KCl. We applied a series of actuation voltages between 0.2 V and 1.2 V to the ion pump with a 100 mM KCl reservoir. We observed that the currents produced by the ion pump with a 1 M KCl reservoir are higher than the currents produced by the pump with a 100 mM KCl reservoir [Fig. 29(f)]. For an applied voltage of 0.2 V, the pump with a 1 M KCl reservoir showed a current of approximately 3 μA while the pump with a 100 mM KCl reservoir showed a current of 0.05 μA. This indicates that having a higher concentration solution in the reservoir results in a higher current produced for the same applied V_{K+}, which in turn increases the amount of K^+ delivered.

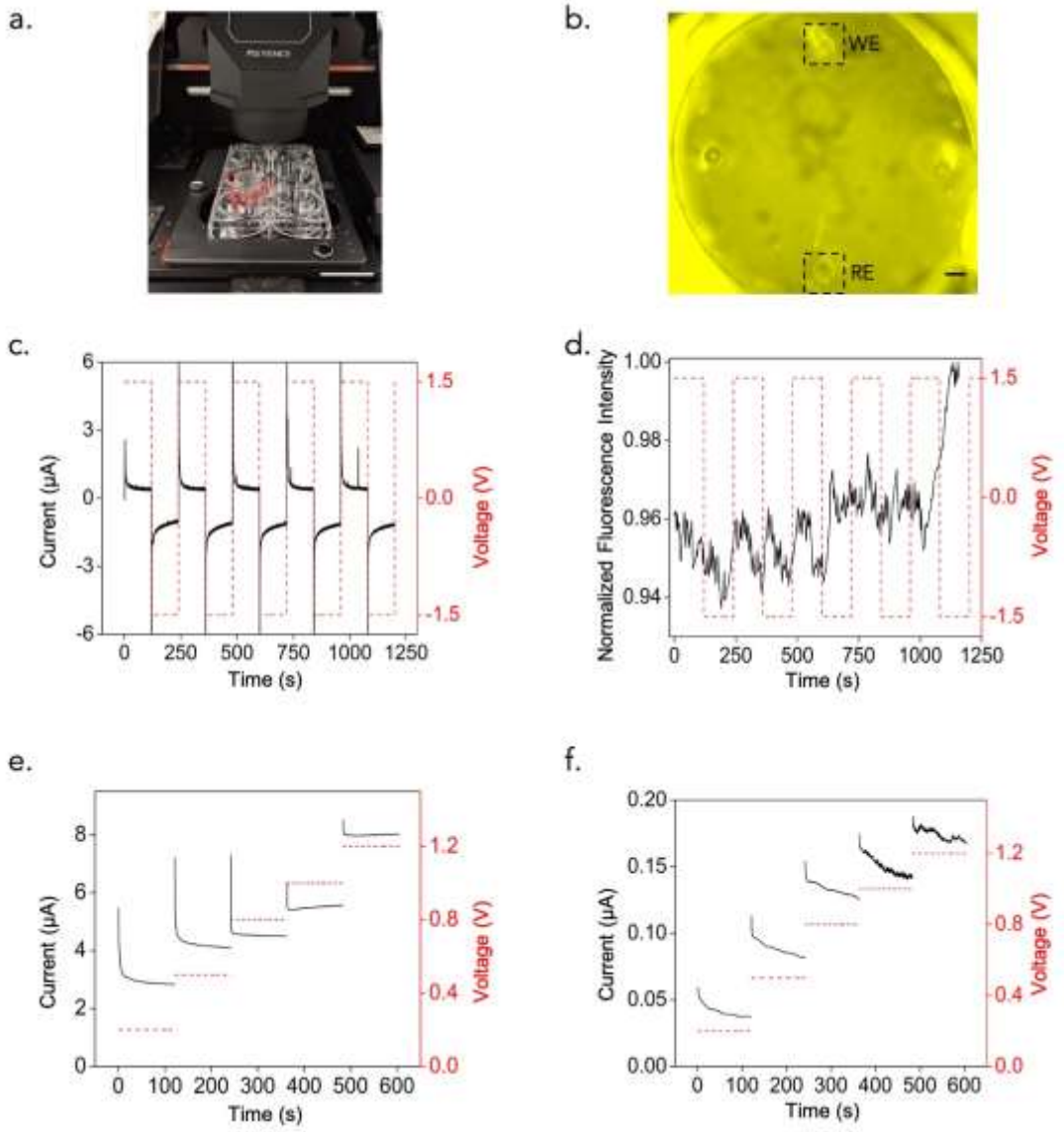

Figure 29: (a) Experimental setup of the ion pump. The ion pump is inserted in a 6-well cell culture plate containing fluorescent dyes as the target and is placed under a fluorescence microscope for real-time imaging during actuation. Scale bar 3.5 cm. (b) Fluorescence microscope image of the target area with working and reference electrodes. Scale bar 100 μm. (c) Current response of the device to an applied voltage. (d) Fluorescence response of the device to an applied voltage. (e) Current response of

the device to a series of voltages applied. Reservoir contains 1 M KCl. (f) Current response of the device to a series of voltages applied. Reservoir contains 100 mM KCl.

After successfully demonstrating K^+ delivery, in order to achieve spatial resolution of delivery, we developed another design of the ion pumps. This pump consists of two layers of SU-8 bonded together to create microfluidic channels on a glass substrate, which are then filled with the positive ion transporting hydrogel [(Fig. 30(a)- 30(b)]. The channels create a 3 × 3 array of 100 μm diameter pixels set 250 μm apart in the center of the chip, opening up to a well [Fig. 34]. Each of these pixels can be independently actuated and controlled resulting in a high spatial resolution. A PDMS cap with an 8 mm × 1 mm × 0.1 mm microfluidic chamber that inserts into this well acts as our target [Fig. 35]. The cap is used to externally culture cells in the fluidic chamber and can be inserted into the well on the device to integrate the cells with the device. The cap has an inlet and outlet to connect to flow systems for media access to the cells, thus maintaining continuous flow for long-term cell culture.

We characterize the pump by applying alternating pulses of +1 V and -1 V between the WE and the RE. Upon applying a positive $V_{K+,}$ potassium ions are delivered from the reservoir to the target through the hydrogel. The pump produced a steady state current of approximately 3 μA for the applied voltage [Fig. 30(c)]. The target was filled with ION Potassium Green-2 solution and imaged in real-time under a fluorescence microscope to observe the change in fluorescence intensity. As reported in Fig. 30(d),

we observe an increase and decrease in fluorescence intensity corresponding to the voltage applied.

To further characterize the spatial resolution of the device, we used a COMSOL Multiphysics model to model the diffusion of K^+ from a 100 μm pixel over time (diffusion coefficient of K^+ = 1.9 X 10^{-9} m^2s^{-1} at 25 °C).[168] The COMSOL model describes the behavior of K^+ injected from a 1μA current and assumes diffusion is dominant in the system. This is expected because the voltage drop occurs primarily across the hydrogel channel. A 1μA current was used since this current value was achievable by all the devices tested. A 10^{-4} cm^3 volume describes the area in the cell-culture microfluidic immediately around the array where the diffusion is simulated.

Fig. 30(e) shows the diffusion of K^+ concentration distribution after 100 ms. There is a high-resolution K^+ concentration gradient around the ion pump pixel from a 1 μA pulse for 100ms. The area right above the pixel shows a [K^+] of 2.5mM which gradually diffuses out to a concentration of 1mM. Fig. 30(f) shows the diffusion 10 s after actuation. The [K^+] directly above the pixel has now dropped to 3.37 μM. We observe that the change is still the strongest right above the pixel and gradually diffuses out away from the pixel. This is consistent with our assumption that diffusion is dominant during pumping.

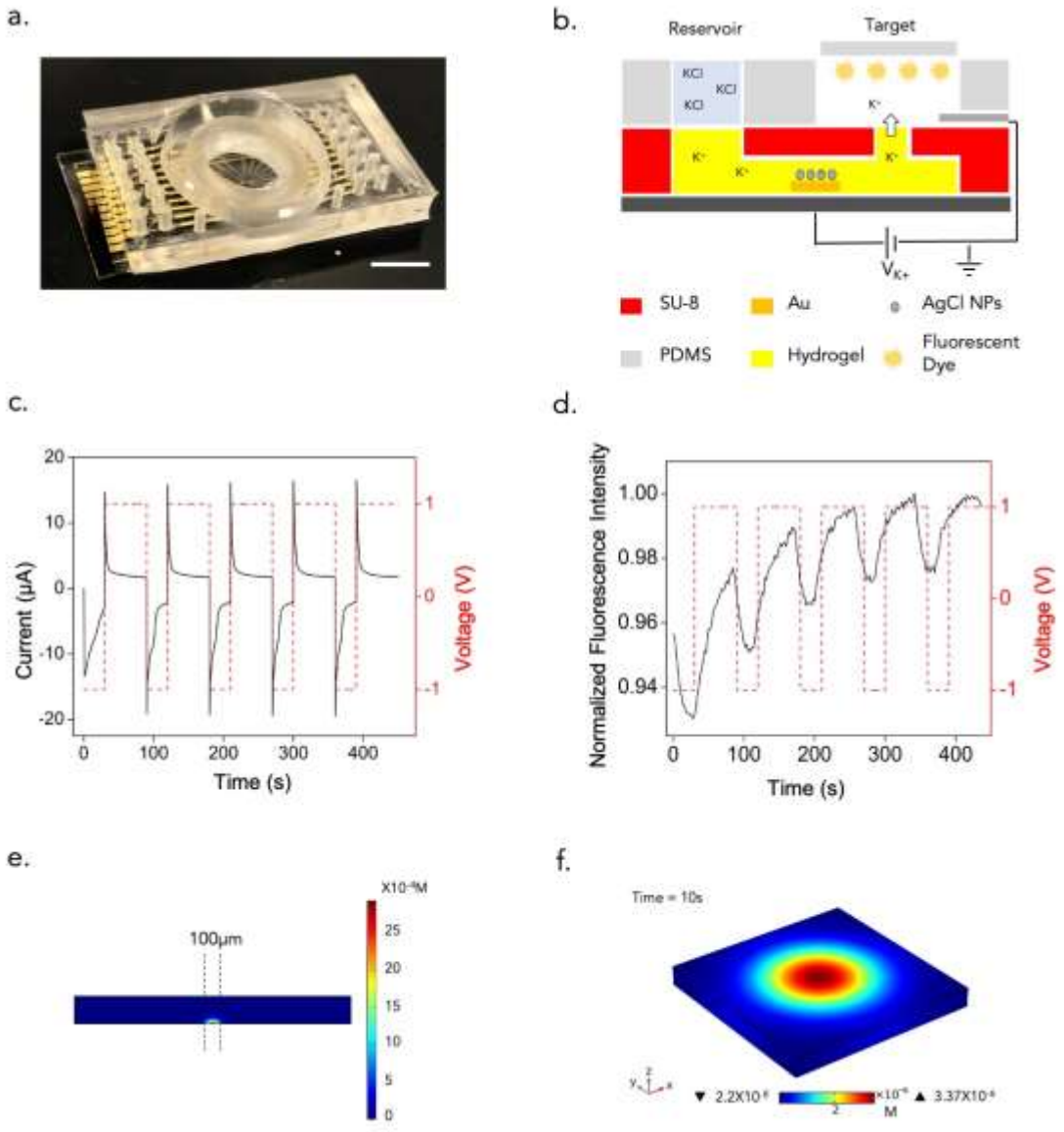

Figure 30: (a) Image of the device. Scale bar 5mm. (b) Schematic of the ion pump. (c) Current response of the device to an applied voltage pulse. (d) Fluorescence response of the device to an applied voltage pulse. (e) COMSOL simulation result showing the change in concentration after 100ms of delivery. (f) COMSOL simulation result showing the change in concentration after 10 s of delivery.

To demonstrate the application of these devices for in vitro cell culture, THP-1 macrophages were cultured in the chamber of the PDMS caps, which were then inserted into the device and clamped to seal. This provides a closed path for the continuous flow of media and prevents leakage. THP-1 cells were chosen based on previous work done by Li et al. in demonstrating the effect of potassium channels on macrophage polarization.[43] The setup [Fig. 35] was placed in an on-stage incubator on a fluorescence microscope and connected to an ElveFlow flow system for media. $DiBAC_4(3)$, a membrane voltage (V_{mem}) sensitive dye, was flown into the chamber. DiBAC changes its fluorescence intensity with a change in V_{mem} – an increase in intensity corresponds to increased cell depolarization.

Fig. 31(a) shows an image of the macrophage cells distributed in the chamber before actuation. The cells were actuated by delivering K^+ using the ion pump. V_{K+} of 0.8V was applied for 20 minutes, and 0V was applied for 20 minutes over 2.5 hours. This actuation protocol was selected based on results observed by Selberg et al.[39] Over the course of actuation, the fluorescence intensity of DiBAC increased [Fig. 31(b)]. This indicates the depolarization of the cells. Fig. 31(c) plots the fluorescence intensity of DiBAC at various time points during actuation, and we see that over time, there is an increase in the intensity of DiBAC, indicating a change in the membrane voltage resulting in the depolarization of these cells.

To be able to apply these ion pumps effectively to biological systems, it is essential to be able to control the concentration of ions being delivered precisely.[39, 159, 169, 170] As a proof of concept for integrating these ion pumps with closed-loop control, a machine-

learning-based closed-loop control algorithm was implemented. The algorithm and architecture used is similar to the ones implemented in an earlier work by Jafari et al.[169] Fig. 31(d) shows a schematic of the controller architecture used. The algorithm is interfaced with the device through a raspberry-pi control board. The fluorescence intensity response of the device serves as feedback to the algorithm, which then decides the next course of actuation for the device. Fig. 31(e) shows results from the device tracking a set sine wave. The control algorithm adjusts V_{K+} given as input to the device in order for the fluorescence intensity to follow the set trajectory. The black trace is the value set by the algorithm, and the red trace is the device's response to the set value.

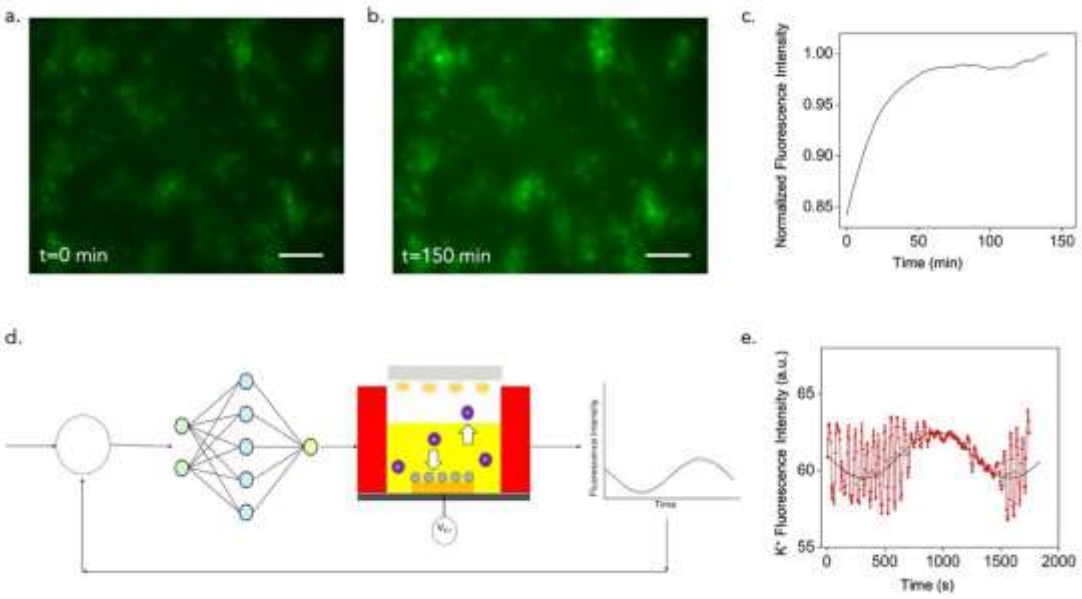

Figure 31: (a) Fluorescence microscope image of the cells over the device before actuation (t=0s). Scale bar 150µm. (b) Fluorescence microscope image of the cells over device after actuation (t=150 min). Scale bar 150µm. (c) Plot of change in

fluorescence intensity of the cells over time. (d) Schematic of closed-loop control integrated with the device. (e) Plot of device tracking a given sine wave using the control algorithm.

Although the ion pumps presented here were developed for delivering potassium, the same design can be utilized to deliver several other positively charged ions such as protons,[47] calcium,[171] and small molecules such as acetylcholine,[166] and GABA.[172] In order to deliver these species, the reservoir solution is switched out to a salt solution of the respective species and the delivery mechanism remains the same. This also increases the ease of multiplexing delivery by allowing us to deliver more than one type of species simultaneously.

3.1.3 CONCLUSIONS

In this work, we presented two designs of an ion pump capable of modulating potassium ion concentration in solution. The ion pumps showed here demonstrate the ease of integration with cells for in-vitro studies and can modulate potassium ion concentration with a high spatial resolution. As a proof-of-concept, we integrate the ion pump with THP-1 macrophage cell culture and observe the effects that changing extracellular potassium ion concentration causes on these cells. We also demonstrate a proof-of-concept implementation of a closed-loop control algorithm to drive the device towards the outcome we wish to achieve. The integration of closed-loop algorithms with the ion pump has great potential to be applied to the cells to study the effect of the

potassium ion on them and enable long-term biological control of membrane voltage with high spatial resolution.

3.1.4 METHODS

Device Fabrication

Well-plate device (PDMS-based design): We designed and printed PDMS molds using Preform software and Form3 3D printers. The molds have two layers, the bottom layer defining the reservoirs and the top layer defining the lid to seal these reservoirs. Once the PDMS is demolded, Ag and AgCl wires are inserted into the reservoirs to create the electrodes.

We then bonded the two layers of PDMS; the contact interfaces were treated in 50 W oxygen plasma for 10 seconds and clamped together using custom-made aluminum clamps. After bonding, a 1.5 μm thick water-insulating layer of Parylene-C was deposited (Specialty Coating Systems Lab Coater) in the presence of an A174 adhesion promoter. This layer also prevents bubbles from being formed in the reservoir. We then inserted four 3 mm long hydrogel-filled capillaries through the PDMS, and the reservoirs were filled with 1M KCl solution using a syringe. The PCB board is soldered onto the PDMS device. Silver conductive paste and alloy dowel pins connect the PCB to the electrodes before soldering to complete the connections.

The device is sealed into a custom-made 3D printed adapter, specifically designed to anchor the device in 6-well cell culture plates, and a layer of uncured PDMS is applied

at the interface and left to cure for 48 hours at room temperature to form a water-tight seal. (Fig 32)

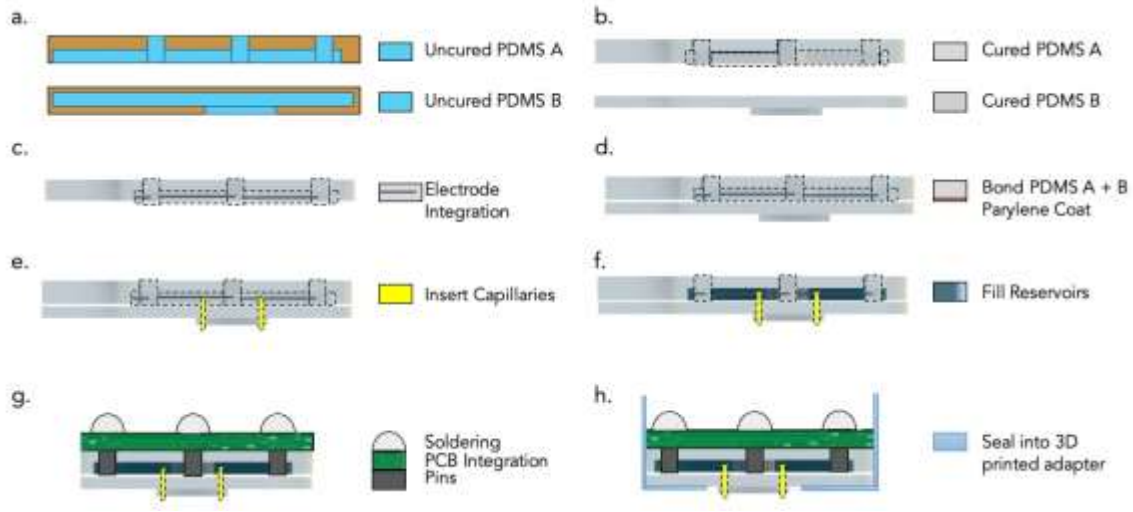

Figure 32: Fabrication Schematic for Well-plate device (PDMS- based design)

High Spatial Resolution Device (SU-8-based design): The ion pumps offering spatial resolution are fabricated on a glass substrate using photolithography techniques. Gold electrodes are patterned onto the substrate using S1813 photoresist followed by e-beam evaporation and liftoff process using Acetone/IPA. The surface of the electrodes is modified by electrochemically depositing Ag/AgCl nanoparticles on the surface of the electrodes. A 2 µm thick SU-8 2002 layer is spin-coated on to the device, which acts as an insulating layer following which a 40 µm thick SU-8 3050 layer is spun and patterned to create microfluidic channels on the substrate.

On a second glass wafer, we spin coat a layer of OmniCoat (Kayaku Advanced Materials Inc.) as a sacrificial layer. A 40 µm thick layer of SU-8 3050 is now spun

and patterned to form the features that act as a cap to the microfluidic channels previously patterned. The two glass substrates are now aligned and bonded using a wafer bonder and ramp baked together. The SU-8 layers fuse and bond, thereby creating closed microfluidic channels. Once the bonding is complete, the wafers are sonicated in a bath containing MF319 to dissolve the sacrificial OmniCoat, releasing the two wafers.

Stereolithography techniques are used to create PDMS fluidics that forms the ports for the SU-8 microfluidic channels. FormLabs 3D printers are used to print out molds that are then filled with PDMS (10:1 w/w base: curing agent) and left to cure at 60 °C for 48 hours. The PDMS is then demolded and thoroughly cleaned by sonicating in IPA and drying with N_2. This PDMS is then chemically bonded onto the SU-8 layer using a 20% v/v solution of (3-Aminopropyl) triethoxysilane (APTES) (Sigma-Aldrich, Burlington, Massachusetts US) in water. The PDMS and SU-8 surface to be bonded is treated with 50 W O_2 plasma in a reactive ion etcher for 30 seconds, then soaked in the APTES solution for 20 minutes. The surfaces are then rinsed with DI water and dried using N_2. The two surfaces are aligned, brought in contact, clamped using custom-made aluminum clamps, and baked at 110 °C for 30 minutes. The clamps are then left to cool to room temperature, and the device is removed from them.

Fig.33 shows the detailed fabrication schematic for these devices.

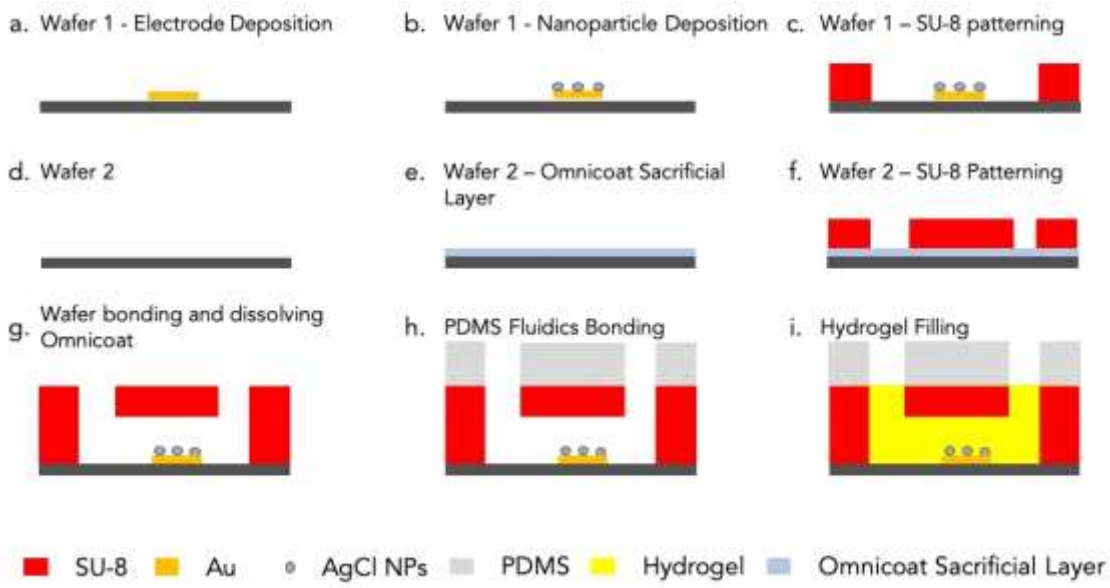

Figure 33: Fabrication schematic for high spatial resolution device (SU8-based design)

Figure 34 Zoom-in image of the 3 X 3-pixel array. Each pixel is a 100 μm in diameter and the pixels are set 250 μm apart from each other.

Hydrogel

a. Precursor Solution: We used an anionic hydrogel consisting made of 2-Acrylamido-2-methylpropane sulfonic acid (AMPSA) - Poly (ethylene glycol) diacrylate (PEGDA). This solution consists of the acrylate monomer mixed with PEGDA and a photo initiator (2-Hydroxy-4'-(2-hydroxyethoxy)-2-methylpropiophenone) which promotes crosslinking in the presence of UV light. The protocols for making the solution have been previously reported. [94] All chemicals were purchased from Sigma-Aldrich.

b. Capillary Preparation (For PDMS Based Well Plate Device): Glass capillaries are etched with 1M NaOH solution followed by flushing with DI water. Silane A-174(3-(trimethoxysilyl)propyl methacrylate) (2530-85-0, Sigma-Aldrich, Burlington, Massachusetts, US) in toluene is used to treat the capillaries for 1 hour after which they are rinsed with ethanol. The hydrogel precursor is now flown into the capillaries and crosslinked under UV at 8 mW/cm^2 (wavelength 306 nm) for 5 minutes.

c. Hydrogel in SU-8 channels (For SU-8 Based High Spatial Resolution Device): Before filling, the device is treated using silane A-174 to promote adhesion between the hydrogel and the SU-8 walls of the channels. To do the silane treatment, the SU-8 is first treated with O_2 plasma for 10 minutes, following which it is placed in a chamber at 90 °C where A-174 is deposited via chemical vapor deposition. The silane is baked onto the inner walls of the channels on a hotplate at 110 °C for 10 minutes.

After the silane has been deposited, the hydrogel precursor solution is flown into the channels and crosslinked under UV at 8 mW/cm^2 (wavelength 306 nm) for 5 minutes.

Cell Culture

THP-1 macrophages (TIB-202™; ATCC, Manassas, Virginia USA) were grown in RPMI 1640 medium (30-2001™; ATCC, Manassas, Virginia USA) supplemented with 10% fetal bovine serum (Corning™ 35011CV; Fisher Scientific, Cambridge, Massachusetts USA), 100 µg/mL Penicillin-Streptomycin (Gibco™ 15140122; Fisher Scientific, Cambridge, Massachusetts USA). Liquid nitrogen cryopreserved stocks (passage four) were seeded into the above complete media at an initial seeding density of 200,000 cells/mL. After four days, cells were counted using a hemocytometer and Trypan Blue solution (T8154; Sigma-Aldrich, Burlington, Massachusetts USA). Instead of media replacement, cells were either expanded or reduced to a resultant density of 200,000 cells/mL every 48 hours. After one week post-resuspension, cells were transferred to the PDMS cell culture cap [Fig. 34], and M_0 macrophages were generated by supplementing media with 100 ng/mL Phorbol-12-myristate-13-acetate (524400; Sigma-Aldrich, Burlington, Massachusetts USA) for 24 hours. Once M_0 macrophages were generated, complete media replacements were performed. For M_0 macrophages, subsequent media consisted of complete RPMI (described in detail above). For M_1 macrophage generation, complete RPMI media was supplemented with 100 ng/mL of lipopolysaccharide from Escherichia coli, Serotype O55:B5 (TLRGRADE®)(ALX-581-013-L001; Enzo Life Sciences, Farmingdale, New York USA) and 20 ng/mL Recombinant Human IFN-γ (300-02; PeproTech, Cranbury New Jersey USA) for 24 hours, then replaced with complete RPMI. For M_2 macrophage

generation, complete RPMI media was supplemented with 20 ng/mL of Recombinant Human Interleukin 4 (IL-4)(200-04; PeproTech, Cranbury New Jersey USA) and 20 ng/mL of Recombinant Human Interleukin 13 (IL-13) (200-13; PeproTech, Cranbury New Jersey USA) for 24 hours, then replaced with complete RPMI. After induction of polarization, all polarization states were maintained for 72 hours, then used in time-synchronized experiments. All cell culture and experimentation were performed at 37 °C in a humidified incubator maintained at 5% CO_2.

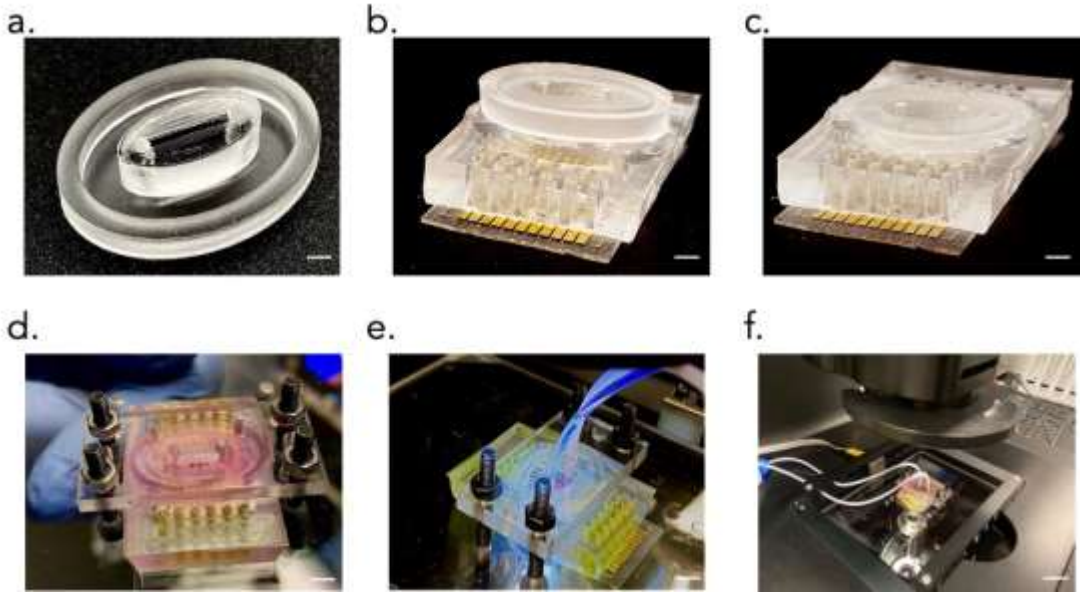

Figure 35: (a) PDMS cap serving as cell culture microfluidic chamber. Scale bar 2 mm. (b) PDMS cap inserts halfway into the SU-8 device. Scale bar 2 mm. (c) PDMS cap inserts all the way into the SU-8 device. Scale bar 2 mm. (d) SU-8 device and PDMS cap clamped together. The region in pink shows the cell culture chamber which serves as the target for the ion pump. The yellow regions show the reservoirs for the pump. Food color is used to mark these regions (for representative purposes. Scale bar

2 mm. (e) Setup connected to ElveFlow system for continuous cell media flow to the cell culture chamber. The tubes from the flow system are plugged into the PDMS cap. Scale bar 2 mm. (f) Device connected to flow system placed on an on-stage incubator under a microscope enabling real-time monitoring of the system and long-term in vitro studies. Scale bar 10 mm.

Control Board

The control board is a 16-channel potentiostat interfaced to a Raspberry Pi single board computer, based on the design demonstrated by Pansodtee et al.[173] Each channel can provide an actuation voltage of ±4 V and an output current of ±20 μA. Using an instrumental amplifier, the controller measures real-time current by first measuring the voltage across a high-precision (0.1%) 1 kΩ shunt resistor. The onboard ADS1115 analog-to-digital converters (ADCs) then measure the amplifiers' output voltages and determine the currents. The actuation voltages are set using the onboard MCP4728 digital-to-analog converters (DACs). The I2C communication bus of the Raspberry Pi is utilized to send commands to the DACs and retrieve data from the ADCs. A Python program running on the Raspberry Pi listens for commands from a client and changes the actuation voltages and measures currents. The Raspberry Pi is put into soft Access Point (AP) mode so that a laptop running the close-loop control program can connect to it via Wi-Fi and provide the necessary course of action based on the current readings.

Fluorescence Probes

We used microscope-based real-time imaging to monitor the change in ion concentration. The fluorescent probe ION Potassium Green-2 (IPG-2) TMA+ salt (3013F, ION biosciences, Texas) is a yellow-green fluorescent, intracellular potassium ion indicator with $\lambda_{excitation}/\lambda_{emission}$ of 525 nm/545 nm respectively and has high sensitivity to detect small changes in K^+ concentration. It exhibits a linear relationship between fluorescence intensity and K^+ concentration. The dye was made to 3μM dispensed in 0.1M Tris buffer. All fluorescence images were analyzed using ImageJ software.

To observe the changes in cell membrane voltage, we used $DiBAC_4(3)$ (Bis-(1,3-Dibutylbarbituric Acid) Trimethine Oxonol) (B438; ThermoFisher, Waltham, Massachusetts, USA). This dye is a slow-response potential-sensitive probe that enters depolarized cells where it binds to intracellular proteins and/or the cell membrane; increased depolarization results in an increase in fluorescence intensity, whereas hyperpolarization is indicated by a decrease in fluorescence intensity at an $\lambda_{excitation}/\lambda_{emission}$ of 493/516 nm respectively. Staining of cells was performed by exposing cells for 30 minutes to complete (defined above) phenol-red-free formula of RPMI (11835030; ThermoFisher, Waltham, Massachusetts, USA), containing a 10 μM solution of the dye, followed by imaging (note: the dye was left in the media during image acquisition). All cell images were analyzed using ImageJ software.

Reproduced from [48]

3.2 DELIVERY OF Na^{+} AND Ca^{+2}

3.2.1 BIOELECTRONIC DELIVERY OF SODIUM

Voltage-gated sodium channels play an important role in the initiation and propagation of action potentials in neurons. [174] Depolarization of the cell membrane causes the sodium channels to activate and inactivate within milliseconds. The influx of sodium ions through these sodium channels depolarizes the membrane further and initiates the rising phase of the action potential. [175] Thus bioelectronic delivery of sodium is of great interest in studying action potentials and innervation.

The SU-8-based ion pumps described in the previous section were used to demonstrate bioelectronic delivery of Na+. Fluorescent dye, CoroNa Green, was used to visualize and calibration change in [Na+] in response to actuation voltage, $V_{Na+.}$ Figure 36(a) shows a schematic of the sodium pump. CoroNa Green shows an increase in fluorescence intensity with an increase in [Na+]. Figure 36(b) shows fluorescence microscope readings demonstrating a change in intensity with a change in [Na+].

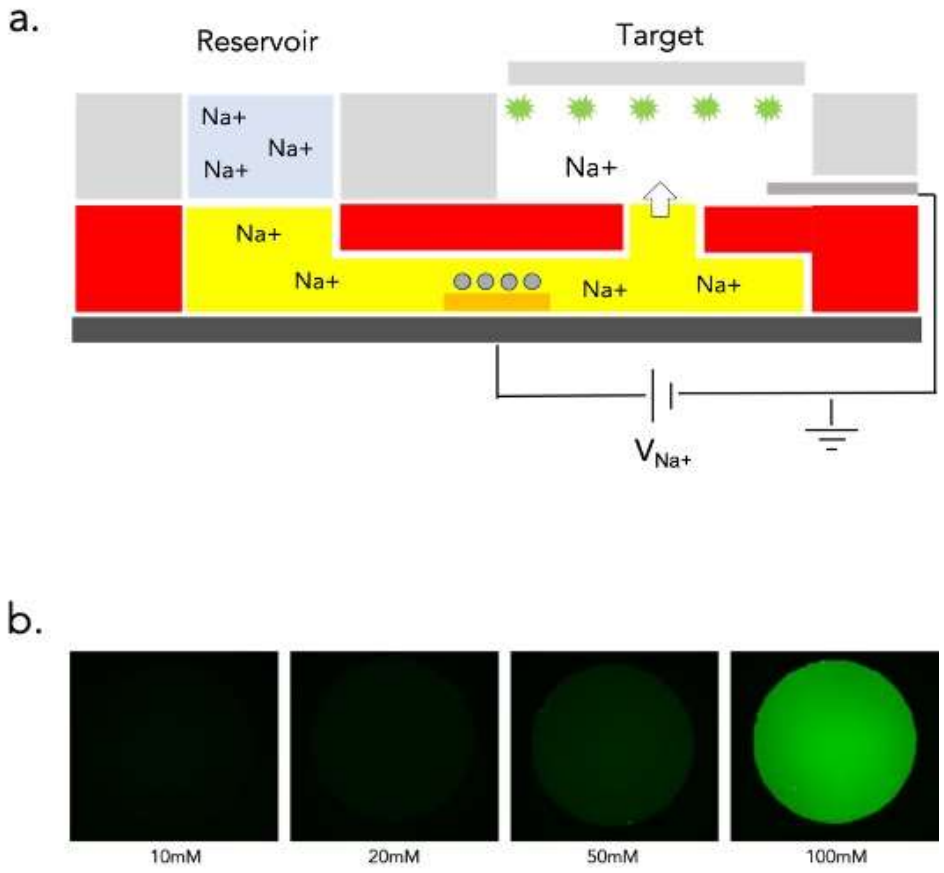

Figure 36 (a) Schematic of sodium pump (b) Fluorescence response of CoroNa Green with varying [Na+]

The fluorescent dye was calibrated using the standard equation below to correlate fluorescence intensity and concentration of sodium delivered.

$$[Na^+] = K_d \frac{F - F_{min}}{F_{max} - F}$$

Where K_d – dissociation constant

F, F_{min}, F_{max} – fluorescence intensities

For a positive V_{Na+}, Na+ is delivered to the target, thus increasing the sodium concentration of the target. Monitoring the fluorescence of the target shows that the

change in concentration closely follows the voltage applied. To evaluate the spatiotemporal resolution of the delivery, V_{Na+} of 1V was applied for 100ms. The current response sharply followed the voltage and generated a square wave that acutely followed the 100ms voltage pulse. COMSOL Multiphysics simulations showed that [Na+] is the greatest just above the pixel array where delivery occurs and gradually decreases as we go away and higher from the pore. This is due to the fact that diffusion is present and the concentration diffuses away over time.

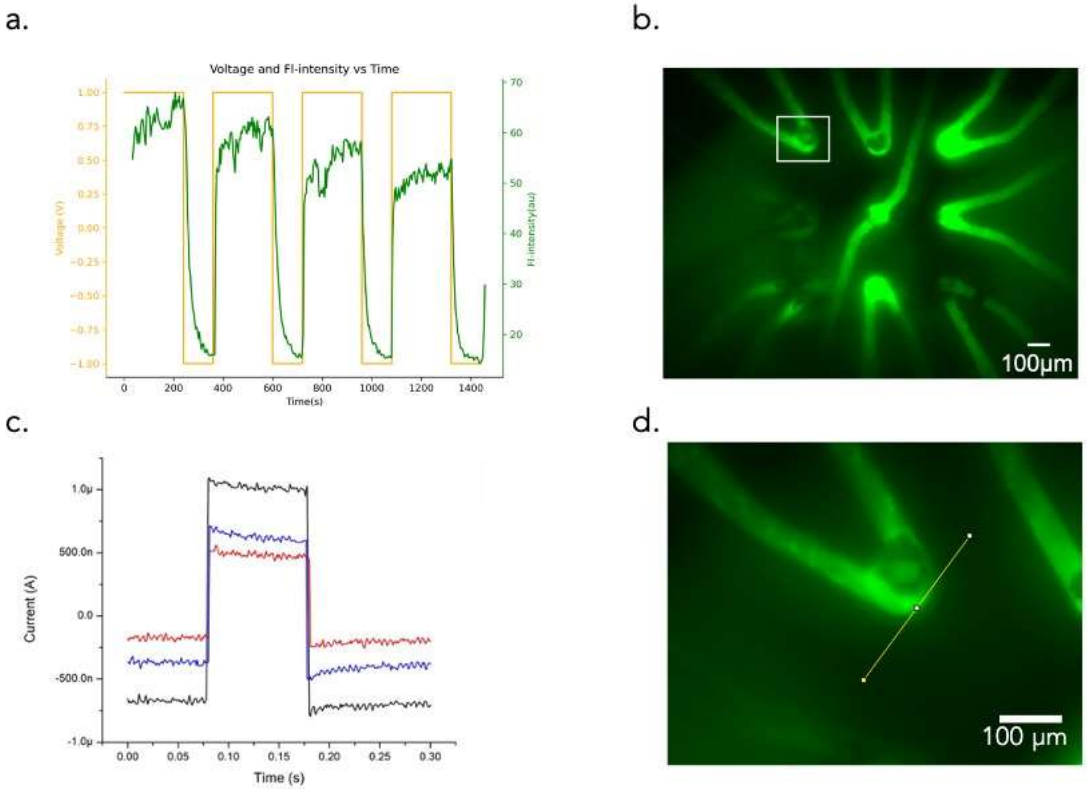

Figure 37: (a) Fluorescence response of sodium pump (b)Microscope image of the pixel array. Fluorescence intensity was measured from the region highlighted in the white box (c) Current response of sodium pump to a 100ms square wave pulse indicating temporal resolution (d) Spatial resolution of sodium pump

3.2.2 BIOELECTRONIC DELIVERY OF CALCIUM

Ca^{2+} is a ubiquitous intracellular messenger that controls diverse cellular functions. [176] Ca^{+2} channels play an important role in transforming naïve macrophages into M1 or M2 macrophages that regulate inflammatory response. [177]

The SU-8-based ion pump described in the previous section was modified by changing the reservoir to 1M $CaCl_2$ to deliver Ca^{+2} to the target (Figure 38).

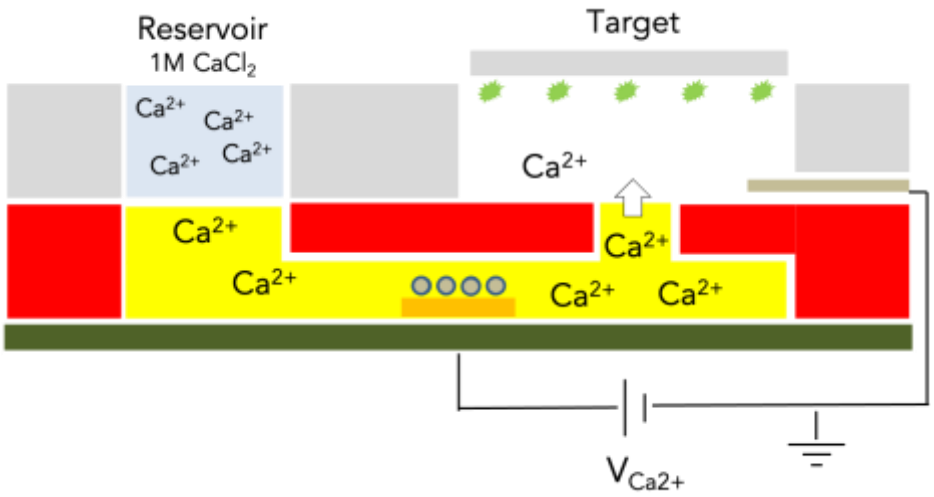

Figure 38: Schematic of the calcium pump

Fluorescent dye, Calbryte-520 Potassium salt, was used in order to visualize change in $[Ca^{+2}]$ in response to actuation. This observed $[Ca^{+2}]$ change was used to calculate the Ca^{+2} pumping efficiency of the device. The fluorescent dye was calibrated using the standard equation mentioned below to correlate fluorescence intensity and concentration of calcium delivered.

$$[Ca^{+2}]_{free} = K_d \frac{F - F_{min}}{F_{max} - F}$$

Where K_d is the dissociation constant of the probe

F, F_{min} and F_{max} are fluorescence intensities at various [Ca^{+2}]

The fluorescence response of the target was recorded in response to an actuation voltage V_{Ca+2} and it was observed that the fluorescence intensity closely follows the voltage applied to the device. Applying a positive voltage releases Ca^{+2} ions into the system thereby increasing the fluorescence intensity of the dye and the inverse happens when a negative voltage is applied.

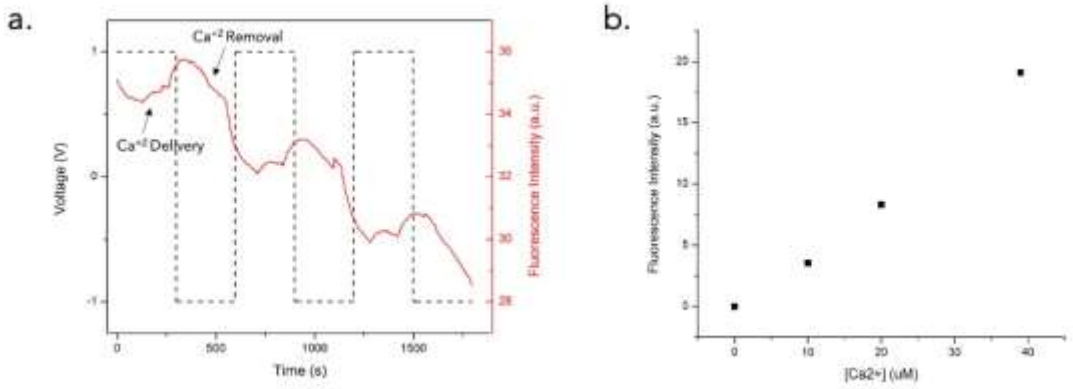

Figure 39 (a) Fluorescence response of the ion pump to V_{Ca+2}. (b) Calibration curve of Calbryte – 520. The fluorescence intensity of the dye increases with increase in [Ca^{+2}]

COMSOL Multiphysics was used to reinforce the results observed experimentally and to demonstrate spatiotemporal resolution of the calcium delivery. The concentration of calcium is highest directly above the delivery site and decreases as we go higher, and away from the region (Fig 40a). The concentration of calcium also increases as the delivery duration increases (Fig 40b)

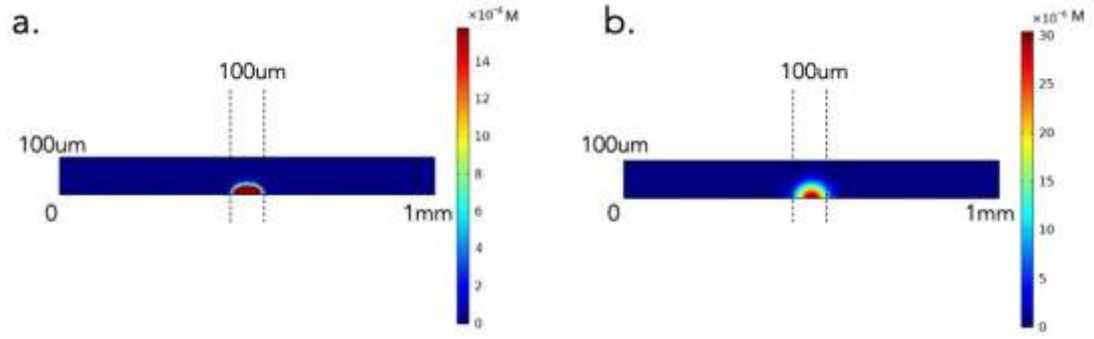

Figure 40: (a) COMSOL simulation showing [Ca^{+2}] after 100ms of delivery (b) COMSOL simulation showing [Ca^{+2}] after 300ms of delivery

3.3 BIOELECTRONIC DELIVERY OF FLUOXETINE – BIOCHEMICAL

3.3.1 INTRODUCTION

Recent developments in bioelectronics hold promise for advancing precision medicine.[178] Bioelectronic devices have been created that allow for monitoring blood sugar levels, controlling stem cell fate, applying electrical stimulation, and delivering therapeutic drugs.[36, 179, 180] Ion pumps are bioelectronic devices that allow for the movement of ions and charged drugs to move toward a targeted area electrophoretically.[45] They have applications in precision medicine when applying a concentration of a drug at a specific region and time is more effective than passive drug delivery methods such as digested pills.[181] Such applications require the ability to carefully control the delivery of therapeutics with precision. In[10], the authors discuss the ability of feedback control to enhance the capabilities of bioelectronic devices. However, implementing feedback control in bioelectronic devices presents unique challenges including variability in device performance. It is difficult to fabricate bioelectronics in a way that the end process is exactly the same. Due to variations

occurring in the fabrication process, the bioelectronic devices can differ in their properties. Components in the device can also vary in their performance when the device is used for an extended period of time.[93] This can lead to differing responses across devices and time when used in an experimental setting. To address the above-mentioned challenges, in previous work, a neural network (NN)-based machine learning algorithm was used with ion pumps to successfully control the pH level of a target solution.[39] A feedback control algorithm was able to regulate pH levels according to a target time-varying trajectory. In [39], the authors were able to use a similar control algorithm to control the membrane potential of stem cells by way of regulating pH of the extracellular environment. Thus, an adaptive feedback control algorithm helps to mitigate variations in system response even when they evolve in time. The second primary challenge in the control of bioelectronic devices is their limited operating range. That is, the voltages that can be applied to the device are limited. This causes a saturation issue that needs to be taken into account. In [182], the authors presented an alternative approach to arriving at an adaptive algorithm that has the benefits of the NN-based controller but explicitly handles saturation with guaranteed convergence. This algorithm was tested in silico.

In this paper, we present an adaptation of the algorithm presented in [182] to control the amount of biochemical being delivered by an ion pump. In our adaptation, we apply a heuristic switching algorithm for modification of the controller gains to improve performance. The biochemical chosen is fluoxetine, which has been shown to be a relevant drug in wound healing in diabetic mice.[183] We demonstrate the algorithm

with three different reference signals that result in the delivery of the same total drug concentration over the period of actuation. This was done to show the controller's ability to keep the current at the reference regardless of the signal used as well as to allow for different methods of delivery. We demonstrate that the controller is able to perform at a reasonable level, keeping the current near the reference throughout the experiment.

3.3.2 MATERIALS AND METHODS

Bioelectronic Ion Pump

Ion pumps are bioelectronic devices that can perform precise electrophoretic delivery of ions and molecules from a region of high concentration in the device, known as the reservoir, to the region of interest, known as the target.[45, 166] Over the years, ion pumps have been used to modulate pH in a local environment, [184] treat neurological disorders, [185, 186] induce macrophage recruitment, [48] and even to deliver biochemicals in plants. [106] In this work, we use the ion pump to deliver Fluoxetine, a biochemical which is a selective serotonin reuptake inhibitor known to have immunomodulatory effects. [183] The ion pump transfers the biochemical from the reservoir to the target, with a voltage (V_{pump}, typically between 0.5V and 2V) applied between the working electrode (Ag) and the reference electrode (Ag/AgCl) (Fig 41(a)). A negatively charged hydrogel selectively transports the biochemical between the target and the reservoir. In the reservoir, we have 0.01M of fluoxetine hydrochloride. Fluoxetine exists as a positively charged species at a pH of 5. For a positive V_{pump}, the Fluoxetine moves through the hydrogel-filled capillary and is transported to the target. Fig 41(b) shows an image of

the device in a six-well plate with a buffer solution. This acts as our target for the experiments.

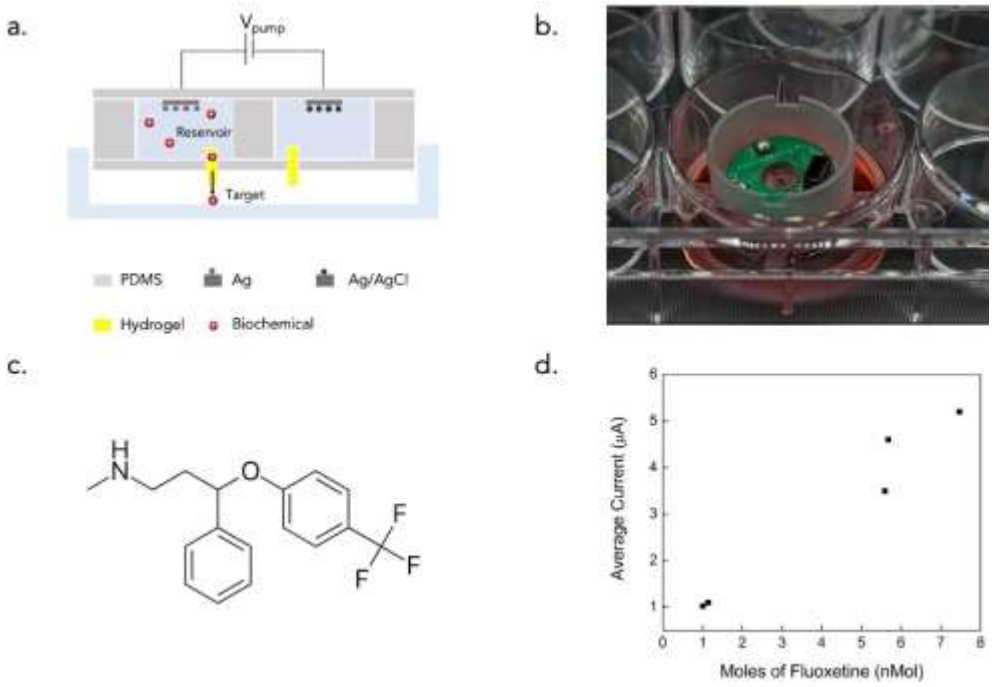

Figure 41: (a) Schematic of the bioelectronic ion pump. (b) Image of the ion pump in a 6-well plate with buffer solution. (c) Chemical structure of Fluoxetine (d) Graph showing the relationship between the current produced by the ion pump and the amount of fluoxetine delivered.

We collect the target solution after completion of delivery and use High-Performance Liquid Chromatography (HPLC) to estimate the amount of Fluoxetine in the target. We establish a relationship between the current produced during the biochemical delivery and the corresponding amount of fluoxetine delivered to calibrate the ion pump's performance (see Fig 41(d)) Based on these results, we found the devices to be

delivering the biochemical with an efficiency of approximately 20%, where efficiency is defined as follows.

$$Efficiency = \frac{No.of\ moles\ of\ FLuoxetine\ delivered}{No.of\ moles\ of\ electrons\ transferred}\ \text{X}\ 100\%$$

Controller

Sliding mode control is known for its ability to handle system uncertainties including unmodelled dynamics. [187] A sliding mode controller attempts to achieve a reference signal by forcing the system to slide toward a stable manifold. The controller drives the system towards a designed sliding manifold, where the system stays, sliding along the manifold until it reaches equilibrium. One major drawback with the control design is the chattering of the control signal that tends to appear. [188] However, researchers have developed many methods to address this so the control method can be used in real-world applications. It is applied in robotics, process control, induction motors, and power converters. [189-191] A similar sliding mode controller developed in [182] is utilized for the output feedback control experiment in this paper. The controller developed in [182] was shown to perform well with a mechanistic model of an ion pump that included saturation. The challenges encountered in simulations are comparable to the ones expected in these experiments. This inspired confidence that the controller developed in [182] would be a viable controller.

To begin, we consider our system to be an affine nonlinear system with input saturation represented by the following state space model

$$x' = f(x) + g(x)\emptyset(u) + \delta(t)$$

$$u' = v$$

$$y = h(x)$$

where x ∈ Rn is the state vector. In our experiment, x is the current being read from the system. An artificial control signal ν ∈ Rm is introduced to help reduce the known chattering issue with sliding mode controllers. The output of the function sat(ϕ(u)) ∈ Rm is the control input vector. In this application, this is the voltage applied to the system. The variable y ∈ Rn is the output vector of the system. In the experiment here y = x which is the read current from the system. The function f (x) ∈ Rn is an unknown locally Lipschitz nonlinear function and g(x) ∈ Rn×m is an unknown input coefficient value. The time-varying variable δ(t) ∈ R is a sufficiently smooth disturbance occurring throughout the experiment. We design the manifold as

$$s = Ke + e'$$

where K is a positive constant, and e is the error defined as

$$e(t) = x(t) - r(t)$$

x(t) is the current value, and r(t) is the desired reference value for the current.

The sliding mode controller then calculates the artificial control input to be used for calculating the actual control signal to be sent to the ion pump.

$$\nu = \mu\rho sign(Qs)$$

where ρ is a positive coefficient and Q is obtained as

$$Q = g(x)\nabla u\, \phi(u)$$

We require the sign of g(x) found through experiments to be μ = −1, which is the case when the response of the system is monotonically increasing with the input. In some

cases, the rate of change in the response could be faster or slower in one direction than the other.

For details regarding the stability proof of the developed controller, readers are referred to our previous work. [182]

Experimental Setup

The ion pump is integrated with a printed circuit board (PCB) interface which connects the electrodes in the pump to an external power supply. We use silver pins and a conductive silver paste to connect the Ag/AgCl electrodes in the reservoir to the PCB which is then soldered to the ion pump. Jumper cables are used to connect this PCB to a Raspberry Pi-based external voltage controller which can connect to the WiFi24. The device is seated in a six-well plate with a buffer solution acting as the target for delivery. The external voltage controller applies the control commands it receives from the sliding mode controller to the ion pump. The setup is able to successfully apply up to 16 different voltages with a resolution of 1.95mV per its channels. In addition, it is able to successfully read up to 16 current values from the ion pump but at a potential sacrifice in the accuracy of the reading, where the resolution of the current reading is 0.125nA. This could lead to extra uncertainty in the system. Figure 42 shows the closed-loop experimental setup. The error is calculated using the value of the current output read from the ion pump and the desired reference value. The sliding mode controller evaluates the next voltage value to drive the current toward the desired reference. This is sent to the Raspberry Pi through a WiFi connection between the Raspberry Pi and a laptop where the control algorithm is running. The Raspberry Pi

applies the voltage value to the ion pump through a connected cable. This closes the loop.

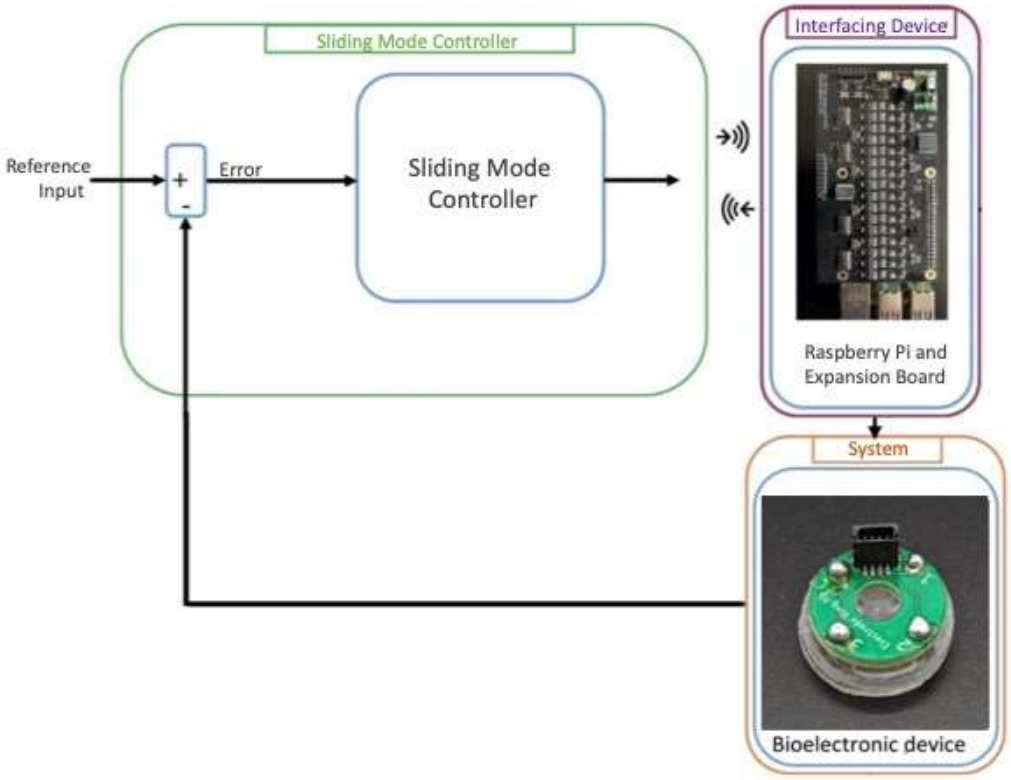

Figure 42: Schematic of the experimental closed-loop setup. The error is computed using the values of the current output read from the ion pump and the desired reference value. The sliding mode controller evaluates the next voltage value. This is sent to the external voltage controller with Raspberry Pi through a WiFi connection with the laptop running the control algorithm. The external voltage controller applies the value through a connected cable from the ion pump. After the voltage has been applied, the external voltage controller reads the current from the ion pump and sends it back to the laptop with the control algorithm through WiFi closing the loop.

3.3.3 RESULTS

Figure 42 shows experimental results for feedback control on current in the ion pump device using sliding mode control. In the first column, the blue lines indicate the desired current set as a reference for the feedback control algorithm. The red line is the current being measured from the device in real-time. The second column shows the controller output (i.e., voltage) being applied to the ion pump in green. The third column shows the corresponding tracking error in cyan.

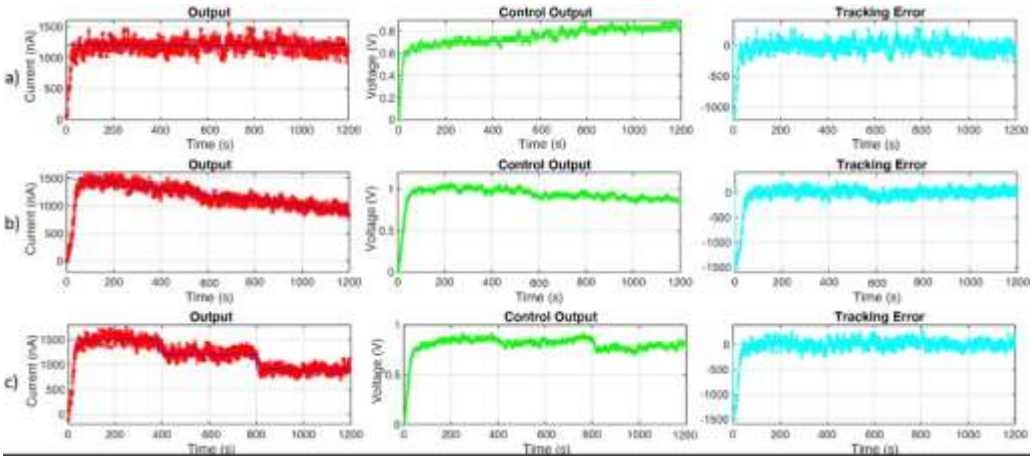

Figure 43: *Experimental results for feedback control on current in the ion pump device using sliding mode control. Row (a) shows the ion pump response to a constant reference signal at 1200nA. Row (c) shows the ion pump response to step changes in the reference signal starting at 1500nA dropping by 300nA each 400 seconds. Row (b) shows the ion pump response to a gradual decline reference signal beginning at 1500nA and ending at 900nA. The blue line in the first column indicates the desired current set as a reference for the feedback control algorithm. The red curve represents the measured current from the device in real time. The second column shows the control*

output that is delivered to the device in green. The third column shows the error between the desired and measured current referred to as tracking error in cyan.

We establish a value for the reference signal by estimating the amount of current required to deliver a dosage of 0.45mg of fluoxetine. Based on device calibration, we estimate that a current of 1.2μA (1200nA) is required to meet the desired dosage of biochemical. In the first experimental setup (see Fig 43(a)), we test the controller's performance on a constant reference signal of 1200nA. In the second experiment (see Fig 43(b)), we test the controller's performance on a gradual descending reference signal starting at 1500nA dropping to 900nA by the end of the experiment. In the third experiment (see Fig 43(c)), we test the controller's performance on a step-wise descending reference signal starting at 1500nA, dropping by 300nA every 400 seconds. Note that the fluctuations around the reference signals at steady-state have a relative error of less than 7% in all the experiments. We define the system to be at steady-state after the first 100 seconds of the experiment to allow for all three runs to reach the reference from the starting current of 0nA. Since the amount of biochemical delivered is determined by integrating over the measured current, we don't expect that the high-frequency fluctuations in current measurements have a high impact on the overall uncertainty in the biochemical delivery. Although the fluctuations make it difficult to keep the current exactly at the reference, the average current throughout each experiment can be calculated to show the desired amount of fluoxetine is being delivered. The average for each reference signal is as follows: constant - 1171.49nA,

gradual decline - 1166.45nA, decreasing steps - 1184.75nA. Table 1 shows the relative error information along with the averages.

Table 2: Quantitative measures of all the experiments.

Experiment	Average Output Signal	Average Steady-State Relative Error
Constant	1171.49nA	7%
Gradual Decline	1166.45nA	6%
Decreasing Steps	1184.75nA	7%

3.3.4 DISCUSSION

We see that the controller had to gradually increase the voltage applied to the ion pump in order for it to maintain the constant reference. This is due to the device's decaying performance as the experiment continues. This highlights the need for an adaptive control strategy and reinforces why open-loop control is unable to deliver a desired concentration with precision. One thing to notice is that the average current throughout the experiment was always lower than the actual reference. It's unclear why this is happening but it can be compensated for by increasing the reference signal slightly past the wanted reference to offset the consistent error being seen.

An enhancement that can be applied to achieve better control of the ion pump is to develop an algorithm that automatically tunes the control parameters. The reason for this is that the efficiency of the ion pump tends to decline over time. This would mean that the response of the device will change over the course of the experiment, which could affect the performance of the sliding mode controller. Adaptive parameters could

lead to better performance since they would adjust as needed to the varying response of the ion pump.

Some of the oscillatory behavior of the current could be due to the interfacing board used. When the controller sends a voltage value that is smaller than the resolution of 1.95mV then the board is unable to send the exact voltage value. This can cause slight oscillatory behavior with the current as small changes in voltage are able to cause large changes in the current as seen in Fig 43. Although exact control of the current at the reference is not achievable, we see in Table 2 that the average of the current is near the desired value and is within acceptable relative error bounds. Finally, the presented work combining closed-loop control and delivery of fluoxetine by ion pumps can have real-world applications in the field of wound healing. People can respond differently to the same applied medical treatment for reasons such as age, ethnicity, and genetics. [192] This makes it difficult for physicians to treat people optimally. Through precision medicine, custom treatment options can be created depending on an individual's needs. Closed-loop control allows for the customization of the treatment strategy by changing the strategy in real time as new information is gained. [193] This can be done by interfacing the feedback control regulated ion pump presented here with a higher-level control algorithm that provides the reference signal. [182] In this way, wound healing might be treated by sensing how well a wound is responding to a specific treatment and changing the dosage of biochemicals as needed in real-time.

3.3.5 CONCLUSION

We demonstrated a method for delivering a desired amount of biochemical using closed-loop control. By finding the efficiency of the ion pump in delivering fluoxetine, one can compute the amount of fluoxetine being delivered using the current of the device. A sliding mode controller was used in vitro to successfully keep the current at the desired reference which allowed the desired amount of fluoxetine to be delivered. Reproduced from [194]

4. ACTUATORS TO STUDY IONIC COMMUNICATION IN BACTERIA

4.1 INTRODUCTION

Endogenous electrical signaling that exists in cells, i.e., bioelectricity, is of great importance in understanding the behavior of cells and regulating it. [42, 195, 196] One of the most popular examples of communication through electrical signaling is the propagation of action potential in neurons.[197] Ion channel function in bacteria is a region of interest in many studies. Bacterial biofilms are organized communities with billions of densely packed cells. Within the biofilm, metabolic coordination between cells involves some form of electrochemical signaling. [44] These metabolic changes involved changes in the membrane potential of the individual cells. Membrane potential is the electrical potential difference across the cell membrane of the cell that balances the concentration gradient inside and outside the cell. Changes in the membrane potential involve the movement of charged species across the cell

membrane. Several studies have studied the role played by potassium in changing the membrane potential of *Bacillus Subtilis*, and its role in biofilm formation. [44, 198, 199] This work integrates a bioelectronic ion pump with the *B. subtilis* biofilms to study the effect of spatiotemporally changing potassium concentration around the biofilm.

4.2 RESULTS AND DISCUSSION

Bioelectronic ion pumps have demonstrated the capacity to deliver ions and charged molecules to an array of various *in vivo* and *in vitro* 2D models. [200, 201] In this work, we demonstrate another application for these ion pumps by using them to deliver K+ to bacterial biofilms and study the effect caused in the biofilm by the spatiotemporal delivery of K+.

Figure 44a shows a schematic of the ion pump. In the reservoir, KCl exists as K+ and Cl-. For a positive $V_{K+,}$ K+ ions are transported from the reservoir to the target, which is the biofilm, through an AMPSA: PEGDA cation-exchange hydrogel. The device consists of 4 chambers filled with 1M KCl and containing an 800 μm diameter glass capillary filled with hydrogel. The chambers contain Ag and AgCl wires which act as the working and reference/ counter electrodes respectively. The details of K+ delivery have been previously described in [48].

The target in this work is a biofilm-forming strain of *B. Subtilis* grown on an agar substrate (Fig 44b). These biofilms are typically formed under environmental stress conditions. [202, 203] Studies have demonstrated a change in membrane potential corresponding to a change in the extracellular potassium ion concentration of the biofilms [44] [204]. Oscillations in extracellular potassium levels were synchronized with

oscillations in membrane potential throughout the biofilm, while clamping the potassium flux resulted in a quenching of the membrane potential oscillations. Internally, *B.subtilis* has a [K+] of about 300 mM. In their resting state, the K+ ion channels in the cell membrane are closed. When the extracellular [K+] is about 150 mM, it results in an efflux of K+ resulting in depolarization in the bacteria. When the extracellular [K+] is 300 mM, i.e, matching the internal [K+], the formation of a potassium electrochemical gradient is prevented. This quenches oscillations in the membrane potential of the bacteria (Fig 44c). [44]

In order to study whether a localized change in potassium ion concentration would cause a response in the stimulated region of the biofilm, we developed a setup to integrate the ion pump into a 6-well plate using a custom-made 3D-printed adapter. The adapter stabilizes the ion pump in the well while simultaneously allowing us to image the biofilm through the device. This setup of the ion pump with the biofilm enables us to locally stimulate the biofilm with K+ delivery from the ion pump and monitor the biofilm's response over several hours. The platform also has the advantage over a traditional, microfluidics-based setup because the biofilm is composed of extremely motile cells, and having the agar substrate holds the biofilm together and prevents the cells from swimming away.

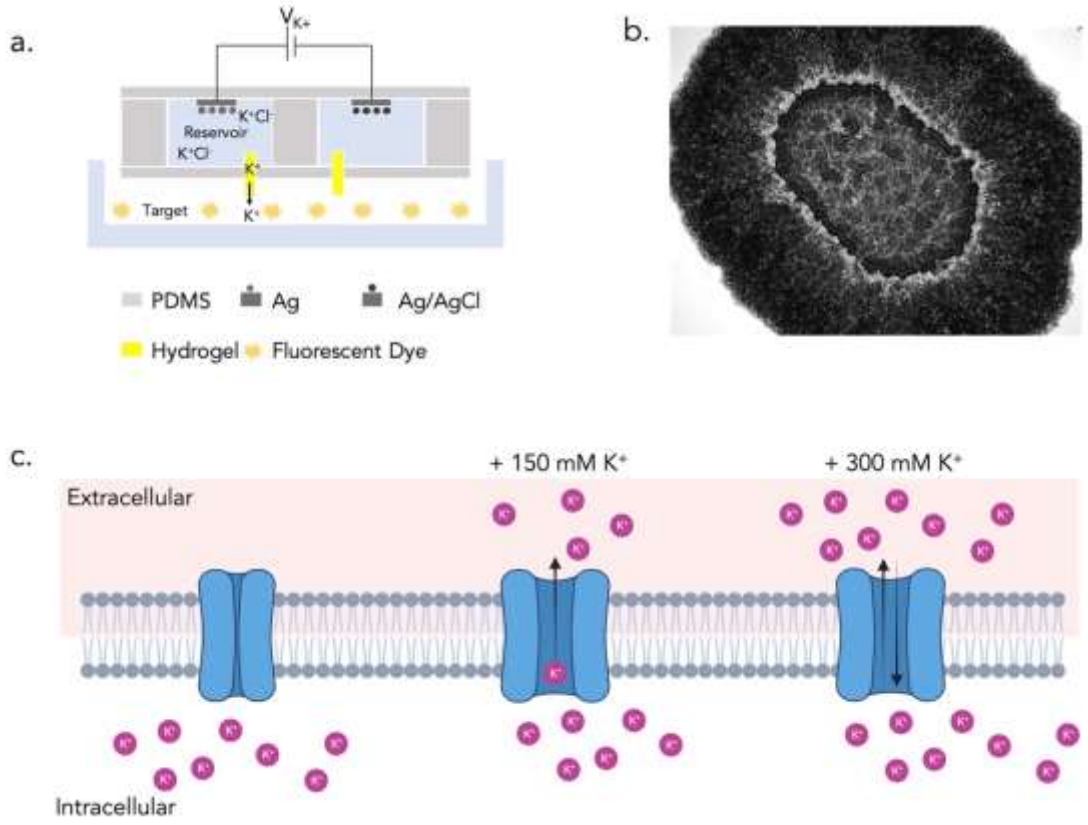

Figure 44: (a) Schematic of the potassium ion pump (b) Microscope image of B. Subtilis biofilm (c) Transport of K+ through the potassium ion channels of the bacterial cell membrane under different extracellular [K+]. Created with BioRender.com

A yellow-green, fluorescent potassium indicator, IPG-2, was used to detect and calibrate potassium delivery from the ion pump to the target. The dye has a linear relationship between potassium concentration and fluorescence intensity of the dye. This relationship is used to generate a calibration curve to determine the change in concentration of K+ in the target post-delivery. We used a series of alternating V_{K+} pulses of +2V and -2V to characterize the delivery efficiency of the device.

In order to achieve a higher delivery dosage, it is crucial to optimize the delivery parameters, such as the current produced and the duration of delivery. According to Ohm's Law, the current produced is primarily dictated by the voltage, V_{K+}, and the resistances in the circuit. Fig 45 shows a simplified circuit diagram of the ion pump schematic. The main resistances that contribute to the overall resistance of the ion pump include the resistance of the electrodes, electrolytes in the reservoir, and the ion exchange membrane. The effect of reservoir concentration and V_{K+} on delivery efficiency has previously been discussed in a study by Dechiraju et. al [48]. Here, we will discuss how to optimize the resistance of the electrodes and the ion exchange membrane to ensure that we can meet the required delivery dosage.

$$V = IR$$

$$R_{total} = R_{electrode} + R_{electrolyte} + R_{IEM}$$

Resistance depends on the resistivity (ρ), length (L), and cross-sectional area (A)

$$R = \rho\frac{L}{A}$$

For a given length and material of a conductor, increasing the cross-sectional area results in a reduction of the resistance.

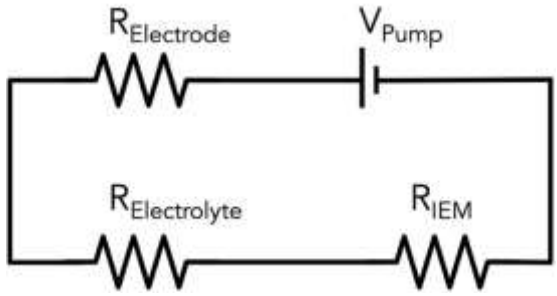

Figure 45: Circuit diagram of ion pump with the associated resistances

To reduce resistance associated with the electrodes ($R_{electrode}$), we increased the thickness of the wire used from 0.1 mm diameter to 0.25 mm diameter. To reduce the resistance associated with the hydrogel (R_{IEM}), we increased the thickness of the glass capillary from a 100 µm inner diameter to 800 µm inner diameter. The change in the current produced at each step is tracked and reported in table 3.

Table 3: Comparison of current for different electrode and IEM diameters

Diameter of electrode (mm)	Diameter of capillary (µm)	Current, I (µA)
0.1	100	2
0.1	400	12
0.1	800	20
0.25	800	80

We observe 40 times increase in the current produced when the electrode diameter is increased to 0.25 mm and the capillary diameter is increased to 800 µm.

Figure 46a shows a fluorescence microscope image of the biofilm with the device on top of it. The four large circles mark the locations where the capillaries meet the biofilm. The biofilm consists of two main parts – a central dormant region, and a peripheral region where the bacteria is active, and growth can be observed. To demonstrate the effect of locally delivering K+, the top right electrode was chosen as the WE while the top left electrode acts as the CE/RE since these electrodes are in

contact with the active region of the biofilm. Alternating pulses of V_{K+} = 2.5V and V_{K+} = 0V are used where actuation starts at t = 1hr and ends at t = 3hrs.

ThT (Thioflavin-T) dye is used to detect changes in the membrane potential of the biofilm. ThT is positively charged so it can be retained in cells due to the negative membrane potential inside the cell. ThT fluorescence increases when the inside of the cell becomes more negative, and thus ThT is inversely related to the membrane potential. For an extracellular potassium ion concentration of 150mM, the membrane potential of the biofilm decreases, resulting in an increase in the intensity of ThT.

We observe that during the course of actuation, the membrane potential of the stimulated region of the biofilm reduces, as indicated by the increase in the fluorescence intensity of the ThT (Fig 46b). This is consistent with the previously demonstrated behavior of the biofilms. An increase in [K+] near the WE also results in a slight reduction in [K+] at the CE since the CE reservoir draws Na+, K+, Ca+2, and other physiological cations because of the corresponding $-V_{K+}$ at that electrode. This results in an opposite behavior being observed at the biofilm around the CE as indicated in Fig 46b.

The change in membrane potential of the biofilm at the WE is also compared with the membrane potential of the dormant region of the biofilm over the course of actuation. The fluorescence intensity of ThT stays largely constant at the dormant region thereby showing that the increase in ThT signal is a result of K+ stimulation by the ion pump (Fig 46c). Finally, to demonstrate the spatial resolution of the device, a line is drawn between the WE and the CE/RE and the change in fluorescence intensity of the ThT

between t = 1 and 3 hours is plotted as a function of the distance from the CE. We can see that the intensity of change is strongest at the WE, and gradually decreases as we move away from the WE towards the CE/RE (Fig 46d). This demonstrates a strong effect of the spatial resolution of K+ delivery by the ion pump.

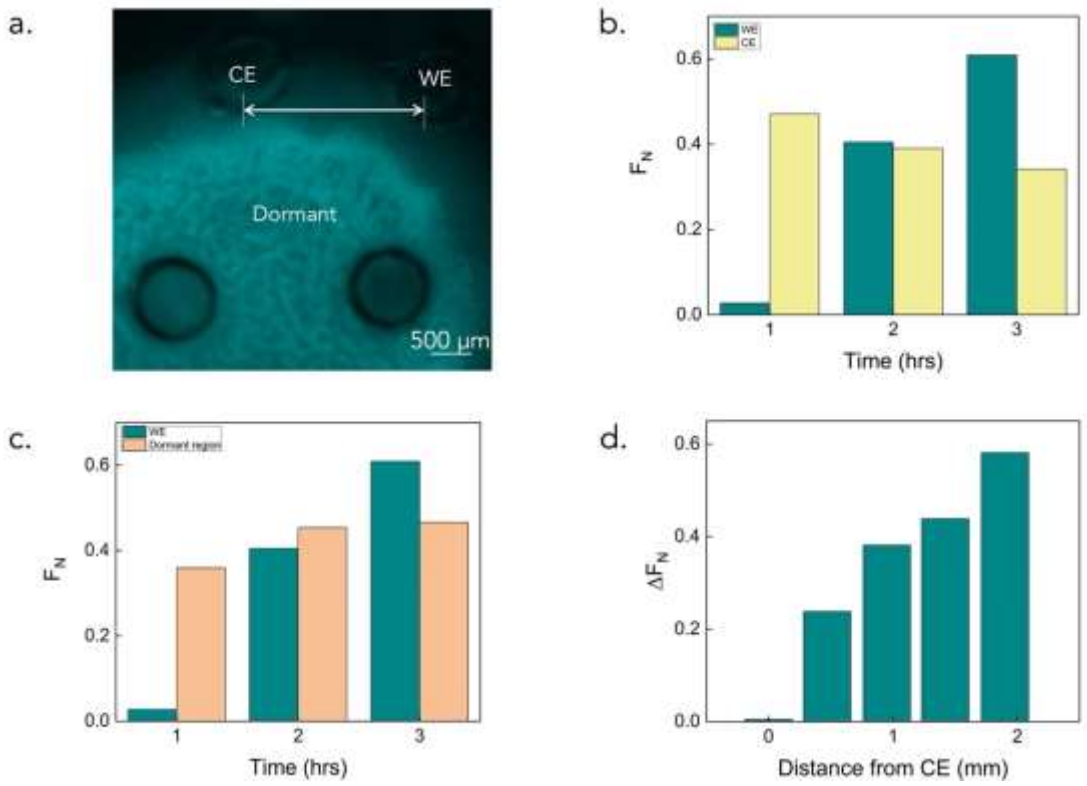

Figure 46: (a) Microscope image of the biofilm integrated with the ion pump. The positions of the WE, CE, and dormant regions are marked in the figure. Scale bar 500 um. (b) Comparison of ThT fluorescence at the WE and CE over the course of actuation. (c) Comparison of ThT fluorescence at the WE and the dormant region over the course of actuation (d) Change in ThT fluorescence as a function of distance from the CE measured over the duration of actuation.

Adding K+ to the extracellular environment also influences the growth of the biofilm. Studies show that potassium ion is involved in cell-to-cell signaling and metabolic coordination in the biofilm [204] [203]. In this study, we measured differences in the growth of biofilms that were treated and untreated with excess K+. The biofilms treated with K+ showed an increase in their growth compared to the untreated films when the external environmental conditions were maintained the same (Fig 47).

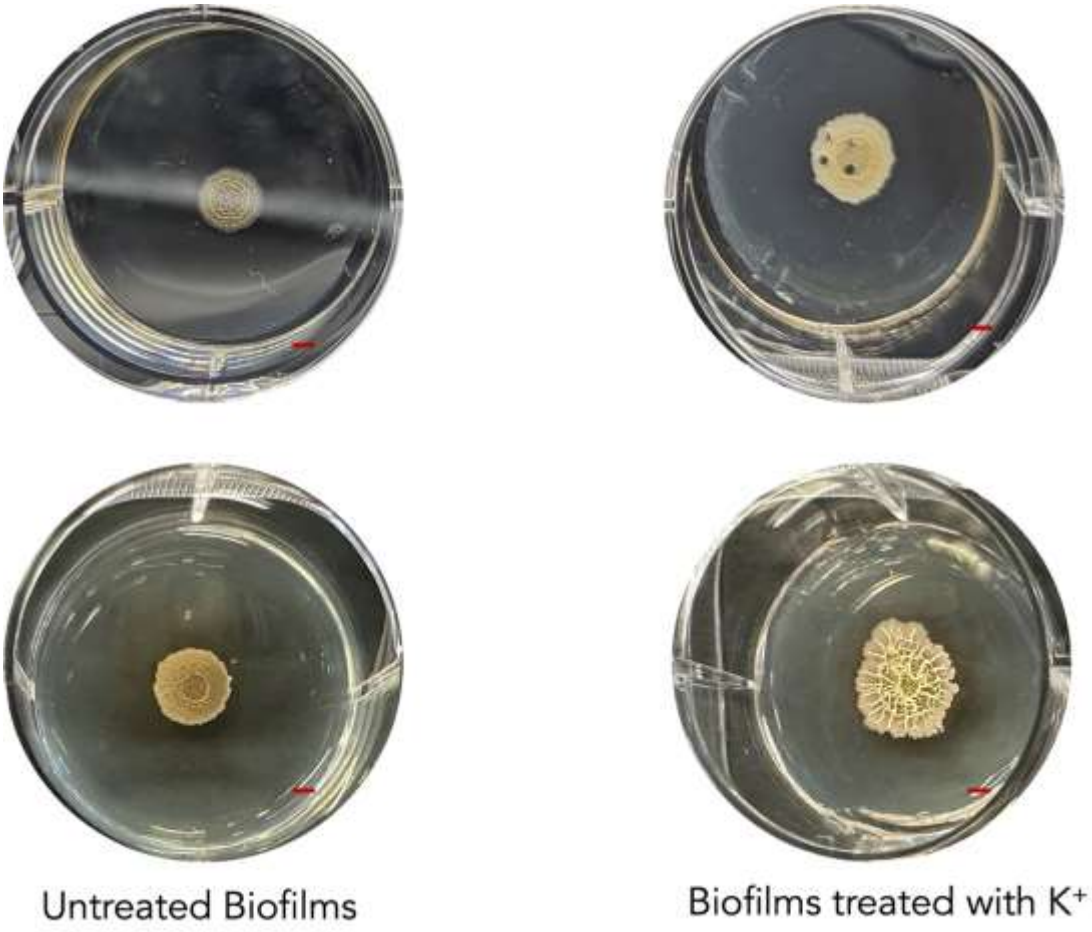

Figure 47: Growth of biofilm

4.3 CONCLUSION

In this work, we have successfully integrated a *B. Subtilis* biofilm with our ion pump setup in a 6-well plate. We utilize this setup to demonstrate the effect of changing the extracellular potassium ion concentration in very localized regions of the biofilm and observing the changes produced in the membrane potential and growth of the biofilm due to the stimulus. This work also has the potential to be expanded to study the effect of other ions and small molecules on biofilm growth and behavior and can be used as an alternative to microfluidic devices to study the effects of various electrical stimulation on communication and growth within these biofilm colonies.

4.4 METHODS

Device Fabrication

We designed and printed PDMS molds using Preform software and Form3 3D printers. The molds have two layers, the bottom layer defining the reservoirs and the top layer defining the lid to seal these reservoirs. Once the PDMS is de-molded, Ag and AgCl wires of diameter 0.25 mm are inserted into the reservoirs to create the electrodes. We then bonded the two layers of PDMS; the contact interfaces were treated in 50 W oxygen plasma for 30 seconds and clamped together using custom-made aluminum clamps. After bonding, a 1.5 μm thick water-insulating layer of Parylene-C was deposited (Specialty Coating Systems Lab Coater) in the presence of an A174 adhesion promoter. This layer also prevents bubbles from being formed in the reservoir. We then inserted four 5 mm long, 800 μm inner diameter glass capillaries filled with hydrogel through channels pre-made in the PDMS, and the reservoirs were filled with 1M KCl

solution using a syringe. The PCB board is soldered onto the PDMS device. Silver conductive paste and alloy dowel pins connect the PCB to the electrodes before soldering to complete the connections (Figure 48).

The device is sealed into a custom-made 3D printed adapter, specifically designed to anchor the device in 6-well cell culture plates, and a layer of uncured PDMS is applied at the interface and left to cure for 48 hours at room temperature to form a water-tight seal. We used an anionic hydrogel consisting of 2-Acrylamido-2-methylpropane sulfonic acid (AMPSA) - Poly (ethylene glycol) diacrylate (PEGDA). This solution consists of the acrylate monomer mixed with PEGDA and a photo initiator (2-Hydroxy-4'-(2-hydroxyethoxy)-2-methylpropiophenone) which promotes crosslinking in the presence of UV light. The protocols for making the solution have been previously reported. [94] All chemicals were purchased from Sigma-Aldrich.

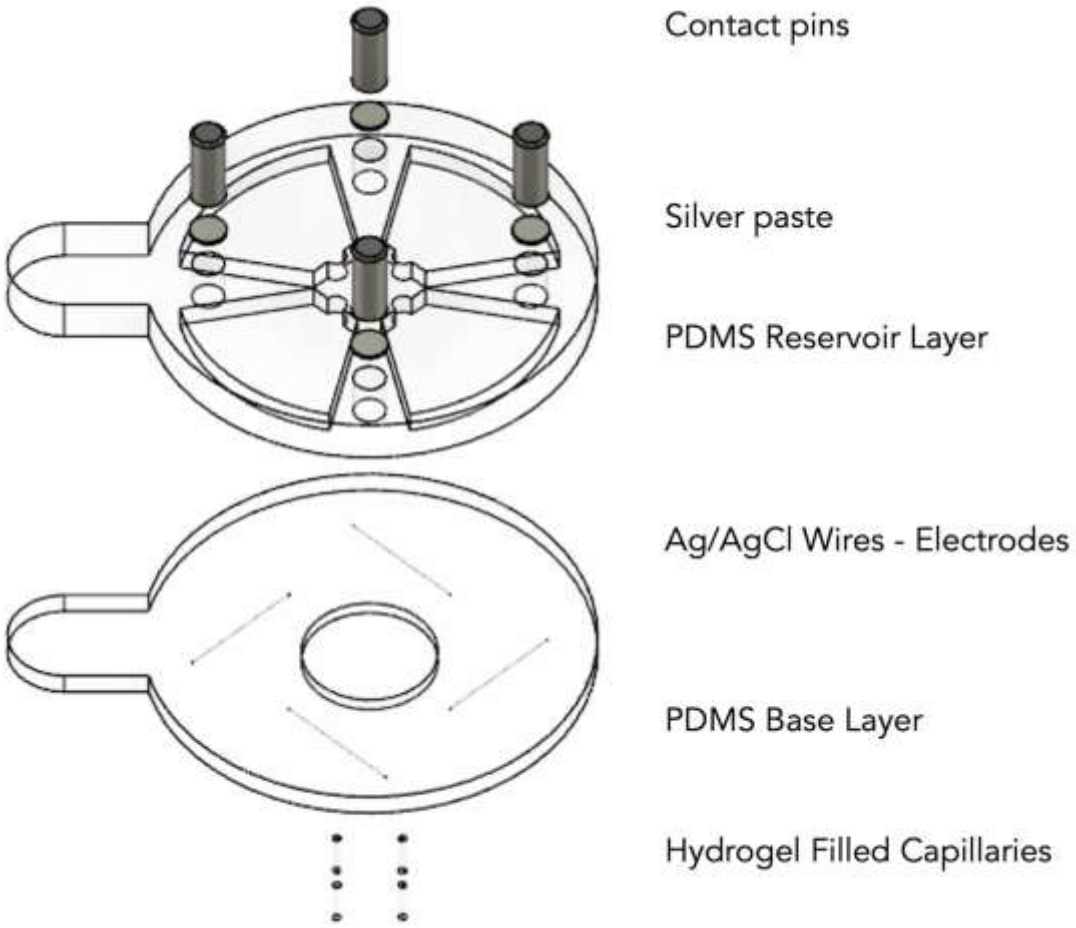

Figure 48: Fabrication schematic of the ion pump. Reproduced from [205]

Biofilm Formation

A biofilm-forming strain of *B. subtilis* was used. In brief, cells from a frozen stock were streaked on LB agar plates and incubated at 37°C overnight. Then, a single colony was picked from the plate and grown in liquid LB to the mid-exponential phase. A drop of cells was placed on 1.5% agar pads made with MSgg medium [5 mM potassium phosphate (pH 7.0), 100 mM 3-(N-morpholino) propane sulfonic acid (pH 7.0), 2 mM MgCl2, 700 mM CaCl2, 50 mM MnCl2, 100 mM FeCl3, 1 mM ZnCl2, 2 mM thiamine,

0.5% glycerol, 0.5% glutamate] and 10 μM Thioflavin T (ThT) in a 6-well plate. The plate was maintained at 30°C in a thermobox and cell growth was monitored using time-lapse fluorescence microscopy using an Olympus IX81 microscope and a 2.5x objective.

Fluorescence Probes

We used microscope-based real-time imaging to monitor the change in ion concentration. The fluorescent probe ION Potassium Green-2 (IPG-2) TMA+ salt (3013F, ION biosciences, Texas) is a yellow-green, fluorescent, intracellular potassium ion indicator with $\lambda_{excitation}/\lambda_{emission}$ of 525 nm/545 nm respectively and has high sensitivity to detect small changes in K^+ concentration. It exhibits a linear relationship between fluorescence intensity and K^+ concentration. The dye was made to 3μM dispensed in 0.1M Tris buffer. All fluorescence images were analyzed using ImageJ software.

To observe the changes in cell membrane voltage, we used the fluorescent, cationic dye Thioflavin-T (ThT). ThT has an $\lambda_{excitation}/\lambda_{emission}$ of 349 nm/454 nm. All cell images were analyzed using ImageJ software.

Time-Lapse Microscopy

Keyence BZ-X710 with a 2.5X objective was used for most of the experiments. Fluorescence images were taken with a YFP filter to characterize K+ delivery from the devices. Biofilm images were taken in phase contrast and CFP fluorescence. Images were taken every 10mins and the minimum exposure time to provide a good signal-to-noise ratio was used.

5. OUTLOOK

Bioelectronics has played an important role in clinical settings for decades with devices like the cardiac pacemaker and brain implants. Over recent years, bioelectronics has become an increasingly popular choice for point-of-care diagnostics and precision medicine applications. The developments in this dissertation contribute towards the effort to make platforms that can significantly reduce the need for animal studies while maintaining the same level of reliability. Devices integrated with on-chip microfluidics enable easy integration with 2D cell cultures and offer a high spatiotemporal resolution of ion and drug delivery to the cells while devices that can be used in standard 6-well plates offer increased ease of integration with more complex 3D cell models such as organoids as well as integration with cell types that exist in non-liquid mediums.

Organisms rely on a multiscale feedback control structure that enables hierarchical homeostasis of their physiological processes. While bioelectronic devices (sensors and actuators) offer the opportunity to interact with biological systems, the full potential of these interactions can be realized through sophisticated control algorithms. These algorithms need to be resilient to inherent challenges in biological systems, such as uncertainty, noise, and temporal and response variability. Closed-loop approaches can effectively address these limitations and enable precise control, even without extensive prior knowledge of the system, thanks to their real-time learning capabilities. In this context, the implementation of closed-loop control algorithms on bioelectronic ion pumps for long-term pH control, delivering various other ions such as potassium as

well as delivering precise doses of biochemicals such as fluoxetine allow for improved integration of bioelectronic devices with physiological control loops and facilitating the restoration of homeostasis. Considering that homeostasis is fundamental to life itself and that age-related changes often involve slower and weaker homeostasis control loops, the merging of such control algorithms with bioelectronic sensors and actuators holds significant promise for advancing the field of bioelectronic medicine.

6. BIBLIOGRAPHY

[1] E. M. Bick, Clin Orthop Relat Res 1972, 88, 2.

[2] M. Piccolino, Trends in Neurosciences 1997, 20, 443.

[3] M. Seitanidou, R. Blomgran, G. Pushpamithran, M. Berggren, D. T. Simon, Advanced Healthcare Materials 2019, 8, 1900813.

[4] A. Williamson, J. Rivnay, L. Kergoat, A. Jonsson, S. Inal, I. Uguz, M. Ferro, A. Ivanov, T. A. Sjöström, D. T. Simon, M. Berggren, G. G. Malliaras, C. Bernard, Advanced Materials 2015, 27, 3138.

[5] A. Zhang, C. M. Lieber, Chemical Reviews 2016, 116, 215.

[6] M. Berggren, A. Richter-Dahlfors, Advanced Materials 2007, 19, 3201.

[7] K. Sefah, J. A. Phillips, X. Xiong, L. Meng, D. Van Simaeys, H. Chen, J. Martin, W. Tan, Analyst 2009, 134, 1765.

[8] Y. Liu, J. Li, T. Tschirhart, J. L. Terrell, E. Kim, C. Y. Tsao, D. L. Kelly, W. E. Bentley, G. F. Payne, Advanced healthcare materials 2017, 6, 1700789.

[9] I. Y. Wong, B. D. Almquist, N. A. Melosh, Materials Today 2010, 13, 14.

[10] J. Selberg, M. Jafari, C. Bradley, M. Gomez, M. Rolandi, APL Materials 2020, 8, 120904.

[11] X. Strakosas, J. Selberg, Z. Hemmatian, M. Rolandi, Advanced Science 2017, 4.

[12] A. Obaid, M. E. Hanna, Y. W. Wu, M. Kollo, R. Racz, M. R. Angle, J. Muller, N. Brackbill, W. Wray, F. Franke, E. J. Chichilnisky, A. Hierlemann, J. B. Ding, A. T. Schaefer, N. A. Melosh, Sci Adv 2020, 6, eaay2789.

[13] S. Ronchi, M. Fiscella, C. Marchetti, V. Viswam, J. Muller, U. Frey, A. Hierlemann, Front Neurosci 2019, 13, 208.

[14] E. Song, C. H. Chiang, R. Li, X. Jin, J. Zhao, M. Hill, Y. Xia, L. Li, Y. Huang, S. M. Won, K. J. Yu, X. Sheng, H. Fang, M. A. Alam, Y. Huang, J. Viventi, J. K. Chang, J. A. Rogers, Proc Natl Acad Sci U S A 2019, 116, 15398.

[15] Y. Chen, Y. Zhang, Z. Liang, Y. Cao, Z. Han, X. Feng, npj Flexible Electronics 2020, 4.

[16] G. D. Spyropoulos, J. N. Gelinas, D. Khodagholy, Sci Adv 2019, 5, eaau7378.

[17] S. Inal, J. Rivnay, A. O. Suiu, G. G. Malliaras, I. McCulloch, Acc Chem Res 2018, 51, 1368.

[18] A. Zhang, C. M. Lieber, Chem Rev 2016, 116, 215.

[19] H. Fang, K. J. Yu, C. Gloschat, Z. Yang, C. H. Chiang, J. Zhao, S. M. Won, S. Xu, M. Trumpis, Y. Zhong, E. Song, S. W. Han, Y. Xue, D. Xu, G. Cauwenberghs, M. Kay, Y. Huang, J. Viventi, I. R. Efimov, J. A. Rogers, Nat Biomed Eng 2017, 1.

[20] E. Stavrinidou, R. Gabrielsson, E. Gomez, X. Crispin, O. Nilsson, D. T. Simon, M. Berggren, Sci Adv 2015, 1, e1501136.

[21] Z. Hemmatian, R. H. Tunuguntla, A. Noy, M. Rolandi, PLoS One 2019, 14, e0212197.

[22] A. M. Pappa, H. Y. Liu, W. Traberg-Christensen, Q. Thiburce, A. Savva, A. Pavia, A. Salleo, S. Daniel, R. M. Owens, ACS Nano 2020.

[23] M. Jakesova, M. Silvera Ejneby, V. Derek, T. Schmidt, M. Gryszel, J. Brask, R. Schindl, D. T. Simon, M. Berggren, F. Elinder, E. D. Glowacki, Sci Adv 2019, 5, eaav5265.

[24] A. Habib, X. Zhu, U. I. Can, M. L. McLanahan, P. Zorlutuna, A. A. Yanik, Sci Adv 2019, 5, eaav9786.

[25] A. Singer, S. Dutta, E. Lewis, Z. Chen, J. C. Chen, N. Verma, B. Avants, A. K. Feldman, J. O'Malley, M. Beierlein, C. Kemere, J. T. Robinson, Neuron 2020.

[26] L. Caruso, T. Wunderle, C. M. Lewis, J. Valadeiro, V. Trauchessec, J. Trejo Rosillo, J. P. Amaral, J. Ni, P. Jendritza, C. Fermon, S. Cardoso, P. P. Freitas, P. Fries, M. Pannetier-Lecoeur, Neuron 2017, 95, 1283.

[27] X. Strakosas, J. Selberg, P. Pansodtee, N. Yonas, P. Manapongpun, M. Teodorescu, M. Rolandi, Sci Rep 2019, 9, 10844.

[28] N. Bhokisham, E. VanArsdale, K. T. Stephens, P. Hauk, G. F. Payne, W. E. Bentley, Nat Commun 2020, 11, 2427.

[29] Y. Yu, H. Y. Y. Nyein, W. Gao, A. Javey, Adv Mater 2020, 32, e1902083.

[30] M. Jia, M. Jafari, P. Pansodtee, M. Teodorescu, M. Gomez, M. Rolandi, APL Materials 2022, 10, 041112.

[31] M. Jia, J. Kim, T. Nguyen, T. Duong, M. Rolandi, Biopolymers 2021, 112, e23433.

[32] J. Selberg, M. Jia, M. Rolandi, PloS one 2019, 14, e0202713.

[33] H. Chun, T. D. Chung, Annual Review of Analytical Chemistry 2015, 8, 441.

[34] S. Z. Bisri, S. Shimizu, M. Nakano, Y. Iwasa, Advanced Materials 2017, 29, 1607054.

[35] T. Arbring Sjöström, M. Berggren, E. O. Gabrielsson, P. Janson, D. J. Poxson, M. Seitanidou, D. T. Simon, Advanced Materials Technologies 2018, 3, 1700360.

[36] D. T. Simon, E. O. Gabrielsson, K. Tybrandt, M. Berggren, Chemical Reviews 2016, 116, 13009.

[37] D. J. Poxson, E. O. Gabrielsson, A. Bonisoli, U. Linderhed, T. Abrahamsson, I. Matthiesen, K. Tybrandt, M. Berggren, D. T. Simon, ACS Applied Materials & Interfaces 2019, 11, 14200.

[38] J. Isaksson, P. Kjall, D. Nilsson, N. D. Robinson, M. Berggren, A. Richter-Dahlfors, Nat Mater 2007, 6, 673.

[39] J. Selberg, M. Jafari, J. Mathews, M. Jia, P. Pansodtee, H. Dechiraju, C. Wu, S. Cordero, A. Flora, N. Yonas, Advanced Intelligent Systems 2020, 2, 2000140.

[40] A. G. Guex, D. J. Poxson, D. T. Simon, M. Berggren, G. Fortunato, R. M. Rossi, K. Maniura-Weber, M. Rottmar, Applied Materials Today 2021, 22, 100936.

[41] R. Binggeli, R. C. Weinstein, Journal of theoretical biology 1986, 123, 377.

[42] M. Levin, Pezzulo, G., and Finkelstein, J. M., Annual Review of Biomedical Engineering 2017, 19, 353.

[43] C. Li, M. Levin, D. L. Kaplan, Scientific Reports 2016, 6, 21044.

[44] A. Prindle, J. Liu, M. Asally, S. Ly, J. Garcia-Ojalvo, G. M. Süel, Nature 2015, 527, 59.

[45] A. Williamson, J. Rivnay, L. Kergoat, A. Jonsson, S. Inal, I. Uguz, M. Ferro, A. Ivanov, T. A. Sjostrom, D. T. Simon, M. Berggren, G. G. Malliaras, C. Bernard, Adv Mater 2015, 27, 3138.

[46] T. Nguyen, N. Asefifeyzabadi, H. Li, L. Luo, M. Rolandi, Advanced Materials Technologies 2023, 8.

[47] X. Strakosas, J. Selberg, X. Zhang, N. Christie, P.-H. Hsu, A. Almutairi, M. Rolandi, Adv Sci (Weinh) 2019, 6, 1800935.

[48] H. Dechiraju, J. Selberg, M. Jia, P. Pansodtee, H. Li, H.-C. Hsieh, C. Hernandez, N. Asefifeyzabadi, T. Nguyen, P. Baniya, G. Marquez, C. Rasmussen-Ivey, C. Bradley, M. Teodorescu, M. Gomez, M. Levin, M. Rolandi, AIP Advances 2022, 12.

[49] E. M. Ahmed, Journal of advanced research 2015, 6, 105.

[50] M. Jia, M. Rolandi, Advanced Healthcare Materials 2020, 9, 1901372.

[51] O. Wichterle, D. Lim, Nature 1960, 185, 117.

[52] S. Cascone, G. Lamberti, International Journal of Pharmaceutics 2020, 573, 118803.

[53] J. Li, D. J. Mooney, Nature Reviews Materials 2016, 1, 1.

[54] A. Gupta, M. Kowalczuk, W. Heaselgrave, S. T. Britland, C. Martin, I. Radecka, European Polymer Journal 2019, 111, 134.

[55] T. Distler, A. R. Boccaccini, Acta Biomaterialia 2020, 101, 1.

[56] N. Eslahi, M. Abdorahim, A. Simchi, Biomacromolecules 2016, 17, 3441.

[57] H. Yuk, B. Lu, X. Zhao, Chemical Society Reviews 2019, 48, 1642.

[58] D. Seliktar, Science 2012, 336, 1124.

[59] K. Y. Lee, D. J. Mooney, Chemical Reviews 2001, 101, 1869.

[60] C. Yang, Z. Suo, Nature Reviews Materials 2018, 3, 125.

[61] J. A. Tuszynski, in *Brain and Human Body Modeling: Computational Human Modeling at EMBC 2018*, (Eds: S. Makarov, M. Horner, G. Noetscher), Springer International Publishing, Cham 2019, 195.

[62] T. Someya, Z. Bao, G. G. Malliaras, Nature 2016, 540, 379.

[63] Q. Rong, W. Lei, M. Liu, Chemistry – A European Journal 2018, 24, 16930.

[64] J. Xu, Y.-L. Tsai, S.-h. Hsu, Molecules 2020, 25, 5296.

[65] K. B. Rufato, J. P. Galdino, K. S. Ody, A. G.B. Pereira, E. Corradini, A. F. Martins, A. T. Paulino, A. R. Fajardo, F. A. Aouada, F. A. La Porta, A. F. Rubira, E. C. Muniz, in *Hydrogels - Smart Materials for Biomedical Applications*, 2019.

[66] W. Hu, Z. Wang, Y. Xiao, S. Zhang, J. Wang, Biomaterials Science 2019, 7, 843.

[67] C.-J. Lee, H. Wu, Y. Hu, M. Young, H. Wang, D. Lynch, F. Xu, H. Cong, G. Cheng, ACS Applied Materials & Interfaces 2018, 10, 5845.

[68] E. Zygadło-Monikowska, Z. Florjańczyk, E. Wielgus-Barry, E. Hildebrand, Journal of Power Sources 2006, 159, 392.

[69] K.-T. Lee, N.-L. Wu, Journal of Power Sources 2008, 179, 430.

[70] Q. Tang, M. Chen, G. Wang, H. Bao, P. Saha, Journal of Power Sources 2015, 284, 400.

[71] A. Katzenberg, C. Muñoz Davila, B. Chen, T. Siboonruang, M. A. Modestino, ACS Applied Polymer Materials 2020, 2, 2046.

[72] Z. Shi, X. Gao, M. W. Ullah, S. Li, Q. Wang, G. Yang, Biomaterials 2016, 111, 40.

[73] H. Tan, K. G. Marra, Materials 2010, 3, 1746.

[74] J. L. Drury, D. J. Mooney, Biomaterials 2003, 24, 4337.

[75] P. G. Bruce, *Solid state electrochemistry*, Vol. 5, Cambridge university press, 1997.

[76] B. B. Owens, G. R. Argue, Science 1967, 157, 308.

[77] Y.-F. Y. Yao, J. Kummer, Journal of Inorganic and Nuclear Chemistry 1967, 29, 2453.

[78] K. A. Mauritz, R. B. Moore, Chemical reviews 2004, 104, 4535.

[79] B. D. Paulsen, K. Tybrandt, E. Stavrinidou, J. Rivnay, Nature materials 2020, 19, 13.

[80] M. Barrande, R. Bouchet, R. Denoyel, Analytical chemistry 2007, 79, 9115.

[81] W. Barros Jr, Physical Review E 2019, 99, 052501.

[82] J.-H. Cao, B.-K. Zhu, Y.-Y. Xu, Journal of membrane science 2006, 281, 446.

[83] T. M. W. J. Bandara, B. E. Mellander, in *Ionic Liquids: Theory, Properties, New Approaches*, 2011.

[84] F. H. Muhammad, R. H. Y. Subban, T. Winie, Materials Today: Proceedings 2017, 4, 5130.

[85] S. K. De, N. R. Aluru, B. Johnson, W. C. Crone, D. J. Beebe, J. Moore, Journal of Microelectromechanical Systems 2002, 11, 544.

[86] S. De, C. Cramer, M. Schönhoff, Macromolecules 2011, 44, 8936.

[87] P. Pissis, A. Kyritsis, Solid State Ionics 1997, 97, 105.

[88] Y. Guo, X. Zhou, Q. Tang, H. Bao, G. Wang, P. Saha, Journal of Materials Chemistry A 2016, 4, 8769.

[89] W. Hu, Z. Wang, Y. Xiao, S. Zhang, J. Wang, Biomater Sci 2019, 7, 843.

[90] G. Ruano, J. I. Iribarren, M. M. Pérez-Madrigal, J. Torras, C. Alemán, Polymers 2021, 13, 1337.

[91] N. Yan, D. R. Paul, B. D. Freeman, Polymer 2018, 146, 196.

[92] J. Kamcev, R. Sujanani, E.-S. Jang, N. Yan, N. Moe, D. R. Paul, B. D. Freeman, Journal of Membrane Science 2018, 547, 123.

[93] H. Dechiraju, M. Jia, L. Luo, M. Rolandi, Advanced Sustainable Systems 2022, 6, 2100173.

[94] M. Jia, L. Luo, M. Rolandi, Macromolecular Rapid Communications 2022, 43, 2100687.

[95] T. Nguyen, N. Asefifeyzabadi, H. Li, L. Luo, M. Rolandi, Advanced Materials Technologies 2023, 8, 2201996.

[96] A. Y. Mitrophanov, E. A. Groisman, Bioessays 2008, 30, 542.

[97] C. Cosentino, Bates, D. , *Feedback Control in Systems Biology*, CRC Press, Boca Raton 2012.

[98] S. Keene, Y. van de Burgt, Nat Mater 2020.

[99] M. Levin, J. Selberg, M. Rolandi, iScience 2019, 22, 519.

[100] J. Selberg, M. Gomez, M. Rolandi, Cell Syst 2018, 7, 231.

[101] H. Yuk, B. Lu, X. Zhao, Chem Soc Rev 2019, 48, 1642.

[102] M. Jakešová, M. Silverå Ejneby, V. Đerek, T. Schmidt, M. Gryszel, J. Brask, R. Schindl, D. T. Simon, M. Berggren, F. Elinder, E. D. Głowacki, Science Advances 2019, 5, eaav5265.

[103] R. Epsztein, E. Shaulsky, M. Qin, M. Elimelech, Journal of Membrane Science 2019, 580, 316.

[104] A. Jonsson, Z. Y. Song, D. Nilsson, B. A. Meyerson, D. T. Simon, B. Linderoth, M. Berggren, Science Advances 2015, 1.

[105] M. Seitanidou, R. Blomgran, G. Pushpamithran, M. Berggren, D. T. Simon, Adv Healthc Mater 2019, 8.

[106] I. Bernacka-Wojcik, M. Huerta, K. Tybrandt, M. Karady, M. Y. Mulla, D. J. Poxson, E. O. Gabrielsson, K. Ljung, D. T. Simon, M. Berggren, E. Stavrinidou, Small 2019, 15.

[107] Y. Deng, E. Josberger, J. Jin, A. F. Rousdari, B. A. Helms, C. Zhong, M. Anantram, M. Rolandi, Scientific reports 2013, 3.

[108] T. Miyake, E. E. Josberger, S. Keene, Y. Deng, M. Rolandi, APL Materials 2015, 3, 014906.

[109] T. Miyake, M. Rolandi, Journal of Physics: Condensed Matter 2015, 28, 023001.

[110] C. Zhong, Y. Deng, A. F. Roudsari, A. Kapetanovic, M. Anantram, M. Rolandi, Nature Communications 2011, 2, 476.

[111] Z. Hemmatian, S. Keene, E. Josberger, T. Miyake, C. Arboleda, J. Soto-Rodriguez, F. Baneyx, M. Rolandi, Nature Communications 2016, 7.

[112] J. Soto-Rodriguez, Z. Hemmatian, E. E. Josberger, M. Rolandi, F. Baneyx, Advanced Materials 2016, 28, 6581.

[113] D. J. Blackiston, K. A. McLaughlin, M. Levin, Cell Cycle 2009, 8, 3527.

[114] S. H. Wright, Adv Physiol Educ 2004, 28, 139.

[115] C. M. Ajo-Franklin, A. Noy, Advanced Materials 2015.

[116] J. L. Whited, M. Levin, Curr Opin Genet Dev 2019, 57, 61.

[117] H. F. Lodish, *Molecular cell biology*, W.H. Freeman, New York 2000.

[118] S. Sundelacruz, M. Levin, D. L. Kaplan, Stem cell reviews and reports 2009, 5, 231.

[119] L. Abdul Kadir, M. Stacey, R. Barrett-Jolley, Front Physiol 2018, 9, 1661.

[120] M. Levin, G. Pezzulo, J. M. Finkelstein, Annu Rev Biomed Eng 2017, 19, 353.

[121] R. Kwok, Nature 2010, 463, 288.

[122] M. B. Elowitz, A. J. Levine, E. D. Siggia, P. S. Swain, Science 2002, 297, 1183.

[123] S. K. Aoki, G. Lillacci, A. Gupta, A. Baumschlager, D. Schweingruber, M. Khammash, Nature 2019, 570, 533.

[124] L. Bleris, Z. Xie, D. Glass, A. Adadey, E. Sontag, Y. Benenson, Mol Syst Biol 2011, 7, 519.

[125] C. Briat, A. Gupta, M. Khammash, J R Soc Interface 2018, 15.

[126] C. Briat, M. Khammash, ACS Synth Biol 2018, 7, 419.

[127] C. Briat, C. Zechner, M. Khammash, ACS Synth Biol 2016, 5, 1108.

[128] J. Doyle, M. Csete, PLoS Biol 2005, 3, e392.

[129] M. Freeman, Nature 2000, 408, 313.

[130] T. W. Grunberg, D. Del Vecchio, Curr Opin Biotechnol 2019, 63, 41.

[131] M. Lawrynczuk, Chem Eng J 2008, 145, 290.

[132] D. Mishra, P. M. Rivera, A. Lin, D. Del Vecchio, R. Weiss, Nat Biotechnol 2014, 32, 1268.

[133] F. Menolascina, G. Fiore, E. Orabona, L. De Stefano, M. Ferry, J. Hasty, M. di Bernardo, D. di Bernardo, PLoS Comput Biol 2014, 10, e1003625.

[134] A. Milias-Argeitis, M. Rullan, S. K. Aoki, P. Buchmann, M. Khammash, Nat Commun 2016, 7, 12546.

[135] K. H. Ang, G. Chong, Y. Li, IEEE transactions on control systems technology 2005, 13, 559.

[136] G. Fiore, G. Perrino, M. Di Bernardo, D. Di Bernardo, ACS synthetic biology 2016, 5, 154.

[137] J.-B. Lugagne, S. S. Carrillo, M. Kirch, A. Köhler, G. Batt, P. Hersen, Nature communications 2017, 8, 1.

[138] V. G. Maltarollo, K. M. Honório, A. r. B. F. da Silva, Artificial neural networks-architectures and applications 2013, 203.

[139] C. Angermueller, T. Pärnamaa, L. Parts, O. Stegle, Molecular systems biology 2016, 12, 878.

[140] Y. Park, M. Kellis, Nature biotechnology 2015, 33, 825.

[141] D. M. Camacho, K. M. Collins, R. K. Powers, J. C. Costello, J. J. Collins, Cell 2018, 173, 1581.

[142] S. N. Kumpati, P. Kannan, IEEE Transactions on neural networks 1990, 1, 4.

[143] E. Lavretsky, K. A. Wise, in *Advanced textbooks in control and signal processing*,, Springer,, London ; New York 2013, 1 online resource.

[144] M. J. a. G. M. a. J. S. a. M. J. a. H. D. a. P. P. a. M. T. a. M. R. a. M. Gomez, IEEE Control Systems Letters 2020.

[145] J. Park, I. W. Sandberg, Neural Comput 1991, 3, 246.

[146] J. Park, I. W. Sandberg, Neural Comput 1991, 3, 246.

[147] G. Marquez, B. Johnson, M. Jafari, M. Gomez, "Online machine learning based predictor for biological systems", presented at *2019 IEEE Symposium Series on Computational Intelligence (SSCI)*, 2019.

[148] X. Strakosas, J. Selberg, X. Zhang, N. Christie, P. H. Hsu, A. Almutairi, M. Rolandi, Adv Sci (Weinh) 2019, 6, 1970041.

[149] Z. Hemmatian, E. Jalilian, S. Lee, X. Strakosas, A. Khademhosseini, A. Almutairi, S. R. Shin, M. Rolandi, ACS Applied Materials & Interfaces 2018, 10, 21782.

[150] A. Massa, F. Perut, T. Chano, A. Woloszyk, T. A. Mitsiadis, S. Avnet, N. Baldini, Eur Cell Mater 2017, 33, 252.

[151] S. C. Chao, G. J. Wu, S. F. Huang, N. T. Dai, H. K. Huang, M. F. Chou, Y. T. Tsai, S. P. Lee, S. H. Loh, World J Stem Cells 2018, 10, 196.

[152] Y. Xu, P. Zou, A. E. Cohen, Curr Opin Chem Biol 2017, 39, 1.

[153] R. Kateklum, B. Manuel, C. Pieralli, S. Mankhetkorn, B. Wacogne, International Journal of Photochemistry and Photobiology 2017, 2, 94

[154] J. Platisa, G. Vasan, A. Yang, V. A. Pieribone, ACS Chem Neurosci 2017, 8, 513.

[155] L. Jin, Z. Han, J. Platisa, J. R. Wooltorton, L. B. Cohen, V. A. Pieribone, Neuron 2012, 75, 779.

[156] S. Almeida, Z. Zhang, G. Coppola, W. Mao, K. Futai, A. Karydas, M. D. Geschwind, M. C. Tartaglia, F. Gao, D. Gianni, M. Sena-Esteves, D. H. Geschwind, B. L. Miller, R. V. Farese, Jr., F. B. Gao, Cell Rep 2012, 2, 789.

[157] J. Marh, Z. Stoytcheva, J. Urschitz, A. Sugawara, H. Yamashiro, J. B. Owens, I. Stoytchev, P. Pelczar, R. Yanagimachi, S. Moisyadi, Proc Natl Acad Sci U S A 2012, 109, 19184.

[158] J. Wang, X. Wu, C. Chon, T. Gonska, D. Li, Measurement Science and Technology 2012, 23, 025701.

[159] M. Jia, H. Dechiruji, J. Selberg, P. Pansodtee, J. Mathews, C. Wu, M. Levin, M. Teodorescu, M. Rolandi, APL Materials 2020, 8, 091106.

[160] U. K. Udensi, P. B. Tchounwou, Int J Clin Exp Physiol 2017, 4, 111.

[161] C. Svensen, in *Pharmacology and Physiology for Anesthesia (Second Edition)*, (Eds: H. C. Hemmings, T. D. Egan), Elsevier, Philadelphia 2019, 814.

[162] G. G. Somjen, Annual Review of Physiology 1979, 41, 159.

[163] C. Fisch, S. B. Knoebel, H. Feigenbaum, K. Greenspan, Progress in Cardiovascular Diseases 1966, 8, 387.

[164] S. K. Doke, S. C. Dhawale, Saudi Pharmaceutical Journal 2015, 23, 223.

[165] C. Pitsalidis, A.-M. Pappa, A. J. Boys, Y. Fu, C.-M. Moysidou, D. van Niekerk, J. Saez, A. Savva, D. Iandolo, R. M. Owens, Chemical Reviews 2022, 122, 4700.

[166] M. Seitanidou, K. Tybrandt, M. Berggren, D. T. Simon, Lab on a Chip 2019, 19, 1427.

[167] V. A. Pokrovskii, H. C. Helgeson, Geochimica et Cosmochimica Acta 1997, 61, 2175.

[168] V. M. M. Lobo, A. C. F. Ribeiro, L. M. P. Verissimo, Journal of Molecular Liquids 1998, 78, 139.

[169] M. Jafari, G. Marquez, J. Selberg, M. Jia, H. Dechiraju, P. Pansodtee, M. Teodorescu, M. Rolandi, M. Gomez, IEEE Control Systems Letters 2021, 5, 1133.

[170] A. D. Mickle, S. M. Won, K. N. Noh, J. Yoon, K. W. Meacham, Y. Xue, L. A. McIlvried, B. A. Copits, V. K. Samineni, K. E. Crawford, D. H. Kim, P. Srivastava, B. H. Kim, S. Min, Y. Shiuan, Y. Yun, M. A. Payne, J. Zhang, H. Jang, Y. Li, H. H. Lai, Y. Huang, S.-I. Park, R. W. Gereau, J. A. Rogers, Nature 2019, 565, 361.

[171] J. Isaksson, P. Kjäll, D. Nilsson, N. Robinson, M. Berggren, A. Richter-Dahlfors, Nature Materials 2007, 6, 673.

[172] A. Jonsson, Z. Song, D. Nilsson, B. A. Meyerson, D. T. Simon, B. Linderoth, M. Berggren, Science Advances 2015, 1, e1500039.

[173] P. Pansodtee, J. Selberg, M. Jia, M. Jafari, H. Dechiraju, T. Thomsen, M. Gomez, M. Rolandi, M. Teodorescu, PLOS ONE 2021, 16, e0257167.

[174] A. L. Hodgkin, A. F. Huxley, The Journal of physiology 1952, 117, 500.

[175] F. H. Yu, W. A. Catterall, Genome Biology 2003, 4, 207.

[176] R. Bagur, G. Hajnóczky, Mol Cell 2017, 66, 780.

[177] V. Nascimento Da Conceicao, Y. Sun, K. Ramachandran, A. Chauhan, A. Raveendran, M. Venkatesan, B. DeKumar, S. Maity, N. Vishnu, G. A. Kotsakis, P. F. Worley, D. L. Gill, B. B. Mishra, M. Madesh, B. B. Singh, iScience 2021, 24, 103339.

[178] K. Zlobina, M. Jafari, M. Rolandi, M. Gomez, Cell Reports Physical Science 2022, 3, 101149.

[179] R. Owens, P. Kjall, A. Richter-Dahlfors, F. Cicoira, Biochim Biophys Acta 2013, 1830, 4283.

[180] M. F. Griffin, P. E. Butler, A. M. Seifalian, D. M. Kalaskar, World J Stem Cells 2015, 7, 37.

[181] X. Strakosas, M. Seitanidou, K. Tybrandt, M. Berggren, D. T. Simon, Science Advances 2021, 7, eabd8738.

[182] B. Hosseini Jafari, K. Zlobina, G. Marquez, M. Jafari, J. Selberg, M. Jia, M. Rolandi, M. Gomez, J R Soc Interface 2021, 18, 20210497.

[183] C. M. Nguyen, D. M. Tartar, M. D. Bagood, M. So, A. V. Nguyen, A. Gallegos, D. Fregoso, J. Serrano, D. Nguyen, D. Degovics, A. Adams, B. Harouni, J. J. Fuentes, M. G. Gareau, R. W. Crawford, A. M. Soulika, R. R. Isseroff, Diabetes 2019, 68, 1499.

[184] X. Strakosas, J. Selberg, X. Zhang, N. Christie, P. H. Hsu, A. Almutairi, M. Rolandi, Adv Sci (Weinh) 2019, 6, 1800935.

[185] C. M. Proctor, A. Slézia, A. Kaszas, A. Ghestem, I. del Agua, A.-M. Pappa, C. Bernard, A. Williamson, G. G. Malliaras, Science Advances 2018, 4, eaau1291.

[186] I. Uguz, C. M. Proctor, V. F. Curto, A. M. Pappa, M. J. Donahue, M. Ferro, R. M. Owens, D. Khodagholy, S. Inal, G. G. Malliaras, Adv Mater 2017, 29.

[187] Y. Shtessel, C. Edwards, L. Fridman, A. Levant, *Sliding mode control and observation*, Vol. 10, Springer, 2014.

[188] K. D. Young, V. I. Utkin, U. Ozguner, IEEE Transactions on Control Systems Technology 1999, 7, 328.

[189] S. Gambhire, D. R. Kishore, P. Londhe, S. Pawar, International Journal of Dynamics and Control 2021, 9.

[190] V. M. Panchade, R. H. Chile, B. M. Patre, Annual Reviews in Control 2013, 37, 289.

[191] L. Wu, J. Liu, S. Vazquez, S. K. Mazumder, IEEE/CAA Journal of Automatica Sinica 2022, 9, 392.

[192] S. E. McDowell, J. J. Coleman, R. E. Ferner, Bmj 2006, 332, 1177.

[193] P. D. Ganzer, G. Sharma, Neural Regen Res 2019, 14, 46.

[194] M. Giovanny, D. Harika, B. Prabhat, L. Houpu, T. Maryam, P. Pattawong, J. Mohammad, T. Mircea, R. Marco, G. Marcella, bioRxiv 2023, 2023.08.29.555386.

[195] M. Levin, Cell 2021, 184, 1971.

[196] M. Levin, Mol Biol Cell 2014, 25, 3835.

[197] W. Gerstner, W. M. Kistler, *Spiking neuron models: Single neurons, populations, plasticity*, Cambridge university press, 2002.

[198] C. J. Comerci, A. L. Gillman, L. Galera-Laporta, E. Gutierrez, A. Groisman, J. W. Larkin, J. Garcia-Ojalvo, G. M. Süel, Cell Systems 2022, 13, 488.

[199] K. Kikuchi, L. Galera-Laporta, C. Weatherwax, J. Y. Lam, E. C. Moon, E. A. Theodorakis, J. Garcia-Ojalvo, G. M. Süel, Science 2022, 378, 43.

[200] H. Dechiraju, J. Selberg, M. Jia, P. Pansodtee, H. Li, H.-C. Hsieh, C. Hernandez, N. Asefifeyzabadi, T. Nguyen, P. Baniya, G. Marquez, C. Rasmussen-Ivey, C. Bradley, M. Teodorescu, M. Gomez, M. Levin, M. Rolandi, AIP Advances 2022, 12, 125205.

[201] M. Jia, M. Jafari, P. Pansodtee, M. Teodorescu, M. Gomez, M. Rolandi, APL Materials 2022, 10, 041112.

[202] J. W. Costerton, P. S. Stewart, E. P. Greenberg, science 1999, 284, 1318.

[203] J. Liu, A. Prindle, J. Humphries, M. Gabalda-Sagarra, M. Asally, D.-y. D. Lee, S. Ly, J. Garcia-Ojalvo, G. M. Süel, Nature 2015, 523, 550.

[204] C.-Y. Yang, M. Bialecka-Fornal, C. Weatherwax, J. W. Larkin, A. Prindle, J. Liu, J. Garcia-Ojalvo, G. M. Süel, Cell Systems 2020, 10, 417.

[205] P. Baniya, M. Tebyani, N. Asefifeyzabadi, T. Nguyen, C. Hernandez, K. Zhu, H. Li, J. Selberg, H.-C. Hsieh, P. Pansodtee, H.-y. Yang, C. Recendez, G. Keller, W. S. Hee, E. Aslankoohi, R. R. Isseroff, M. Zhao, M. Gomez, M. Rolandi, M. Teodorescu, Scientific Reports 2023, 13, 14766.